

## Superconducting quantum interference in semiconducting Josephson junctions

de Vries, Fokko

**DOI**

[10.4233/uuid:a536ba72-441e-42fb-803f-a762a9c25c07](https://doi.org/10.4233/uuid:a536ba72-441e-42fb-803f-a762a9c25c07)

**Publication date**

2019

**Document Version**

Final published version

**Citation (APA)**

de Vries, F. (2019). *Superconducting quantum interference in semiconducting Josephson junctions*. [Dissertation (TU Delft), Delft University of Technology]. <https://doi.org/10.4233/uuid:a536ba72-441e-42fb-803f-a762a9c25c07>

**Important note**

To cite this publication, please use the final published version (if applicable). Please check the document version above.

**Copyright**

Other than for strictly personal use, it is not permitted to download, forward or distribute the text or part of it, without the consent of the author(s) and/or copyright holder(s), unless the work is under an open content license such as Creative Commons.

**Takedown policy**

Please contact us and provide details if you believe this document breaches copyrights. We will remove access to the work immediately and investigate your claim.

**SUPERCONDUCTING QUANTUM INTERFERENCE  
IN SEMICONDUCTING JOSEPHSON JUNCTIONS**



# **SUPERCONDUCTING QUANTUM INTERFERENCE IN SEMICONDUCTING JOSEPHSON JUNCTIONS**

## **Proefschrift**

ter verkrijging van de graad van doctor  
aan de Technische Universiteit Delft,  
op gezag van de Rector Magnificus prof. dr. ir. T.H.J.J. van der Hagen  
voorzitter van het College voor Promoties,  
in het openbaar te verdedigen op  
woensdag 13 maart 2019 om 12:30 uur

door

**Folkert Kornelis DE VRIES**

Natuurkundig ingenieur, Technische Universiteit Delft, Nederland  
geboren te Amsterdam, Nederland



Dit proefschrift is goedgekeurd door de promotoren.

Samenstelling promotiecommissie:

Rector Magnificus,	voorzitter
Prof. dr. ir. L. P. Kouwenhoven,	Technische Universiteit Delft, promotor
Dr. S. Goswami,	Technische Universiteit Delft, copromotor

*Onafhankelijke leden:*

Prof. dr. J. Klinovaja,	Universität Basel
Prof. dr. ir. B. J. van Wees,	Rijksuniversiteit Groningen
Prof. dr. C. W. J. Beenakker,	Universiteit Leiden
Prof. dr. G. A. Steele,	Technische Universiteit Delft
Prof. dr. ir. R. Hanson,	Technische Universiteit Delft, reservelid



Copyright © 2018 by F. K. de Vries

Cover design by Fokko de Vries

Printed by Gildeprint

Casimir PhD Series, Delft-Leiden 2019-02

ISBN 978-90-8593-384-7

An electronic version of this dissertation is available at

<http://repository.tudelft.nl/>.

# SUMMARY

A topological superconductor is a new state of matter that attracts a lot of interest for its potential application in quantum computers. However, there is no single material known to host this state of matter. In this thesis, combinations of superconductors and semiconductors are investigated experimentally with the goal to engineer such a topological superconductor. The materials chosen combine spin-orbit interaction, superconductivity and one-dimensionality. Then, under influence of a magnetic field, the hybrid superconductor semiconductor system is predicted to become topological.

First, the theoretical background of the experiments is presented, with special attention to the superconducting quantum interference in semiconducting Josephson junctions. In addition, a description of the different materials used and the fabrication of the devices, is provided.

In the first experiment we explore hole transport through GeSi core-shell nanowires. Electronic measurements reveal two transport channels only, which underlines the one-dimensionality of the nanowire. On top of that, high-quality induced superconductivity is observed in both the tunneling and open regime, and evidence for strong spin-orbit interaction is presented.

Then, we switch materials to a two-dimensional electron and hole gas in an InAs/GaSb double quantum well. The spin-orbit interaction is studied by measuring the difference between the densities of electrons with opposite spin orientation. Two types of spin-orbit interaction are identified by tuning the magnitude of one of them, with an applied electric field.

InAs quantum wells are known to exhibit enhanced conduction at their edges. We find supercurrent through these edges in Josephson junction devices using superconducting quantum interference measurements. The interference pattern reveals a flux periodicity of  $h/e$ . Interestingly, while this periodicity is observed in the trivial regime, it was considered a signature of topological superconductivity before. We argue and show that nonlocal processes lead to the  $h/e$  effect in our devices. The correlated occurrence of enhanced edge conduction and the  $h/e$  periodicity is confirmed in Josephson junctions made of InSb flakes.

The final experimental chapter considers a superconducting quantum interference device, fabricated in an InAs quantum well. This geometry allows for control of the superconducting phase difference of the Josephson junction, potentially reducing the magnetic field needed for the device to become topological. Unfortunately, in the measurements we do not observe signatures of topological superconductivity.

At last, we describe what device geometry and material combination could be used to do reach the topological regime. In addition, we discuss ideas for future research of the other material systems used in this thesis.



# SAMENVATTING

Een topologische supergeleider is een nieuwe toestand van materie die veel aandacht trekt dankzij zijn potentiële toepassingen in kwantumcomputers. Er is echter geen afzonderlijk materiaal bekend dat deze toestand van materie herbergt. In dit proefschrift worden combinaties van supergeleiders en halfgeleiders experimenteel onderzocht, met als doel een dergelijke topologische supergeleider te construeren. De gekozen materialen combineren spin-baaninteractie, supergeleiding en eendimensionaliteit. Door het aanleggen van een magneetveld zou het hybride supergeleider halfgeleider systeem dan topologisch kunnen worden.

Eerst wordt de theoretische achtergrond van de experimenten gepresenteerd, met speciale aandacht voor supergeleidende kwantuminterferentie in halfgeleidende Josephson juncties. Daarnaast is er een beschrijving van de gebruikte materialen en de fabricage van de hybride systemen bijgevoegd.

In het eerste experiment onderzoeken we transport van gaten door GeSi kern-schil nanodraden. Elektronische metingen onthullen slechts twee transportkanalen, wat de eendimensionaliteit van de nanodraden onderstreept. Bovendien is er hoge kwaliteit geïnduceerde supergeleiding geobserveerd in zowel het tunneling als open regime, en bewijs voor sterke spin-baaninteractie gepresenteerd.

Vervolgens wisselen we van materiaal naar een tweedimensionaal elektronen en gaten gas in een InAs/GaSb dubbele kwantumput. De spin-baaninteractie is bestudeerd door het meten van het verschil in dichtheid van de elektronen met tegenovergestelde spinoriëntatie. Twee types spin-baaninteractie zijn geïdentificeerd door met een aangelegd elektrisch veld de grootte van een van de twee te veranderen.

Het is bekend dat InAs kwantumputten versterkte geleiding op hun randen laten zien. We observeren superstroom door deze randen in Josephson juncties, gebruik makend van supergeleidende kwantuminterferentie metingen. Het interferentiepatroon laat een flux periodiciteit van  $h/e$  zien. Interessant is dat, terwijl deze periodiciteit geobserveerd is in het triviale regime, zij werd beschouwd als een indicatie van topologische supergeleiding. We beargumenteren en laten zien dat nietlokale processen in onze juncties leiden tot dit  $h/e$  effect. De gecorreleerde observatie van de versterkte randgeleiding en de  $h/e$  periodiciteit is bevestigd in Josephson juncties gemaakt van InSb schilfers.

Het laatste experimentele hoofdstuk beschouwt een supergeleidende kwantuminterferentie device, gefabriceerd in een InAs kwantumput. Deze geometrie maakt het mogelijk het supergeleidende faseverschil van de Josephson junctie te controleren, wat potentieel het magneetveld, dat nodig is om de junctie topologisch te maken, reduceert. Helaas observeren we geen indicaties van topologische supergeleiding in de metingen.

Tenslotte beschrijven we welke geometrie en materiaalcombinatie gebruikt zouden kunnen worden om het topologische regime te bereiken. Daarnaast bediscussiëren we ideeën voor toekomstig onderzoek in andere materiaalsystem die in dit proefschrift gebruikt zijn.



# CONTENTS

<b>Summary</b>	<b>v</b>
<b>Samenvatting</b>	<b>vii</b>
<b>1 Introduction</b>	<b>1</b>
<b>2 Theory</b>	<b>7</b>
2.1 Hamiltonian . . . . .	8
2.1.1 Kinetic energy and confinement . . . . .	8
2.1.2 Magnetic field orbital effect . . . . .	10
2.1.3 Zeeman effect . . . . .	11
2.1.4 Spin-orbit interaction . . . . .	12
2.1.5 Superconductivity . . . . .	14
2.2 Superconducting quantum interference . . . . .	15
2.2.1 Josephson junction . . . . .	15
2.2.2 Superconducting quantum interference: basic picture. . . . .	17
2.2.3 SQI pattern from ABS spectrum . . . . .	18
<b>3 Materials, Fabrication and Measurements</b>	<b>25</b>
3.1 Materials & Fabrication . . . . .	26
3.1.1 Low dimensional nanostructures . . . . .	26
3.1.2 2D heterostructures . . . . .	28
3.2 Measurement setup. . . . .	30
<b>4 Spin-orbit interaction and induced superconductivity in a one-dimensional hole gas</b>	<b>31</b>
4.1 Introduction . . . . .	32
4.2 Experimental setup . . . . .	32
4.3 Superconducting quantum dot . . . . .	32
4.4 Andreev processes . . . . .	34
4.5 Landé g-factor anisotropy and spin-orbit interaction . . . . .	35
4.6 Hard superconducting gap . . . . .	37
4.7 Conclusion . . . . .	39
4.8 Supplementary Material . . . . .	39
4.8.1 Calculation of multiple Andreev reflection and the fitting procedure . . . . .	39
4.8.2 Numerical calculations . . . . .	39
4.8.3 Supplementary figures. . . . .	47

<b>5</b>	<b>Spin-orbit interaction in a dual gated InAs/GaSb quantum well</b>	<b>49</b>
5.1	Introduction . . . . .	50
5.2	Experimental setup . . . . .	50
5.3	Electron regime . . . . .	51
5.4	Landau level simulations . . . . .	53
5.5	Two-carrier regime . . . . .	55
5.6	Conclusion . . . . .	57
5.7	Supplementary Material . . . . .	57
5.7.1	Fourier Transforms. . . . .	57
5.7.2	Details on the Landau level simulation. . . . .	57
5.7.3	Supplementary Figures . . . . .	58
<b>6</b>	<b><i>h/e</i> Superconducting Quantum Interference through Trivial Edge States in InAs</b>	<b>63</b>
6.1	Introduction . . . . .	64
6.1.1	Trivial edge states . . . . .	64
6.2	Experimental setup . . . . .	66
6.3	Superconducting quantum interference . . . . .	67
6.4	Gate dependence . . . . .	69
6.5	Even-odd pattern . . . . .	70
6.6	Phenomenological and tight binding model . . . . .	71
6.7	Conclusion . . . . .	73
6.8	Supplementary Material . . . . .	73
6.8.1	Hall bar measurement . . . . .	73
6.8.2	Flux focusing and vortices . . . . .	73
6.8.3	Tight binding model . . . . .	74
6.8.4	Supplementary figures . . . . .	76
<b>7</b>	<b>Even-odd superconducting quantum interference in InSb Josephson junctions</b>	<b>79</b>
7.1	Introduction . . . . .	80
7.2	Experimental setup . . . . .	80
7.3	Even-odd superconducting quantum interference . . . . .	81
7.4	Gate dependence . . . . .	83
7.5	Temperature dependence. . . . .	87
7.6	Odd-even effect . . . . .	87
7.7	Conclusion . . . . .	87
7.8	Supplementary Material . . . . .	88
7.8.1	SQI theory models . . . . .	88
7.8.2	Device geometries . . . . .	89
7.8.3	Supplementary Figures . . . . .	89
<b>8</b>	<b>Phase biasing InAs Josephson junctions</b>	<b>93</b>
8.1	Introduction . . . . .	94
8.2	Experimental setup . . . . .	95
8.3	Current Phase Relation measurement prerequisites. . . . .	96
8.4	CPR in an in-plane magnetic field. . . . .	97

---

8.5	Switching current revival in an in-plane magnetic field . . . . .	100
8.6	Conclusions. . . . .	101
8.7	Supplementary Material . . . . .	102
8.7.1	CPR measured with a DC SQUID. . . . .	102
8.7.2	Supplementary Figures . . . . .	103
<b>9</b>	<b>Outlook</b>	<b>105</b>
9.1	Ge-Si nanowires. . . . .	106
9.2	InSb flakes . . . . .	106
9.3	Robust Majorana's in planar Josephson junctions. . . . .	107
9.3.1	Topological gap . . . . .	107
9.3.2	Correlation and nonlocal measurement . . . . .	109
9.3.3	Material system . . . . .	110
	<b>Bibliography</b>	<b>113</b>
	<b>Acknowledgements</b>	<b>127</b>
	<b>Curriculum Vitae</b>	<b>129</b>
	<b>List of Publications</b>	<b>131</b>





# 1

## INTRODUCTION

Early in the 20th century the physics community was puzzled by several observations that could not be explained within the classical theory. The most famous example is the photo-electric effect, once light with the right color shines on a certain material, electrons are excited and free to move, which can be measured by a resulting current flow. This observation brought together different ideas from Boltzmann, Planck and Einstein about discretized energy levels and discrete energy packages. In the experiment, one light particle, later named photon, provides the energy package needed to excite one electron to a higher energy level. This energy package is an integer times the energy quantum, the minimum possible amount of energy. For the effect to work, the difference between the energy levels has to be exactly equal to the wavelength (color) of the photon times this energy quantum. The concept of discretizing for example energy in quanta lies at the basis of quantum mechanics.

In addition, instead of treating particles like billiard balls as in classical physics, quantum mechanics describes a particle with a wavefunction. The amplitude of the wavefunction is the probability to find the particle in a certain location at a certain time. From classical wave theory we know that waves can interfere, like waves on water surfaces or the noise cancellation sound waves in modern day headphones. The interference is either constructive or destructive, depending on the phase difference between the two waves (Fig. 1.1). Analogous to classical interference, the quantum mechanical wavefunctions can interfere as well. Since a single particle is described by a wavefunction, an intriguing consequence of this is the possibility of a particle interfering with itself. For example, if a single electron is injected in a ring, the wavefunction will spread over the two arms, and interferes at the opposite side of the ring. In this thesis we exploit quantum interference in a ring geometry, by interfering the wavefunction of a superconductor with itself.

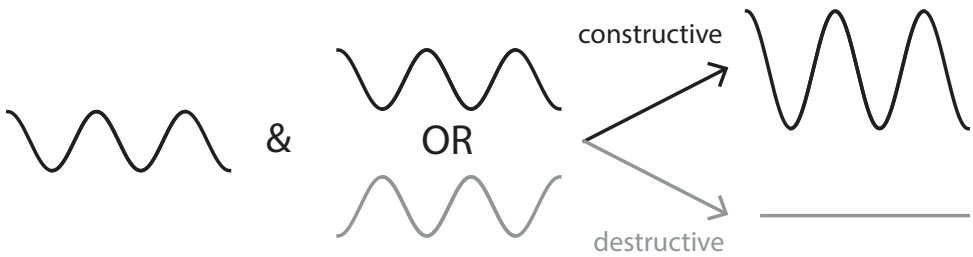


Figure 1.1: **Interference** The phase difference sets the amplitude that comes out. In this example the phase difference is zero for the completely constructive and  $\pi$  for completely destructive. Anything in between is also possible.

Quantum interference effects are studied in the field of solid state physics, in particular in the mesoscopic regime. In this regime, the length of the effect studied is typically smaller than the length over which the phase of the wavefunction is preserved, thus allowing for interference effects. The phase coherence length is typically a few micrometers. On this length scale the physics is usually not well described by a top-down macroscopic model, because for example the charge can not be considered evenly distributed anymore. Also, a bottom up or microscopic description of this size of devices

is computational too costly. Mesoscopic physics forms the bridge between these two and is known for semi-classical and phenomenological explanations. Microscopic models can in some cases be used to simulate (parts or slices of) the device. Simulating the device however, does not directly explain the observed behavior. To obtain a more general understanding of the physical mechanisms playing a role, it is useful to compare the observations with the mesoscopic models.

An interesting new branch in mesoscopic physics concerns the conductance through topologically nontrivial materials. The mathematical framework of topology is then applied to the electronic structure of the materials. The topology is characterized with a topological invariant (a number that is an integer), where trivial means an invariant of zero. If two materials have a different topological invariant, their interface has to be conductive. The bulk properties of the two materials thus dictate what happens at its boundaries, known as the bulk-boundary correspondence. A more simple example of topology and topological invariants is found in the shape of objects. We can divide all objects in the world based on the number of holes in them (the topological invariant). Pinching a hole or breaking a ring shape structure is not allowed, such that the invariant does not change. Then, topologically equivalent objects can be smoothly transformed into each other (Fig. 1.2). Therefore, the topological invariant is stable under smooth transformations. Returning to the topology in the electronic structure, this stability of the topological invariant can stabilize electronic devices, since it can for example reduce the sensitivity to noise.

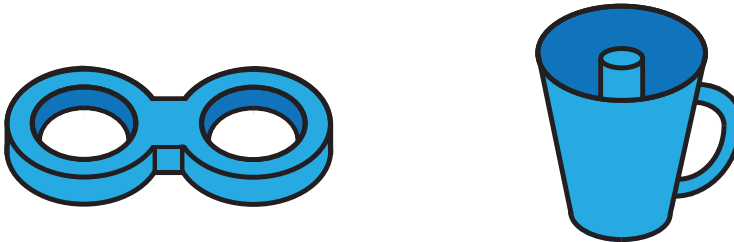


Figure 1.2: **Topology** The double torus can be smoothly deformed into the Pythagoras mug.<sup>1</sup>

One of the promising applications of topologically non trivial materials lies in the field of quantum computing. In a quantum computer, a quantum bit or qubit is formed by a quantum mechanical two level system. Where a classical bit can be either 0 or 1, a qubit can also be a superposition of 0 and 1. In Fig. 1.3 this is illustrated as a bit being either white or black, and the qubit that can also be all gray tones in between. Therefore the information density in a quantum computer scales exponentially ( $2^{(N-1)}$ ) instead of quadratic ( $N^2$ ), as is the case for a classical computer. Together with superposition,

<sup>1</sup>If this is not trivial, you are encouraged to use your favorite search engine and learn about communicating vessels.

quantum mechanical entanglement is at the heart of quantum computing. A single particle of an entangled pair can not be described independently, because the state of that particle is correlated with the other(s). Using these properties, a quantum computer can solve certain problems far more efficient than a classical computer, in example the traveling salesman problem. Two remaining challenges in quantum computing are reducing errors arising from operations, and increasing the timescale over which the information is preserved. A topological qubit, a qubit based on the topology of the electronic structure of a material, could solve both problems.

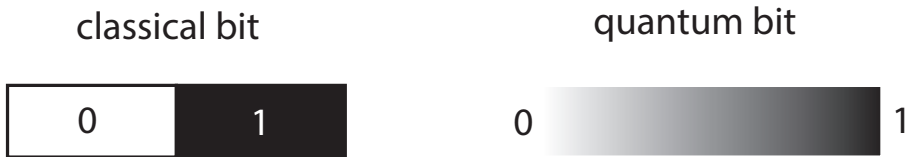


Figure 1.3: **Bit versus qubit.** A classical bit being either 0 or 1 is represented by being either white or black. The quantum bit can take any gray between white and black, so any value between 0 and 1, as well.

Such a topological qubit could be made from particles one finds at the boundary of a topologically nontrivial superconductor. These particles are anyons, and the two qubit levels correspond to the parity of two anyons (even and odd). Once two of the anyons, that live in two dimensions, are exchanged twice, their parity switches, even though the particles returned to the same location. These exchanges, or braids, can thus used to perform quantized qubit operations. The error in the operation that could occur, would be an over-rotation during the exchange of the particles. However, that only impacts the qubit state once the (accumulative) over-rotation equals one full rotation. Due to the bulk-boundary correspondence, the quantum information of the particles is spread over the whole topological superconductor. The information is thus stored non-locally and therefore protected from local noise. In summary, the quantized operations and non-local storage of quantum information could solve the modern day quantum computing challenges.

Unfortunately, there is no material at hand that is a topological superconductor a priori. However, one could engineer it by mixing the following ingredients: a one-dimensional semiconductor with strong spin-orbit interaction, a superconductor, and a large magnetic field. The experimental challenge lies in the combination, and ensuring the relative strengths are in the right ballpark. The search and characterization of possible systems for creating a topological superconductor is the focus of this thesis, which is divided in the following chapters:

- In chapter 2, the basic theoretical background to the various experiments in this thesis is presented, with a focus on superconducting quantum interference.
- The technical aspects of the materials, device fabrication and electronic measurements is treated in chapter 3.
- In chapter 4, the one-dimensional hole gas in Ge-Si semiconducting nanowire is investigated as a candidate material. The spin-orbit interaction, magnetic field response and induced superconductivity are studied.

- Chapter 5 focuses on different spin-orbit interaction mechanisms in InAs/GaSb two-dimensional structures.
- The induced superconductivity in InAs 2DEG is investigated by superconducting quantum interference in Chapter 6. An interference effect, previously related to topological systems, is observed in a trivial system.
- In Chapter 7, Josephson junctions in a different material system, InSb flakes, are investigated via superconducting quantum interference measurements.
- A different geometry, where the superconducting phase difference of the Josephson junction is controlled, is considered in chapter 8.
- At last, an outlook is given on how to proceed to form a topological superconductor in the investigated systems, with a focus on the Josephson junctions from chapter 8.



# 2

## THEORY

*The theoretical background for the upcoming experiments is provided in this chapter. First, the relevant physical phenomena in a semiconducting Josephson junction are described. Then, we focus on superconducting quantum interference (SQI) in the Josephson junctions. The symmetries in the SQI patterns are presented, and we analyze under which circumstances these symmetries are broken.*



## 2.1. HAMILTONIAN

A stationary quantum mechanical system is described by its wavefunction  $\psi(\mathbf{r})$  that lives in a Hilbert space characterized by the eigenvectors and eigenenergies of an Hamiltonian,  $\hat{H}$  [1]:

$$\hat{H}\psi(\mathbf{r}) = E\psi(\mathbf{r}), \quad (2.1)$$

where  $E$  are the eigenenergies.

In a semiconductor, the wavefunction represents charge carriers (electrons or holes) throughout the material. In this section, we discuss the terms in the Hamiltonian that play a role in semiconducting Josephson junctions. On top of that, physical phenomena that lie at the basis of the experiments performed in the following chapters, are discussed.

### 2.1.1. KINETIC ENERGY AND CONFINEMENT

The Hamiltonian describing the kinetic energy of an electron with mass  $m_0$ , and the potential energy landscape it lives in reads [1]:

$$\hat{H}_0 = \frac{\hat{\mathbf{p}}^2}{2m_0} + V(\mathbf{r}) + V_0, \quad (2.2)$$

where  $\hat{\mathbf{p}} = -i\hbar\nabla_{\mathbf{r}}$ , and  $\hbar$  is Planck's constant. In semiconductors, the constant potential  $V_0$  contains the chemical potential  $\mu$ . The spatial dependent part,  $V(\mathbf{r})$ , is caused by a combination of potentials originating from sources inside and outside the semiconducting material.

#### LATTICE POTENTIAL: $\mathbf{k} \cdot \mathbf{p}$ APPROXIMATION

In the semiconductor itself, the electrons live in a periodic potential caused by the crystal lattice,  $V(\mathbf{r} + \mathbf{R}) = V(\mathbf{r})$ , with lattice vector  $\mathbf{R}$ . This crystal periodicity is often used as a basis to describe  $\psi(\mathbf{r})$  in terms of Bloch wavefunctions:

$$\psi(\mathbf{r}) = e^{i\mathbf{k} \cdot \mathbf{r}} u(\mathbf{r}), \quad (2.3)$$

where  $\mathbf{k}$  is the wavenumber and  $u$  are the band depending amplitudes. Using these wavefunctions,  $\hat{H}_0(\mathbf{r})\psi(\mathbf{r})$  can be rewritten to  $\hat{H}_0(\mathbf{k})u(\mathbf{r})$  with:

$$\hat{H}_0(\mathbf{k}) = \frac{1}{2m_0} (\hat{\mathbf{p}}^2 + \hbar^2 \mathbf{k}^2 + 2\hbar \mathbf{k} \cdot \hat{\mathbf{p}}) + V(\mathbf{k}). \quad (2.4)$$

Here, we consider the semiconducting bands close to the band gap (small  $k$ ). For  $k = 0$ , the wavefunctions are obtained by solving the Hamiltonian:

$$\left[ \frac{\hat{\mathbf{p}}^2}{2m_0} + V(\mathbf{k}) \right] u_{n,0}(\mathbf{r}) = E_n(0) u_{n,0}(\mathbf{r}). \quad (2.5)$$

Then, we use the wavefunctions  $u_{n,0}$  found, and treat the  $k^2$  and  $\mathbf{k} \cdot \mathbf{p}$  terms in eq. 2.4 as a perturbation. This approach is called  $\mathbf{k} \cdot \mathbf{p}$  theory, of which a thorough description

can be found in Ref. 2. Here we consider the first and second order perturbations only, resulting in [1]:

$$E_n(k) = E_n(0) + \frac{\hbar^2 k^2}{2m_0} + \frac{\hbar^2}{m_0^2} \sum_{m \neq n} \frac{|\langle u_{m,0} | \mathbf{k} \cdot \mathbf{p} | u_{n,0} \rangle|^2}{E_m(0) - E_n(0)} \quad (2.6)$$

Substituting the perturbation terms with the effective mass,  $m_{\text{eff}}$ :

$$\frac{1}{m_{\text{eff}}} = \frac{1}{m_0} + \frac{1}{m_0^2} \sum_{m \neq n} \frac{|\langle u_{m,0} | \mathbf{k} \cdot \mathbf{p} | u_{n,0} \rangle|^2}{E_m(0) - E_n(0)}, \quad (2.7)$$

leads to the following eigenenergies and Hamiltonian:

$$E_n(k) = E_n(0) + \frac{\hbar^2 k^2}{2m_{\text{eff}}}, \quad (2.8)$$

$$H_0(\mathbf{k}) = \frac{\hbar^2 k^2}{2m_{\text{eff}}} + V(\mathbf{k}). \quad (2.9)$$

The Hamiltonian in the semiconductor crystal thus has eigenstates (or bands) that depend quadratically on  $k$ , which is known as the parabolic band approximation.

### EXTERNAL POTENTIALS

If the wavefunction is confined by either the boundary of the semiconductor or external potentials, its energy eigenvalues are quantized with an energy level difference,  $\epsilon$ . Once the confinement length  $L$  becomes smaller than the typical length of  $\psi(\mathbf{r})$  (the Fermi wavelength  $\lambda_F$ ), the spatial dimensionality of the Hamiltonian is reduced. Confining the wavefunction in one, two or three spatial dimensions thus leads to a two-, one-, or zero-dimensional (2D, 1D, 0D) systems. Several well known examples are studied in this thesis: a two-dimensional quantum well, a nanowire, and a quantum dot.

If the quantum confinement is caused by a finite size of the semiconductor, the electrostatic potential  $V$  is often not constant at its boundary. An offset of the chemical potential could for example show up at an interface with another material, due the work function difference of the materials [3]. In a two-dimensional quantum well, that could lead to a one-dimensional potential well at its edges. We study the transport through these edges in Chapters 6 and 7.

In a 0D structure, or quantum dot, an additional energy level splitting occurs, caused by the Coulomb interaction. The splitting is known as the charging energy,  $E_C$ , that depends on the capacitance  $C$  of the quantum dot, following  $E_C = e^2/C$ , where  $e$  is the single electron charge. Usually,  $E_C > \epsilon$  (we consider zero temperature), leading to a level structure as represented schematically in Fig. 2.1a [4]. The charge transport through the quantum dot depends on whether there is a level available as schematically drawn in Fig. 2.1b. The suppression of transport due to the charging energy level splitting is known as Coulomb blockade. Higher order processes, such as the Kondo effect [5, 6], can break this blockade condition. The Kondo effect exploits the spin degree of freedom of the quantum dot level. When the quantum dot has nonzero spin, a singlet spin state forms with the spin baths of the leads. Exchanging the spin of the bath and the quantum dot then results in charge transfer (Fig. 2.1c). Because of its spin dependence, this effect is tunable with a magnetic field via the Zeeman effect, as will be discussed in section 2.1.3.

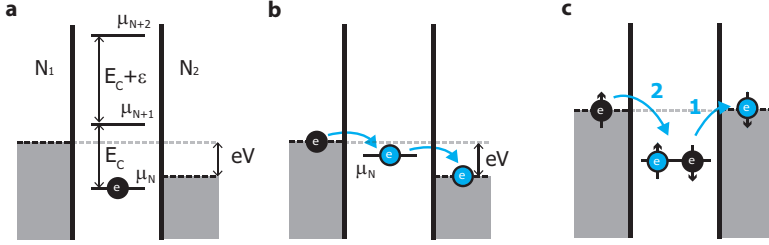


Figure 2.1: **Quantum dot.** **a** Schematic energy diagram of a quantum dot (central region). The chemical potential,  $\mu$ , of the energy levels in the quantum dot are set by the energy level splitting  $\epsilon$  and charging energy  $E_C$ . A bias voltage  $V$  applied over the leads,  $N_{1,2}$ , shifts the Fermi levels of the leads with  $eV$ . In case an energy level is below the energy in both leads, it is filled with an electron, otherwise it is empty. **b** Once an energy level is available in the bias voltage window  $eV$ , the electrons flow as indicated by the arrows. **c** In case of a nonzero spin in the quantum dot and zero bias voltage, the Kondo effect leads to electron transport. In a simplistic picture, a spin flip process as sketched here contributes to the transport. The arrows and numbers identify the direction and order of the tunneling events.

### 2.1.2. MAGNETIC FIELD ORBITAL EFFECT

Once a magnetic field,  $\mathbf{B}$ , is applied, particles with charge  $q$  and velocity  $\mathbf{v}$  are influenced by the this field due to the Lorentz force

$$\mathbf{F} = q(\mathbf{E} + \mathbf{v} \times \mathbf{B}), \quad (2.10)$$

where  $\mathbf{E}$  is the applied electric field. Following the classical Drude model for a 2D system, a free particle with mass  $m_{\text{eff}}$  will follow a circular trajectory at a typical timescale of:

$$\tau_c = \frac{1}{\omega_c} = \frac{m_{\text{eff}}}{e|\mathbf{B}|} \quad (2.11)$$

Depending on whether the circular trajectory is phase coherent or not (whether the phase of  $\psi = |\psi|e^{i\phi}$  is conserved), this effect is described with classical or quantum mechanics. In the quantum mechanical description the orbital effect is taken into account by adding the magnetic vector potential ( $\mathbf{B} = \nabla \times \mathbf{A}$ ) to the momentum by Peierls substitution:

$$\mathbf{p} \rightarrow \mathbf{p} + e\mathbf{A} \quad \text{or} \quad \mathbf{k} \rightarrow \mathbf{k} + \frac{2\pi}{\Phi_0}\mathbf{A} \quad (2.12)$$

where  $\Phi_0 = h/e$  is the flux quantum. Here, we describe the consequences of the orbital effect in the quantum regime, considering the momentum of the charged particles only. The orbital effect in systems where the spin and momentum are coupled is considered in section 2.1.4.

### QUANTUM HALL EFFECT

Treating the Lorentz force quantum mechanically leads to quantization of the electron motion in accordance with the number of flux quanta penetrating its circular orbit [7]. To find the energies of the quantized levels, we consider the following Hamiltonian:

$$H = \frac{(\mathbf{p} + e\mathbf{A})^2}{2m_{\text{eff}}} + V(z), \quad (2.13)$$

where the magnetic field is applied in the  $z$ -direction  $\mathbf{B} = (0, 0, B_z)$ , and the vector potential is  $\mathbf{A} = (-B_z y, 0, 0)$ . The Hamiltonian is separated in parts corresponding to directions in the plane  $(x, y)$  and perpendicular  $(z)$  of a 2D electron gas, where the first becomes [7]:

$$H_{xy} = \frac{(p_x - eB_z y)^2}{2m_{\text{eff}}} + \frac{p_y^2}{2m_{\text{eff}}} \quad (2.14)$$

This Hamiltonian can be solved using the following wavefunction ansatz:  $\psi(x, y) = \phi(y) \exp(ik_x x)$ , which reduces the problem to a harmonic oscillator with eigenenergies:

$$E_n = \hbar\omega_c \left( n + \frac{1}{2} \right) \quad \text{with } n = 0, 1, 2, \dots \quad \text{and } \omega_c = \frac{eB_z}{m_{\text{eff}}}. \quad (2.15)$$

These energy levels are Landau levels and the density of states of the Hall bar is:

$$\text{DOS}(E, B) = \frac{eB}{h} \sum_n \delta(E - E_n), \quad (2.16)$$

where  $\delta$  is the Dirac delta function. The Landau levels have a degeneracy of  $n_{\text{LL}} = eB/h$ , and, as a consequence, the occupation of the Landau levels changes as a function of magnetic field. This shows up in the magnetoresistance in both the longitudinal and transversal direction, and is known as the quantum Hall effect [8]. The Landau levels can be broadened due to finite temperature, and quantum scattering (scattering that dephases  $\psi$ ). In the regime where the broadening is larger than the Landau level separation, the oscillations of the longitudinal resistivity (Shubnikov-deHaas oscillations) are described by the following relation [7]:

$$\rho_{xx} = \frac{m_{\text{eff}}}{ne^2\tau} \left[ 1 - 2e^{-\pi/\omega_c\tau_q} \frac{2\pi^2 k_B T / \hbar\omega_c}{\sinh(2\pi^2 k_B T / \hbar\omega_c)} \cos\left(2\pi \frac{hn}{2eB}\right) \right], \quad (2.17)$$

where  $\tau_q$  is the quantum lifetime,  $T$  the temperature and  $k_B$  Boltzmann's constant. A temperature dependent measurement of the amplitude allows one to extract  $\tau_q$ , and  $m_{\text{eff}}$  (via  $\omega_c$ ). Furthermore, the oscillation frequency is a direct measure for  $n$ , which is used in Chapter 5.

### 2.1.3. ZEEMAN EFFECT

Next to the charge degree of freedom discussed so far, electrons also exhibit a spin degree of freedom. The Zeeman effect describes the response of the spin to an applied magnetic field  $B$ :

$$\hat{H}_Z = \frac{1}{2} \mathbf{g} \mu_B \mathbf{B} \cdot \boldsymbol{\sigma}, \quad (2.18)$$

where  $\mathbf{g}$  is the Landé  $g$ -factor,  $\mu_B$  the Bohr magneton, and  $\boldsymbol{\sigma}$  the Pauli spin matrices  $(\sigma_x, \sigma_y, \sigma_z)$ . The spin of the electrons line up parallel or anti-parallel to the applied magnetic field, leading to a splitting of the bands with the Zeeman energy:

$$E_Z = \pm \frac{1}{2} \mathbf{g} \mu_B |\mathbf{B}|. \quad (2.19)$$

For example, the Kondo resonance in a quantum dot splits, allowing one to extract the  $g$ -factor (see Chapter 4). The value of the  $g$ -factor is material dependent. Additionally, it could be anisotropic, for example due to coupling between the electron spin and its momentum, which we discuss in the following section.

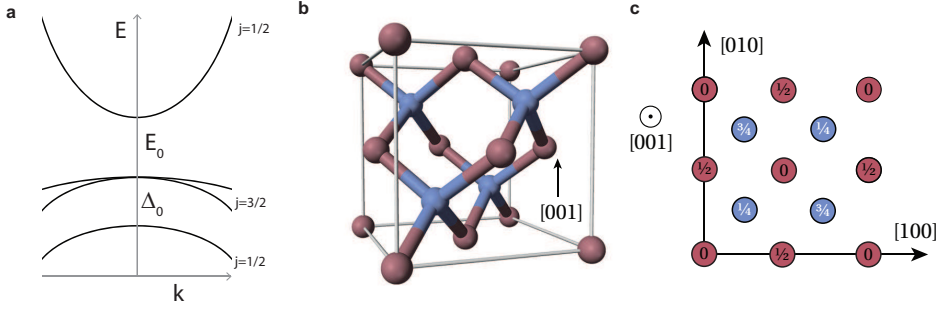


Figure 2.2: **Fermi surfaces with spin-orbit interaction.** **a** Schematic representation of the band structure in the Kane model [10]. Three valence bands and one conduction band are sketched, and their total angular momentum  $j$  is indicated. Furthermore, both the band gap  $E_0$  as well as the spin-orbit gap  $\Delta_0$  are highlighted. **b-c** The zincblende crystal structure, which is inversion asymmetric. Two different atomic species are represented by the blue and red dots. In figure **c** the structure is depicted in the [001] crystal direction, where the numbers highlight the height of the atoms in terms of the lattice constant. These images are taken from Ref. 11.

#### 2.1.4. SPIN-ORBIT INTERACTION

The spin and momentum of an electron can couple because the spin of an electron moving in an electric field interacts with the effective magnetic field experienced by it. This is described by the Pauli spin-orbit term in the non-relativistic approximation of the relativistic Dirac equation [9]:

$$\hat{H}_{\text{SO}} = -\frac{\hbar}{4m_0^2 c^2} \boldsymbol{\sigma} \cdot (\mathbf{p} \times \nabla V), \quad (2.20)$$

where  $c$  is the speed of light.

In solid state crystals, electrons experience the periodic potential of the crystal as they move through it. The SOI arising from this, can be derived by adding  $H_{\text{SO}}$  to eq. 2.2 and solving that with Bloch wavefunctions. A  $\mathbf{k} \cdot \mathbf{p}$  approach, taking into account the bands around the band gap, is sufficient to describe the SOI [10]. The conduction band has an s-type symmetric wavefunction, and therefore no angular momentum. The valence band, instead, has p-type symmetry, thus an angular momentum of  $l = 1$ , and a threefold degeneracy  $\{X, Y, Z\}$ . In addition, all bands have two possible spin states ( $s = -1/2, +1/2$ ). Because the spin is coupled to the angular momentum, the total angular momentum ( $j = l + s$ ) is conserved and identify the bands as sketched in Fig. 2.2a. The SOI term directly couples the three valence bands, splitting the bands in energy with  $\Delta_0$  according to their total angular momentum. The conduction band couples through the valence band with the same  $j$  of  $1/2$ . This coupling is linear in momentum because of the different symmetries of their wavefunctions, and its amplitude depends on the band gap  $E_0$  and  $\Delta_0$  (Fig. 2.2a). As long as the momentum for both spin bands is symmetric around zero, this coupling is symmetric and will only lead to a renormalized  $m_{\text{eff}}$  and  $g$  [7].

However, not all systems exhibit this inversion symmetry, [ $E_s(k) = E_s(-k)$ ]. For example, a zincblende crystal displays bulk inversion asymmetry (BIA), as is visible in the

unit cell sketched in Fig. 2.2b-c. Also, the potential caused by the environment can lack inversion symmetry, which is known as structural inversion asymmetry (SIA). In the following section we present the outcomes of the  $\mathbf{k} \cdot \mathbf{p}$  approximation of inversion asymmetric crystals and potentials [9].

### DRESSELHAUS AND RASHBA

We consider a 2D quantum well, where the electrons confined in two dimensions ( $x, y$ ). The BIA leads to a splitting of the spin degeneracy in momentum space according to Dresselhaus [12]:

$$\hat{H}_{SO,D} = \beta(k_x\sigma_x - k_y\sigma_y) + \gamma(k_xk_y^2\sigma_x - k_yk_x^2\sigma_y), \quad (2.21)$$

where  $\gamma$  is the Dresselhaus SOI parameter and  $\beta$  is the linear coefficient given by  $\gamma \langle k_z \rangle^2$ . In addition, Bychkov and Rashba described the SOI resulting from SIA [13]:

$$\hat{H}_{SO,R} = \alpha(k_y\sigma_x - k_x\sigma_y), \quad (2.22)$$

where  $\alpha$  is the Rashba parameter. The Rashba parameter is strongly dependent on the electrostatic environment, and therefore is usually split into a parts stemming from external electric fields,  $\alpha_0$ , and potential gradients due to material interfaces,  $\alpha_I$  [14]:

$$\alpha = \alpha_0 \mathbf{E} + \alpha_I. \quad (2.23)$$

In Chapter 5 we use the applied electric field to tune  $\alpha$ , while  $\gamma$  stays constant. The Rashba and Dresselhaus SOI describe an energy splitting of the bands dependent on their spin quantum number. There are two energy scales related to this shift in  $k$ . Firstly, the energy difference between the minimum of the band and the energy at  $k=0$ , is called  $E_{SO}$ . Secondly, the energy shift at the Fermi level is  $\Delta_{SO}$ , which is in example for Rashba SOI only equal to  $2\alpha k_F$ . The shift and spin texture at the Fermi level is sketched in Fig. 2.3a-b for both SOI terms separately. Also, a combination of both contributions (in case the two are not equal) is sketched in Fig. 2.3c. Experimentally, the shift due to the SOI can be obtained by measuring the density of the two Fermi surfaces, using Shubnikov-deHaas oscillations (section 2.1.2). This measurement technique is explained in detail in Ref. 14 and used in Chapter 5 of this thesis.

### DIRECT RASHBA

For a hole system with confinement in two directions another type of SOI shows up. The wavefunctions are characterized by their total angular momentum  $j$  due to the confinement potential [16]. These states couple via their dipole moment (if  $l \neq 0$ ) under influence of an applied electric field  $\mathbf{E}$ . This coupling leads to a Rashba like term in the Hamiltonian, and is therefore called direct Rashba SOI [16, 17]:

$$\hat{H}_{SO,DR} = -e\mathbf{E} \cdot \mathbf{r} = eE_x U \tau_x \sigma_z, \quad (2.24)$$

where  $\tau$  and  $\sigma$  are Pauli matrices, and we used  $\mathbf{E} = (E_x, 0, 0)$ , and  $z$  as the direction without confinement. This type of SOI is investigated in nanowires in Chapter 4.

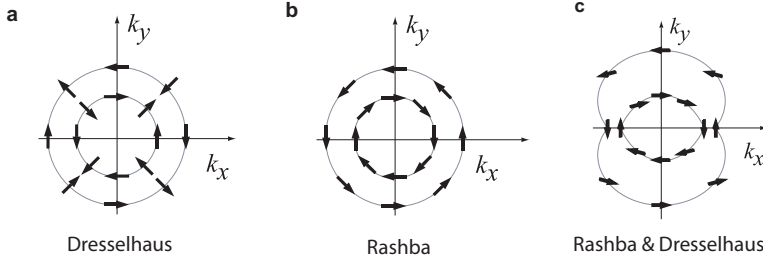


Figure 2.3: **Fermi surfaces with spin-orbit interaction.** The spin polarization at the different  $k$  directions is indicated with the arrows. The spin-orbit interaction terms included are noted for all three panels **a,b,c**. In **c** the Rashba and Dresselhaus strength are unequal. This figure is adapted from Ref. 15.

### MAGNETIC ORBITAL EFFECT & STRAIN

Since the SOI couples the momentum and spin degrees of freedom, the magnetic orbital effect can also influence the spin states of the system. The effect of the momentum shift due to the vector potential is theoretically studied in nanowires, where it strongly impacts the effective Landé  $g$ -factors [18]. The magnitude of the effect is dependent on the relative alignment of the electric and magnetic field. Apart from the SOI, strain in the crystal lattice could induce a shift in the total angular momentum, as described by Bir and Pikus [19]. The shift in total angular momentum reflects in the magnitude of the  $g$ -factor, of which the direction is dependent on the anisotropy of the induced strain.

#### 2.1.5. SUPERCONDUCTIVITY

In a superconductor, electrons form Cooper pairs, bosons that form a condensate. The condensate is generally described by a complex order parameter,  $\Delta = |\Delta|e^{i\phi}$ . The single particle excitation spectrum has an energy gap corresponding to the pairing potential  $|\Delta|$ , and can be described by the Bogoliubov de Gennes (BdG) equation using the mean field approximation [20]:

$$H_s = \begin{bmatrix} H_0 & \Delta \\ \Delta^* & -H_0^* \end{bmatrix}, \quad (2.25)$$

for an s-wave superconductor, where  $H_0$  is given by eq. 2.2. The excitations are quasi-particles with the wavefunction  $\psi(\mathbf{r}) = \begin{bmatrix} \psi_e(\mathbf{r}) \\ \psi_h(\mathbf{r}) \end{bmatrix}$  [20], where  $\psi_e$  and  $\psi_h$  correspond to the electron and hole part of the excitation. Using the BdG equation results in a particle-hole symmetric excitation spectrum. When a superconductor and semiconductor are brought in contact with each other, superconductivity is induced in the semiconductor, following the proximity effect [21]. The BdG equation then introduces the electron-hole symmetry in the Hamiltonian for the semiconductor. This is usually described by using Pauli matrices denoted by  $\tau$ , as for example will be used in the model in chapter 6.

## 2.2. SUPERCONDUCTING QUANTUM INTERFERENCE

In this section we first revisit the basics of a semiconducting Josephson junction, and introduce superconducting quantum interference (SQI). Then, the impact of the geometry, Zeeman effect and SOI terms on the SQI pattern are treated.

### 2.2.1. JOSEPHSON JUNCTION

In 1962 Brian Josephson postulated an equation that describes the current between two superconductors separated by an insulator, the DC Josephson relation [22]:

$$I(\phi(t)) = I_c \sin(\phi(t)), \quad (2.26)$$

where  $\phi$  is the superconducting phase difference, the phase difference between the condensates of the two superconductors. The DC Josephson relation holds in the regime where the Cooper pair transfer between the superconductors is due to tunneling. The maximum supercurrent in the Josephson junction (JJ), also known as the critical current, is independent on the direction of the current in this case and given by:

$$I_c = \max_{\phi=0-2\pi} I(\phi). \quad (2.27)$$

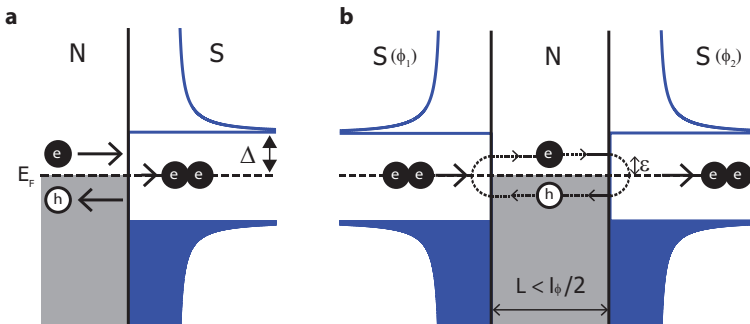


Figure 2.4: **Andreev reflection** **a** Schematic representation of Andreev reflection at a normal metal,  $N$ , superconductor,  $S$ , interface. The incoming electron is retroreflected as a hole, while a Cooper pair is transferred to  $S$ . The Fermi energy,  $E_F$ , and superconducting gap,  $\Delta$ , are indicated. **b** Andreev reflection in a SNS geometry leads to an Andreev bound state with energy,  $\epsilon$ , when the length,  $L$ , of  $N$  does not exceed half the coherence length of the quasiparticles,  $l_\phi$ .

### ANDREEV BOUND STATES

When, instead of an insulator, a semiconductor is contacted by two superconductors, transport could also occur due to Andreev reflection of charge carriers in the semiconductor [23]. Andreev reflection is described as follows: an electron quasiparticle in a semiconductor that reaches a superconductor is retroreflected as a hole quasiparticle, and at the same time a Cooper pair is transferred into the superconductor (Fig. 2.4a). When a quasiparticle Andreev reflects at both sides of the junction, effectively a Cooper pair is transferred through the JJ. If, in addition, the quasiparticle stays phase coherent



during this process, an Andreev bound state (ABS) forms between the two superconductors, as sketched in Fig. 2.4b. To satisfy the phase coherence for a quasiparticle with energy offset from the Fermi level,  $\epsilon$ , the following resonant condition should be met [24]:

$$\phi_e = \phi_1 + \arccos(\epsilon/\Delta) + \phi_h - \phi_2 + \arccos(\epsilon/\Delta) + 2\pi n, \quad (2.28)$$

where  $n = 0, 1, 2, \dots$ , the  $\arccos(\epsilon/\Delta)$  is the phase shift acquired by the evanescent wave (the tunneling term), and  $\phi_1$  and  $\phi_2$  are the phases of the superconducting condensates. Note that this expression holds for the clockwise ABS in sketched in Fig. 2.4b. Including its anti-clockwise counterpart and substituting  $\phi_e - \phi_h = 2L\epsilon v_F/\hbar$  and  $\phi = \phi_1 - \phi_2$ , we find:

$$\frac{\epsilon L}{\xi_s \Delta} = \pm \phi/2 + \arccos(\epsilon/\Delta) + \pi m, \quad (2.29)$$

where  $m = 0, \pm 1, \pm 2, \dots$ ,  $\xi_s = \hbar v_F/\Delta$  is the superconducting coherence length, and  $v_F$  is the Fermi velocity. The ABS level structure in the JJ is characterized by  $\xi_s$  and its length  $L$ : when  $L \gg \xi_s$ , the junction is in the long limit, and oppositely  $L \ll \xi_s$  in the short junction limit. In a long junction, the Thouless energy ( $\hbar v_F l_{\text{mfp}}/L^2$ ) determines the energy levels [25], where for the short junction this is  $\Delta$  [26]. In the remainder of this section we use the short junction limit. For  $L \ll \xi_s$ , the term on the left hand side of eq. 2.29 becomes very small, and the ABS energy levels are given by:

$$\epsilon(\phi) = \pm \Delta \cos(\phi/2). \quad (2.30)$$

Note that the calculated ABS energies in eq. 2.30 is obtained with unity transparency at the super- and semiconductor interface. Using a scattering matrix formalism, the ABS energies are derived for any transparency  $\tau$  [26]:

$$\epsilon_p(\phi) = \Delta \sqrt{1 - \tau_p \sin^2(\phi/2)}. \quad (2.31)$$

### CURRENT PHASE RELATION

The function describing the dependence of the current through the JJ on the superconducting phase difference is called the current phase relation (CPR). Generally, the CPR is derived from the Free energy,  $F$ :

$$I(\phi) = \frac{2e}{\hbar} \frac{\partial F}{\partial \phi}. \quad (2.32)$$

Following this approach, Beenakker found an expression for  $F$  in the JJ in terms of the ABS energies only [26]. Considering  $|\Delta|$  to be constant, the CPR reads [26]:

$$I(\phi) = \frac{e\Delta^2 \sin(\phi)}{2\hbar} \sum_p \frac{\tau_p}{\epsilon_p(\phi)} \tanh\left(\frac{\epsilon_p(\phi)}{2k_B T}\right), \quad (2.33)$$

where  $T$  is the temperature and which is plotted in Fig. 2.5 for different  $\tau$  and  $T$ . As  $\tau$  is increased or  $T$  is decreased, the CPR changes from sinusoidal (like in eq. 2.26) to skewed.

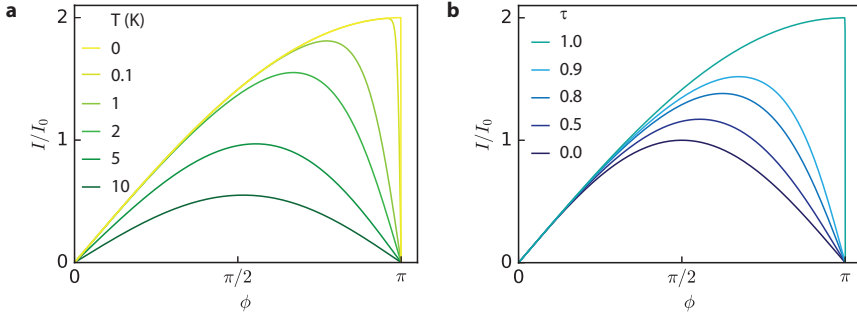


Figure 2.5: **Current phase relation of superconducting quantum point contact.** **a** The normalized critical current, extracted from eq. 2.33 is plotted as function of superconducting phase difference,  $\phi$ , for  $\tau \approx 0$ , and varying  $T$  as indicated. **b** Same as **a**, with  $T \approx 0$ , and varying  $\tau$  as indicated. For both  $\Delta = 1$  meV is used.

### 2.2.2. SUPERCONDUCTING QUANTUM INTERFERENCE: BASIC PICTURE

In a JJ with a magnetic field applied perpendicular to the direction of supercurrent, the magnetic vector potential couples to the superconducting phase difference in the junction, and can cause an interference effect. We describe a basic example of this superconducting quantum interference (SQI), using a JJ with length  $L$  and width  $W$  (see schematic in Fig.2.6a), and a certain CPR,  $I(\phi)$ . Using the gauge  $\mathbf{A} = (0, Bx, 0)$ , we find the gauge invariant phase,  $\gamma$ , for an arbitrary contour,  $C$ , connecting the two superconductors:

$$\gamma(x) = \phi + \frac{2\pi}{\Phi_0} \int_C \mathbf{A} d\mathbf{l} = \phi + \frac{2\pi}{\Phi_0} \int_{-L/2}^{+L/2} A_y dy = \phi + \frac{2\pi}{\Phi_0} BxL, \quad (2.34)$$

where  $\Phi_0 = h/2e$  is the superconducting flux quantum. Restricting ourselves to straight trajectories that are perpendicular to the superconducting contacts, the current through the junction is given by:

$$I(\gamma) = \iint j(x, y) I(\gamma) dx dy = \int_{-W/2}^{W/2} J(x) I(\phi + \frac{2\pi}{\Phi_0} BxL) dx. \quad (2.35)$$

The current density is then dependent on  $x$  only, so we use the current density distribution per unit length in  $y$ ,  $J(x)$ . Next, the CPR is chosen to be sinusoidal,  $I(\phi) = I_c \sin(\phi)$ , and we obtain:

$$I(\phi, B) = \int_{-W/2}^{W/2} J(x) \cos\left(\frac{2\pi}{\Phi_0} BxL\right) \sin(\phi) dx + \int_{-W/2}^{W/2} J(x) \sin\left(\frac{2\pi}{\Phi_0} BxL\right) \cos(\phi) dx \quad (2.36)$$

Finally, we solve the integral, and compute the critical current  $I_c$  as a function of the flux through the junction  $\Phi = BWL$  for two specific expressions for  $J(x)$ . Firstly, we use a constant  $J(x) = I_c/W$  that results in a Fraunhofer shaped SQI pattern:

$$I_c(\Phi)/I_c(0) = \left| \frac{\sin(\pi\Phi/\Phi_0)}{\pi\Phi/\Phi_0} \right|. \quad (2.37)$$

Secondly, for edge transport only,  $J(x) = I_c[\delta(-W/2) + \delta(+W/2)]$ , and we obtain the double slit analogue, or superconducting quantum interference device (SQUID) pattern:

$$I_c(\Phi)/I_c(0) = |\cos(\pi\Phi/\Phi_0)|. \quad (2.38)$$

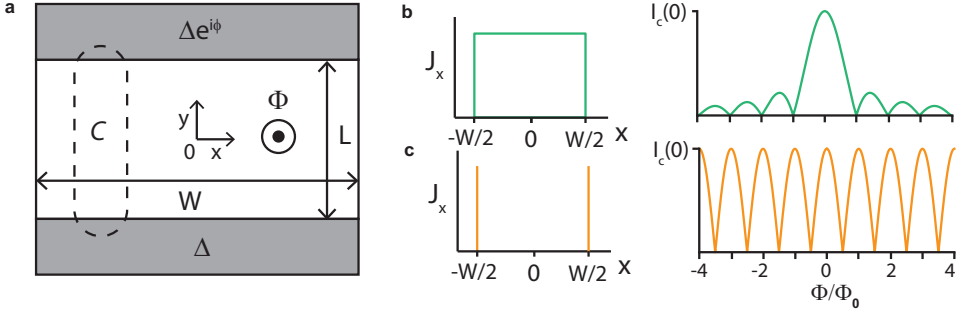


Figure 2.6: **Basics of superconducting quantum interference.** **a** Schematic of a Josephson junction with length  $L$  and width  $W$ . The two superconducting contacts have a gap  $\Delta$  and phase difference  $\phi$ . The magnetic flux,  $\Phi$ , through the junction area is considered, and an example of a contour  $C$  connecting both superconductors is drawn. **b** A homogeneous current distribution,  $J_x$ , accompanied by the Fraunhofer SQUI pattern, observed in the critical current,  $I_c$ , versus normalized flux,  $\Phi/\Phi_0$ . **c** The current is flowing solely through the edges of the devices, resulting in the SQUID interference pattern.

Both current distributions and resulting SQUI patterns are sketched in Fig. 2.6b-c.

Reversing this analysis, enables us to extract the current density distribution from a SQUI pattern, as shows by Dynes and Fulton [27]. For this approach to be valid, one should be in the short junction limit for the trajectories to be straight, and the CPR should be sinusoidal [28]. In the remainder of this section we discuss more complex scenarios, where we consider different geometries, non-homogeneous current density distributions, and non-sinusoidal CPRs.

### GEOMETRY DEPENDENCE

The ratio of the length and width of a JJ can influence the SQUI pattern. In a JJ with a comparable  $L$  and  $W$ , a doubling of the periodicity in the SQUI pattern was observed [29]. Several theoretical works described this via nonlocality of the Andreev quasiparticles, considering their possible trajectories [30, 31]. Depending on the  $L/W$ -ratio, the quasiparticle trajectories span only a part of the total area of the junction, leading to a reduced flux periodicity. In Fig.2.7, the SQUI patterns for several  $L/W$ -ratios are presented, where we used the model described in Ref. 31 for a ballistic JJ. As the ratio increases, the periodicity grows to a maximum of  $2\Phi_0$ .

Furthermore, the geometry of the device can indirectly be influenced by its density of states. For example, if there exists a large density at the edges of a device, the current density distribution is represented by an homogeneous background, with enhanced current at the edges. In Fig.2.7b we plot the resulting SQUI patterns for different values of the background current, and observe a gradual change from a Fraunhofer to SQUID pattern (Fig. 2.6a and b, respectively). This transition is experimentally studied in Chapters 6 and 7 of this thesis.

### 2.2.3. SQUI PATTERN FROM ABS SPECTRUM

Here we describe the effects of a non-sinusoidal CPR on the SQUI pattern observed. The CPR is obtained from the Hamiltonian of the semiconducting JJ. First we connect sym-

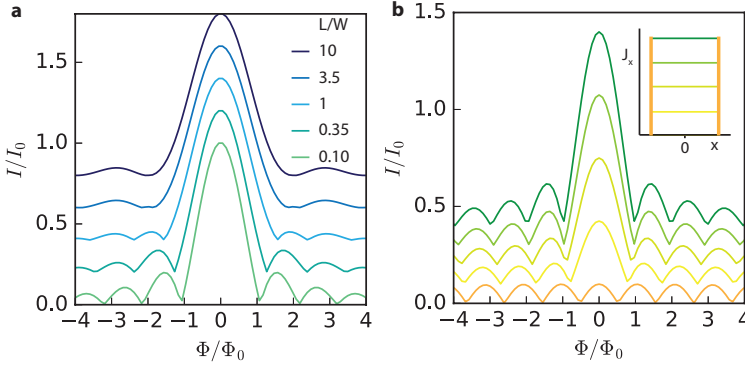


Figure 2.7: **Geometry effect on SQI pattern.** **a** Normalized critical current,  $I/I_0$ , as a function of normalized flux,  $\Phi/\Phi_0$ , for several  $L/W$ -ratios indicated. The model of Ref. 31 is used to calculate these SQI patterns, that are offset by 0.2 for clarity. **b**  $I/I_0$  versus  $\Phi/\Phi_0$  for different current density distributions,  $J_x$ , as sketched in the inset. The SQI pattern changes from a Fraunhofer to SQUID shape, as the current density in the bulk of the sample decreases. A sinusoidal current phase relation is used.

metries in the Hamiltonian to symmetries the CPR, and describe how they show up in the SQI pattern. Then we present the results of modeling the Hamiltonian, to obtain the ABS energies, through which the CPR and SQI pattern are calculated.

### SYMMETRY ANALYSIS

The symmetries of the Hamiltonian translate directly into the Free energy, which is evident from the partition function description:

$$F = -k_B T \ln \text{Tr} e^{-H/T}. \quad (2.39)$$

In addition, the symmetries of  $F$  dictate the symmetries of the CPR through eq. 2.32, linking the Hamiltonian and the CPR. We revisit a thorough symmetry analysis of a 2D Josephson junction with (Rashba and linear Dresselhaus) spin-orbit interaction, Zeeman effect and potential asymmetries, performed in Ref. 32. The Hamiltonian of the semiconductor reads,  $H = H_0 + H_{\text{SO}} + H_Z$ , where the orbital effect is taken into account as well. Superconductivity is included via an s-wave pairing Hamiltonian,  $H_s$ , that is only present in the contacts to the semiconductor (see Ref. 32 for details). In table 2.1, the unitary symmetry operators are presented,  $H = UH'U^\dagger$ , that sustain the symmetry in the CPR indicated. The symmetry operations are given by parity operators  $\mathcal{P}_{x,y}$  that mirror the Hamiltonian in  $x, y = 0$ , respectively, the time reversal operator  $\mathcal{T}$ , and Pauli spin matrices  $\sigma$ . The symmetry breaking terms are either a potential asymmetry,  $V_{x,y}$ , in-plane magnetic field,  $B_{x,y}$ , or linear Rashba or Dresselhaus SOI,  $\alpha, \beta$ , respectively. The coordinate system identical to the one used in Fig.2.6a.

Inspecting the symmetry breaking terms, we see that combinations of  $B_{x,y}$ , and  $\alpha$  and  $\beta$  can break  $I$  and  $III$ , which we come back at in the following paragraphs. Here we

I		II		III	
$I(B_z, \phi) = -I(B_z, -\phi)$		$I(B_z, \phi) = I(-B_z, \phi)$		$I(B_z, \phi) = -I(-B_z, -\phi)$	
$\mathcal{P}_x \mathcal{P}_y$	$V_{x,y}, \alpha, \beta$	$\sigma_y \mathcal{P}_x$	$V_x, B_x, \alpha$	$\mathcal{T}$	$B_{x,y}$
$\sigma_z \mathcal{P}_x \mathcal{P}_y$	$V_{x,y}, B_{x,y}$	$\sigma_x \mathcal{P}_x$	$V_x, B_y, \beta$	$\sigma_z \mathcal{T}$	$\alpha, \beta$
$\sigma_y \mathcal{P}_x \mathcal{T}$	$V_x, B_y, \alpha$	$\mathcal{P}_y \mathcal{P}_x \mathcal{T}$	$V_{x,y}, B_{x,y}, \alpha, \beta$	$\sigma_y \mathcal{P}_y$	$V_y, B_x, \beta$
$\sigma_x \mathcal{P}_x \mathcal{T}$	$V_x, B_x, \beta$	$\sigma_z \mathcal{P}_y \mathcal{P}_x \mathcal{T}$	$V_{x,y}$	$\sigma_x \mathcal{P}_y$	$V_y, B_y, \alpha$

Table 2.1: **Symmetries of the supercurrent.** Three symmetries of the supercurrent as a function of magnetic field,  $B_z$ , and phase difference,  $\phi$ , are presented. The first column represents the symmetry operations of the Hamiltonian, and the second column the terms in the Hamiltonian that protect that symmetry. To lift symmetries *I*, *II* or *III*, all corresponding Hamiltonian symmetry operations should be broken.

focus on the potential asymmetry  $V_x$  that lifts both symmetries *I* and *II*. The asymmetric potential leads to ABS energies dependent on  $x$ . We use two ways to simulate this: by implementing a linear dependence of the transparency on  $x$  in eq. 2.33; and by simply including an asymmetric current distribution, where we take the CPR identical throughout the junction. The SQI pattern is calculated by numerically solving the integral in section 2.2.2. Note that SQI pattern contains the critical current,  $I_c$  (for every magnetic field value). Depending on the sign of the current,  $I_c$  can have different values, so we use  $I_{c,+} = \max_{\phi} I(\phi)$  and  $I_{c,-} = \min_{\phi} I(\phi)$ . Breaking the symmetry  $I(\phi) = I(-\phi)$ , thus only shows up in the interference pattern if  $I_{c,+} = I_{c,-}$  is broken. For clarity, we sketched the effect of the symmetries *I-III* on the SQI pattern in Fig. 2.8. Figures 2.8b,c show the calculated interference patterns while breaking  $V_x$ . Both display that only symmetry III is maintained, as expected from the symmetry analysis. Experimental works confirm that asymmetries of the potential  $V$ , can have a large influence on the shape of the interference patterns [33, 34].

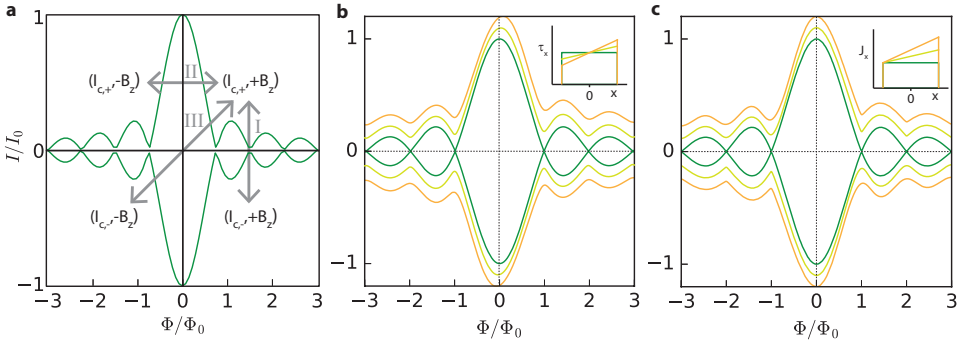


Figure 2.8: **Symmetries in the SQI pattern broken by  $V_x$ .** **a** A Fraunhofer SQI pattern (Eq. 2.37) with influence of the symmetries from table 2.1 sketched. **b** Fraunhofer SQI patterns with asymmetric transparencies,  $\tau(x)$ , of the Andreev levels throughout the JJ (see inset). The green, yellow and orange lines denote the case where  $\tau = 0.75, 0.65$  and  $0.85$  and  $0.55$  to  $0.95$ , respectively. **c** Fraunhofer SQI patterns with an asymmetric current distribution,  $J(x)$ , in the JJ as indicated in the inset. Unity transparency,  $\tau = 1$ , is taken. The traces in **b,c** are offset by 0.1 for clarity and the CPR is calculated from eq. 2.33, using  $T = 50$  mK and  $\Delta = 1$  meV.

### ANDREEV BOUND STATE SPECTRUM

The effect of spin-orbit interaction and in-plane magnetic fields on the symmetries in the SQI pattern can be studied by obtaining the CPR of the JJ through its ABS energy spectrum. We review and use an analytical model proposed by Bezuglyi *et al.*, to obtain the CPR [35]. Then, we calculate the SQI pattern from the CPRs, and discuss its symmetries.

Bezuglyi *et al.* study the following Hamiltonian for the semiconducting part of the JJ [35]:

$$\hat{H} = \left( \frac{\hat{\mathbf{p}}^2}{2m} - E_F \right) \tau_z + \frac{\alpha}{\hbar} (\hat{\mathbf{p}} \times \hat{\mathbf{z}}) \boldsymbol{\sigma} + \mu_B \mathbf{B}_{\parallel} \boldsymbol{\sigma} + \mu_B B_z \sigma_z, \quad (2.40)$$

where  $\boldsymbol{\sigma}$ ,  $\hat{\mathbf{p}}$ ,  $\mathbf{B}_{\parallel}$  lie in the  $x$ - $y$  plane (see Fig.2.6a) and the Nambu basis is used. The Zeeman effect is included via a hyperfine interaction, to not induce a magnetic orbital effect. For the spin-orbit interaction, only the Rashba contribution, with magnitude  $\alpha$ , is taken into account. The superconductors are included by adding  $\Delta e^{\pm i\phi/2}$  at the sides of the semiconductor ( $y > |L/2|$ ). Solving the BdG equation in the quasi-classical approximation ( $\mathbf{p} \approx p_y$ ), they obtain the ABS energies for the short junction limit [35]:

$$\epsilon_p = \pm \Delta \cos \left( \frac{\phi}{2} + \sigma \gamma \right), \quad (2.41)$$

where  $\sigma = \pm 1$  and the Zeeman effect,  $\mathbf{h} = \mu_B \mathbf{B}$ , and spin-orbit interaction,  $\mathbf{w} = \frac{\alpha}{\hbar} (\hat{\mathbf{p}} \times \hat{\mathbf{z}})$ , are contained in  $\gamma$  as:

$$\gamma(\mathbf{h}, \mathbf{w}) = \arcsin \sqrt{\left[ \sum_{l=\pm 1} \frac{1 + l \mathbf{n}_+ \cdot \mathbf{n}_-}{2} \sin^2 \left( \frac{A_+ + l A_-}{2} \right) \right]}, \quad (2.42)$$

$$\mathbf{n}_{\pm} = \frac{\mathbf{h} \pm \mathbf{w}}{|\mathbf{h} \pm \mathbf{w}|}, \quad A_{\pm} = \frac{L}{\xi_s \Delta} |\mathbf{h} \pm \mathbf{w}|.$$

Note that this model only renormalizes the spin splitting. We can then calculate the CPR following eq. 2.33, with  $\tau = 1$  and  $T = 50$  mK, and find the SQI pattern following section 2.2.2.

**Zeeman effect** Considering the Zeeman effect only ( $\mathbf{w} = 0$ ) the expression for  $\gamma$  reduces to [35]:

$$\gamma(\mathbf{h}, 0) = \arcsin[\sin(|\mathbf{h}|L/\xi_s \Delta)] \quad (2.43)$$

The ABS energies and CPR are thus shifted proportional to the magnetic field applied, as presented in Fig.2.9a. Note that the orientation of the magnetic field is not important here. We observe that for  $\gamma = \pi/2$  the CPR frequency (in  $\phi$ ) is doubled, which shows up in the SQI pattern in Fig.2.9b. Once  $\gamma = \pi$ , the CPR switched sign completely, which means that the supercurrent in the JJ is reversed.

This effect is known as a Zeeman-induced  $0 - \pi$  transition, which corresponds to the shift of the minimum in the ABS energy from  $0$  to  $\pi$  phase difference. Generally, it occurs due to the magnetic ordering in the JJ [36–39]. The Zeeman effect induces an energy splitting of the semiconducting bands according to their spin orientation, proportional to the magnetic field applied. Cooper pairs with s-wave pairing in a semiconductor

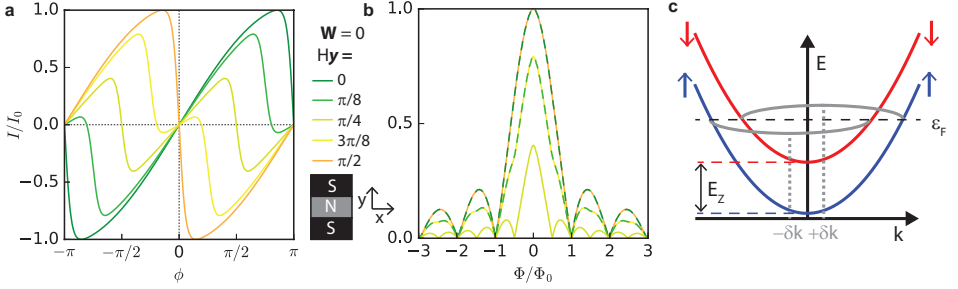


Figure 2.9: **CPR and SQI pattern with Zeeman effect.** **a** Normalized CPR,  $I/I_0(\phi)$ , calculated with the model from Ref. 35 at several magnetic fields,  $H = h(\xi_s \Delta/L)$ , and zero spin-orbit interaction,  $W = w(\xi_s \Delta/L)$ . A schematic of the device is added including the coordinate system used. **b** Normalized SQI pattern for a JJ with a homogeneous current distribution and the CPRs from **a**. **c** Schematic band structure of a 1D semiconductor with the Zeeman effect included. The bands split according to their spin orientation (blue and red) by the Zeeman energy,  $E_Z$ . Cooper pairs that form at the Fermi level  $\epsilon_F$  have a finite momentum of  $\pm\delta k$ .

normally pairs the  $+k, \uparrow$  and  $-k, \downarrow$  electrons. However, at a finite magnetic field, pairing the electrons results in Cooper pairs with a finite momentum  $\pm\delta k$  (Fig. 2.9c) [40]. This finite momentum translates to a spatial dependence of the Cooper pair wavefunction of  $\Delta \sim e^{+i\delta k \cdot x} + e^{-i\delta k \cdot x} = \cos(\delta k \cdot x)$ . The superconducting pairing thus oscillates along the quasiparticle trajectories with typical length of  $1/\delta k$ , leading to the oscillation of the switching current ( $I_c \propto |\Delta|$ ).

**Spin-orbit interaction & Zeeman effect** Adding the spin-orbit interaction to the picture makes the CPR dependent on the direction of the Zeeman field. Therefore, we treat the cases where the Zeeman field is parallel and perpendicular to the effective spin-orbit field, separately. In Fig. 2.10a,b the CPRs and resulting SQI patterns are presented for the perpendicular arrangement. We observe that the first Zeeman induced  $0 - \pi$  transition occurs at a large magnetic field value compared to the Zeeman only case (Fig.2.9). To show this more directly, we plot  $I_c$  obtained from the CPR as a function of magnetic field  $H$  in Fig. 2.10c. The renormalization of the spin splitting (eq. 2.42), causes this distinct behavior.

Next, we move on to the case where the Zeeman field and effective spin-orbit field are oriented parallel. The model of Bezuglyi *et al.* describes a symmetric renormalization of the spin only, by using  $\sigma = \pm 1$ . However, they do not consider that the spin conservation is broken by the spin-orbit interaction, and  $\sigma$  can take different values [41] as schematically shown in the Fermi surfaces in Fig. 2.11a. We heuristically add a Zeeman and SOI dependent shift such that  $\sigma = \frac{\hbar \cdot w}{|\hbar + w|} \pm 1$ . This leads to a phase shift in the CPR (Fig. 2.11b), showing up as an anomalous supercurrent,  $I(\phi = 0) \neq 0$ , as recently observed[42].

The occurrence of this shift and the anomalous supercurrent is confirmed by a numerical calculation by Yokoyama *et al.* [41]. They solve a nominally identical Hamiltonian, but do not use the quasi-classical approximation. The ABS energies are found by representing the BdG equation in terms of a scattering matrix, and extracting its transmission eigenvalues. The scattering matrix itself is obtained with a tight-binding

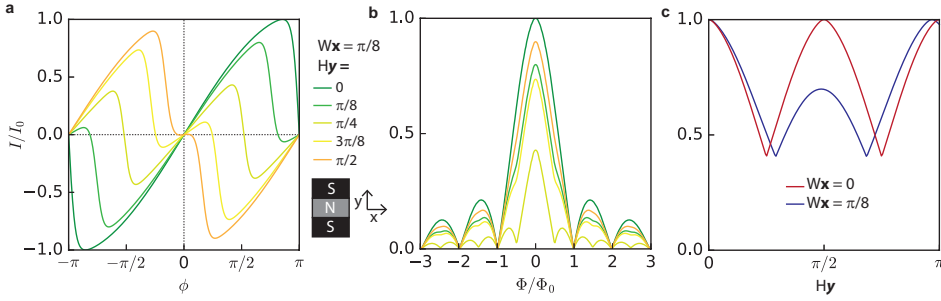


Figure 2.10: **SOI and Zeeman effect, aligned perpendicular.** **a** Normalized CPR,  $I/I_0(\phi)$ , calculated with the model from Ref. 35 at several magnetic fields,  $H = h(\xi_s \Delta/L)$ , with a constant SOI,  $W = w(\xi_s \Delta/L)$ . A schematic of the device is added including the coordinate system used. **b** Normalized SQI pattern for a JJ with a homogeneous current distribution and the CPRs from **a**. **c** Normalized critical current,  $I_c/I_0$ , as a function of magnetic field  $H$ , with and without the SOI indicated.

model of the JJ [41]. We plot their numerical result for the CPR at  $T = 0$ , and  $\tau < 1$  in Fig. 2.11c, and observe the phase shift and anomalous supercurrent.

According to the symmetry breaking terms in table 2.1, this combination of Rashba spin-orbit interaction and  $B_y$  breaks symmetry I. Nevertheless, this is not reflected in the SQI pattern, because the symmetry  $I_{c,+} = I_{c,-}$  is retained (Fig. 2.11b,c). The shape of the SQI pattern can however change drastically dependent on the SOI and Zeeman effect, which is discussed in detail in Ref. 43.

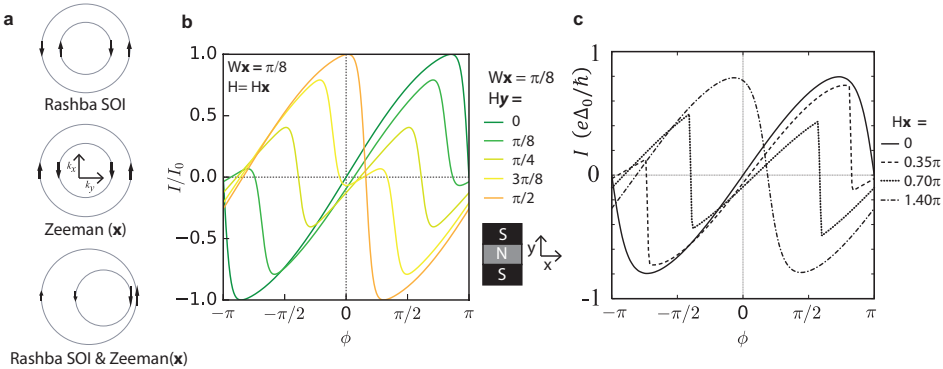


Figure 2.11: **SOI and Zeeman effect, aligned parallel.** **a** Schematic representation of the Fermi surfaces in the junction with SOI and the Zeeman field applied. The arrows denote the spin states along the direction of current,  $y$ . A schematic of the device is added including the coordinate system used. **b** Normalized CPR,  $I/I_0(\phi)$ , at several magnetic fields,  $H = h(\xi_s \Delta/L)$ , with a constant SOI,  $W = w(\xi_s \Delta/L)$ . The CPR is calculated with the model from Ref. 35, where a shift in  $\sigma$  is heuristically added. **c** Numerically calculated supercurrent,  $I$ , versus phase difference,  $\phi$ , in a JJ with SOI as well as Zeeman fields,  $H$ , indicated. This figure is taken from Ref. 41.



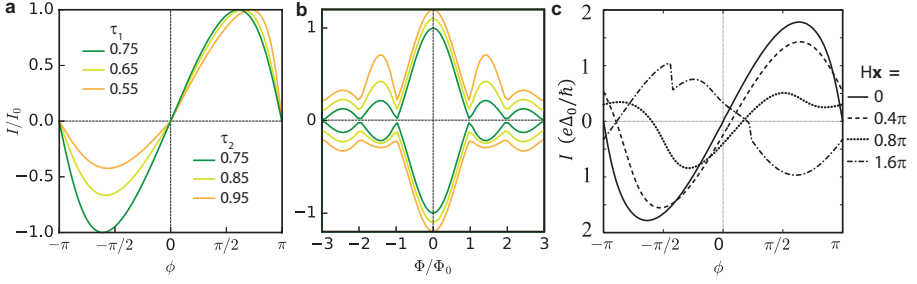


Figure 2.12: **SQI coupling** **a** Normalized CPR,  $I/I_0(\phi)$ , calculated at  $T = 50$  mK and  $\Delta = 1$  meV from eq.2.33, for the transparencies for positive and negative  $\phi$  as indicated. **b** Normalized SQI pattern for a JJ with a homogeneous current distribution and the CPRs from **a**. The lines are offset by 0.1 for clarity. **c** Numerically calculated CPR in a system with SOI and coupling between the ABSs, for different Zeeman fields. This figure is adapted from Ref. 41.

**Coupling Andreev bound states** Finally, we discuss a term that does break both symmetries  $I(\phi) = I(-\phi)$  and  $I_{c,+} = I_{c,-}$ , corresponding to breaking symmetry  $I$  in the SQI pattern. For example, varying  $\tau$  as a function of  $\phi$  leads to an asymmetry in the positive and negative CPR amplitudes we are looking for. Figure 2.12a shows such CPRs, with the corresponding SQI patterns presented in Fig 2.12b, where  $I_c(+B_z) = I_c(-B_z)$  is clearly broken. Such a  $\phi$  - dependent transparency can occur due to coupling of ABSs (with different transparencies). Yokoyama *et al.* investigate this and found the CPR presented in Fig. 2.12, where  $I_{c,+} = I_{c,-}$  is indeed broken. Experimentally, this effect has been observed in a few mode nanowire Josephson junction recently [44].

# 3

## MATERIALS, FABRICATION AND MEASUREMENTS

*First, we briefly discuss the semiconducting materials that are used in this thesis. Then, the most crucial steps in the nanofabrication processes are described. Finally, a typical measurement setup is presented.*

### 3.1. MATERIALS & FABRICATION

The semiconducting materials used in this thesis can be divided in two categories. Firstly, we consider low dimensional nanostructures that are grown individually by vapor-liquid-solid (VLS) technique in the group of prof. Erik Bakkers at Eindhoven University of Technology. Secondly, two-dimensional (2D) heterostructures are described, where thin layers are grown on a substrate by molecular beam epitaxy (MBE) in the groups of Marko Sokolich at HRL and prof. Michael Manfra at Purdue University. The standard nanofabrication processes used for fabricated devices from the different materials, are discussed in Refs. 45, 46 and Ref. 47. Here we will focus only on the most crucial steps of the fabrication.

#### 3.1.1. LOW DIMENSIONAL NANOSTRUCTURES

##### GeSi NANOWIRES

The germanium (Ge) Silicon (Si) core-shell nanowires, with a typical diameter of 10-20 nm, are grown by VLS with the use of a gold catalyst particle. Because of the large valence band offset between Ge and Si [48], a quantum well is formed that hosts a one-dimensional hole gas (Fig. 3.1) [49]. The lattice mismatch between Ge and Si (Fig. 3.3a) induces strain in the Ge core, which has important consequences for the electron transport as we encounter in chapter 4. Recently, hole mobilities up to  $4200 \text{ cm}^2/\text{Vs}$  are reported for nanowires with a [110] growth direction [50].

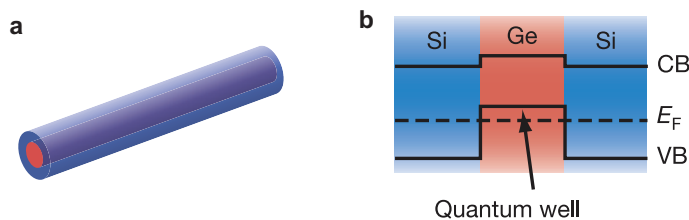


Figure 3.1: **Ge-Si core-shell nanowires.** **a** Schematic representation of Ge (red) -Si (blue) core-shell nanowire. **b** Schematic energy diagram of the valence band (VB), conduction band (CB) and Fermi energy ( $E_F$ ) in the nanowire. Due to the valence band offset a quantum well forms. Both are taken from Ref. 51.

##### INSB FLAKES

There are several techniques to grow small indium antimonide (InSb) 2D structures, all using VLS growth starting from a gold catalyst particle. Firstly, an indium phosphide (InP) and/or indium arsenide (InAs) stem can be grown, where after the material fluxes in the MBE process are tuned such that the InSb growth continues in a 2D manner [52]. This is very similar to the growth of InSb nanowires [53], and an example of such a nanosheet is shown in Fig. 3.2a. Secondly, the growth can be performed without a stem (Fig. 3.2b), in literature called nanosails [54]. Thirdly, flakes can be formed from two nanowires [55]. By patterning the catalyst particles in trenches on an InP substrate, the nanowires grow under a relative angle. Proper lateral alignment of the nanowires then causes them to coalesce as shown in the upper panel of Fig. 3.2c. After that, the

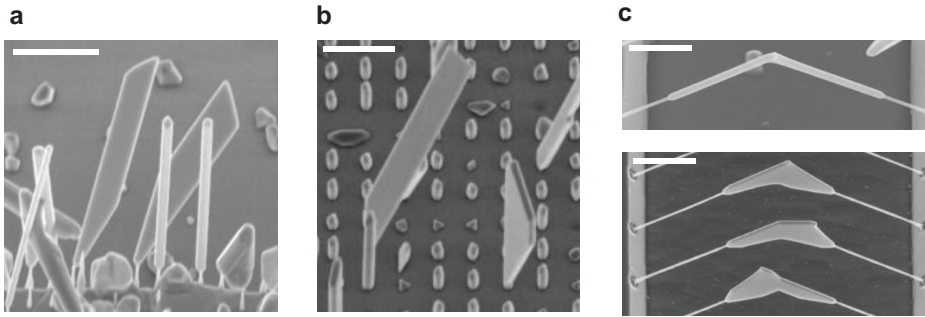


Figure 3.2: **Growth of InSb flakes.** **a** Scanning electron microscope (SEM) image of a nanosheet grown on top of a stem. **b** SEM image of the stemless growth of nanosails. **c** The upper image shows two nanowires coalescing because they are grown under a relative angle. The bottom image shows the final result of the growth. The scalebar is  $1\ \mu\text{m}$  in all panels. All images are courtesy of Stijn Balk and Sasa Gazibegovic.

growth continues in the plane spanned by the two nanowires (lower panel Fig. 3.2c). We characterized the electronic transport in the small 2D structures from all three growth processes and found all have a electron mobility in the range of  $5.000 - 10.000\ \text{cm}^2/\text{Vs}$ . The first two approaches have the disadvantage of resulting in relatively narrow rectangular structures. The third approach however can be used to make larger and square shaped structures, which offers more flexibility in device geometries and fabrication. Therefore, we choose the flakes grown with the third process to study in chapter 7.

### FABRICATION

For both the nanowires and flakes, the first crucial step in the fabrication process is to transfer them from the growth chip on to a suitable substrate. This transfer is done with a micromanipulator, either in the optical microscope [56] or in a scanning electron microscope (SEM). The material of the substrate chosen, depends on subsequent processing steps, and the device geometry. A common choice is a conducting Si substrate with a SiO dielectric layer, such that the substrate can be used as a global electrostatic bottom gate. For the Ge-Si nanowires however, we use a SiN dielectric, because of its resilience to the buffered HF etch that is performed before depositing metallic contacts. After the transfer, pre-patterned markers on the substrate enable us to locate the nanostructures with a SEM, and continue fabricating the devices.

Another crucial step in the fabrication process is cleaning the surface before depositing a superconducting contact. To create these contacts to the Ge-Si nanowires, first the SiO, present on the shell, is etched by a repeated buffered HF etch (3 times 5s dip), with pauses of 2 min in between to oxidize the uncovered Si in air. The chip is then transferred in water to an electron beam evaporator, where 60 nm of the superconductor Aluminium (Al) is deposited. Finally, we anneal the chip for 150 s at  $190\ ^\circ\text{C}$  in a rapid thermal annealer. The duration and temperature are chosen such that the contact resistance decreases, but the Al does not diffusive all the way through the nanowire. We shared our recipe with other groups, that then also managed to make superconducting

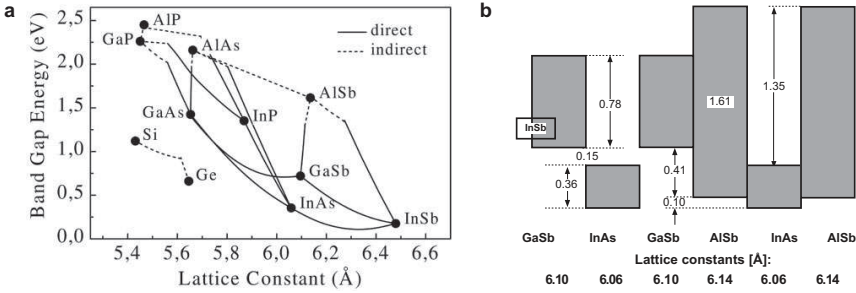


Figure 3.3: **Band gaps and lattice constants.** **a** Band gap (direct or indirect) energy versus lattice constant for the indicated materials, taken from Ref. 63. **b** Band gaps and band offsets for a heterostack of III/V materials as indicated. This figure is adapted from Ref. 64.

contacts [57, 58], and reported the formation of a superconducting alloy made from Ge, Si and Al [59].

To induce superconductivity in the InSb flakes we exploit a process that is developed for InAs [60] and InSb [61] nanowires. The contact area is etched in a saturated ammonium sulfide solution that is heavily diluted with water (ratio 1:200), for 30 min at a temperature of 60°C. The sulfur (S) solution removes the native oxides, but also replaces the Sb atoms with S atoms in the lattice, which could lead to doping of the surface [62]. Then, the chip is transferred to an ultra high vacuum system, where a short argon plasma cleaning step and the superconductor niobium titanium nitride (NbTiN) is deposited.

### 3.1.2. 2D HETEROSTRUCTURES

All 2D heterostructures used in this thesis consist of elements from column III and V in the periodic table. The layers are grown by MBE, ideally in a single crystal without any defects. To do so, the lattice constants of the different layers (Fig. 3.3) have to be as close as possible to each other. In order to confine electrons in a 2D quantum well, a layer of the material of interest is sandwiched between to insulating layers. The insulating layers typically have a large band gap, and a band offset such that the carriers are confined in the layer of interest (Fig. 3.3b).

#### INAs QUANTUM WELLS

InAs quantum wells are generally either consist of AlSb or In(Ga,Al)As barriers, grown on a GaSb or InP substrate, respectively. In the first case, the wavefunction is predominantly located in the InAs because AlSb has a large band gap, where for the latter the wavefunction has a significant weight in the In(Ga,Al)As barriers [65]. This difference reflects for example in the Landé  $g$ -factor, since a value of 11 is found for AlSb [66] and 4 for In(Ga,Al)As barriers [67]. In this thesis we study three different InAs quantum wells, their layer structure is presented in Fig. 3.4. The stack in Fig. 3.4a is a double quantum well, since both an 2D electron gas and 2D hole gas can be formed in the InAs and GaSb layer, respectively [68]. The second heterostack (Fig. 3.4b) is very similar to the first, but has an InAs quantum well only. The third stack is different from the other

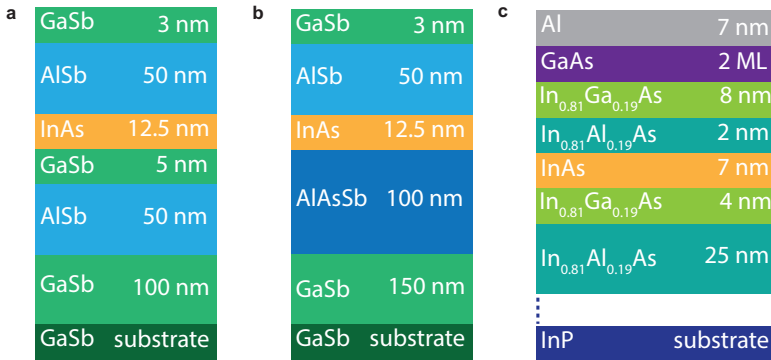


Figure 3.4: **InAs quantum well heterostructures.** The material and thickness is indicated for every layer in **a,b,c**. In **c** there are two monolayers (ML) of GaAs grown in between the quantum well and the Al.

two because a superconducting material is included in it, a thin layer of Al is grown by MBE on top (Fig. 3.4c). This InAs epi Al quantum well exhibits high quality induced superconductivity, because of the oxide and defect free interface between the quantum well and the superconductor [69, 70].

### FABRICATION

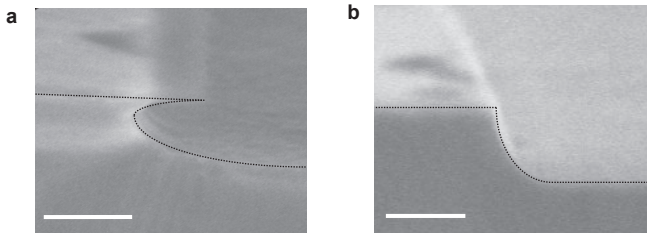


Figure 3.5: **Etch profiles InAs epi Al.** SEM images of the cross section of an InAs epi Al wafer after the mesa etch **a** without and **b** with additional Transene-D etches during the mesa etching. The etch profile is highlighted by the dashed line, and the scale bar equals 100 nm.

Isolating a part of the 2D electron gas (the mesa) is the first, and for us most crucial step in the fabrication process. For the stacks with AlSb, the top barrier is etched with a solution based on photoresist developer (MF321:H<sub>2</sub>O, 1:3) for 13 s. Since this solution does not etch InAs, it serves as an etch stop, that layer is subsequently removed by Argon milling. For the InAs epi Al stack, first the Al is removed with a Transene-D etch (12 s at 48.2°C), for which the two monolayers of GaAs serve as an etch stop. Then, the mesa is etched with a solution of citric acid, phosphoric acid and hydrogen peroxide, diluted in water (ratio 55:3:3:220) with rate of 30 nm/min [71]. However, following this procedure leads to an undesired etch profile, because of significant etching under the Al layer (Fig. 3.5a). Covering such a profile with dielectric material is hard, since the overhanging Al masks the mesa underneath. The top gate metal, deposited on top of

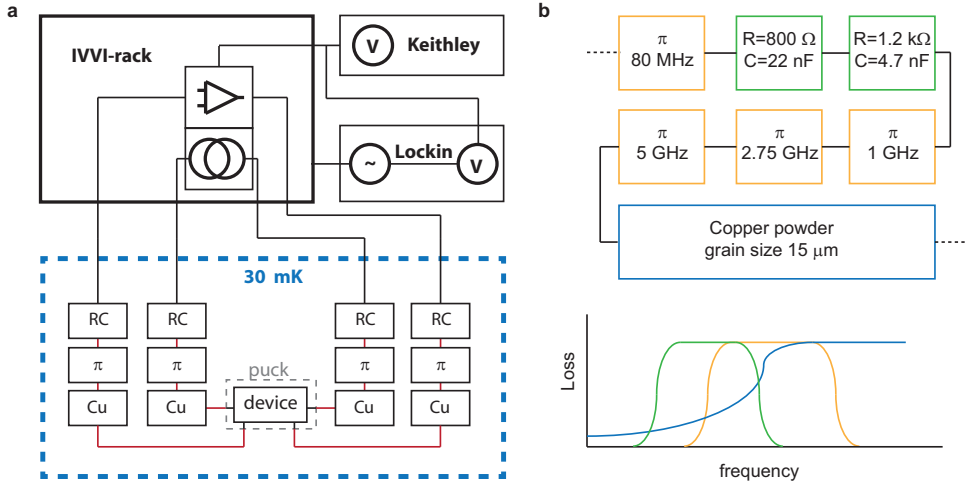


Figure 3.6: **Measurement setup and filtering schematics.** **a** The device and filtering are mounted on the refrigerator plate with the lowest temperature. The filtering consists of RC-  $\pi$ - and copper (Cu) powder filters. The DC lines from the copper powder filters to the device are shielded with copper braid. The sources and amplifiers are located in the IVVI rack and voltages can be measured with either a Keithley or a Lock in amplifier. **b** The upper panel depicts the filtering of the DC lines in detail, with 4  $\pi$  filters with a pass band up to the frequency indicated, the RC filters with a cut off frequency of 9 kHz and 28.2 kHz, and the copper powder filter. The lower panel schematically shows the frequency range the different filters cover.

the dielectric, could then easily make unwanted contact with the mesa. We solve this by adding two intermediate Transene-D dips (2 s) to the mesa etch process, and obtain an etch profile without overhang (Fig. 3.5b). Furthermore, we found that depositing dielectric material on a region with a shallow mesa etch depth of 100 nm could induce carriers and short the device to its environment. To keep the mesa isolated, an etch depth of 200 nm is used.

### 3.2. MEASUREMENT SETUP

All measurement reported in this thesis are either done in either an Oxford Triton dilution refrigerator or a Janis He-3 refrigerator, with base temperatures  $T$  of 30 mK and 300 mK, respectively [72]. The electronic setup for a four point current bias measurement in the Oxford system is schematically presented in Fig. 3.6a. A home build IVVI rack [73] contains the current and voltages sources and amplifiers. The measurement apparatus used is either a Keithley (2000 or 2700) for DC signals, or a lock in amplifier (SR830) for AC excitations on the order of 10 Hz. All DC lines in the fridge have three filtering stages at  $T = 30$  mK, RC-filters,  $\pi$ -filters and copper powder filters. The parameters of the different filter stages are presented in the upper panel of Fig. 3.6d. Additionally, in the lower panel a schematic diagram depicts which part of the frequency spectrum is suppressed by each stage. The DC lines are shielded with copper braid in between the filter stages and from the last filter stage to the puck (see red lines in Fig. 3.6a), which hosts the printed circuit board with the device.

# 4

## SPIN-ORBIT INTERACTION AND INDUCED SUPERCONDUCTIVITY IN A ONE-DIMENSIONAL HOLE GAS

*Low dimensional semiconducting structures with strong spin-orbit interaction (SOI) and induced superconductivity attracted much interest in the search for topological superconductors. Both the strong SOI and hard superconducting gap are directly related to the topological protection of the predicted Majorana bound states. Here we explore the one-dimensional hole gas in germanium silicon (Ge-Si) core-shell nanowires (NWs) as a new material candidate for creating a topological superconductor. Fitting multiple Andreev reflection measurements shows that the NW has two transport channels only, underlining its one-dimensionality. Furthermore, we find anisotropy of the Landé g-factor, that, combined with band structure calculations, provides us qualitative evidence for direct Rashba SOI and a strong orbital effect of the magnetic field. Finally, a hard superconducting gap is found in the tunneling regime, and the open regime, where we use the Kondo peak as a new tool to gauge the quality of the superconducting gap.*

---

This chapter has been published as, *Spin-orbit interaction and induced superconductivity in a one-dimensional hole gas*, Folkert K. de Vries, Jie Shen, Rafal J. Skolasinski, Michal P. Nowak, Daniel Varjas, Lin Wang, Joost Ridderbos, Floris Zwanenburg, Ang Li, Sebastian Koelling, Marcel A. Verheijen, Erik P. A. M. Bakkers and Leo P. Kouwenhoven in *Nano Letters* 18 (10), 6483-6488 (2018)



### 4.1. INTRODUCTION

The large band offset and small dimensions of the Ge-Si core-shell nanowire (NW) lead to the formation of a high-quality one-dimensional hole gas [49, 50]. Moreover, the direct coupling of the two lowest-energy hole bands mediated by the electric field is predicted to lead to a strong direct Rashba SOI (SOI) [16, 17]. The bands are coupled through the electric dipole moments that stem from their wavefunction consisting of a mixture of angular momentum (L) states. On top of that, the spin states of that wavefunction are mixed due to heavy and light hole mixing. Therefore, an electric field couples via the dipole moment to the spin states of the system and causes the SOI. This is different from Rashba SOI, which originates from the coupling of valence and conduction bands. The predicted strong SOI is interesting for controlling the spin in a quantum dot electrically [74, 75]. Combining this strong SOI with superconductivity is a promising route towards a topological superconductor [76, 77]. Signatures of Majorana bound states (MBSs) have been found in multiple NW experiments [78, 79]. An important intermediate result is the measurement of a hard superconducting gap [61, 80], which ensures the semiconductor is well proximitized as is needed for obtaining MBSs.

### 4.2. EXPERIMENTAL SETUP

Here we study a superconducting quantum dot in a Ge-Si NW. The scanning and transmission electron microscopy images of the device (Fig. 4.1a-b) show a Josephson junction of  $\sim 170$  nm length. The quantum dot is formed in between the contacts. The Ge-Si core-shell nanowires were grown by the vapor-liquid-solid (VLS) method as discussed in detail in the Supporting Information of Ref. 50. The NW has a Ge core with a radius of 3 nm. The Ge crystal direction is found to be [110], in which hole mobilities up to  $4600 \text{ cm}^2/\text{Vs}$  are reported [50]. The elemental analysis in Fig. 4.1c reveals a pure Ge core with a 1 nm Si shell and a 3 nm amorphous silicon oxide shell around the wire. Superconductivity is induced in the Ge core by aluminium (Al) leads [51], and crucially, the device is annealed for a short time at a moderate temperature [57, 58]. We believe that the high temperature causes the Al to diffuse in the wire, therefore enhancing the coupling to the hole gas. Note that we do not diffuse the Al all the way through, since we pinch off the wire (Fig. 4.S7) and there is no Al found in the elemental analysis (Fig. 4.1c). Two terminal voltage bias measurements are performed on this device in a dilution refrigerator with an electron temperature of  $\sim 50$  mK.

### 4.3. SUPERCONDUCTING QUANTUM DOT

To perform tunneling spectroscopy measurements the bottom gate voltage  $V_{\text{bg}}$  is used to vary the barriers of the quantum dot and alter the density of the holes as well. From a large source-drain voltage,  $V$ , measurement (Fig. 4.S7), we estimate a charging energy  $U$  of 12 meV, barriers' asymmetry of  $\Gamma_1/\Gamma_2 = 0.2-0.5$ , where  $\Gamma_{1(2)}$  is the coupling to the left (right) lead, and a lever arm of  $0.3 \text{ eV}/V$ . In Fig. 4.1d, the differential conductance  $dI/dV$  as a function of a  $V$  versus  $V_{\text{bg}}$  reveals a superconducting gap ( $2\Delta = 380 \mu\text{eV}$ ) and several Andreev processes within this window. Additionally, an even-odd structure shows up in both the superconducting state at low  $V$  and normal state at high  $V$ , which is related to the even or odd parity of the holes in the quantum dot. The even-odd structure

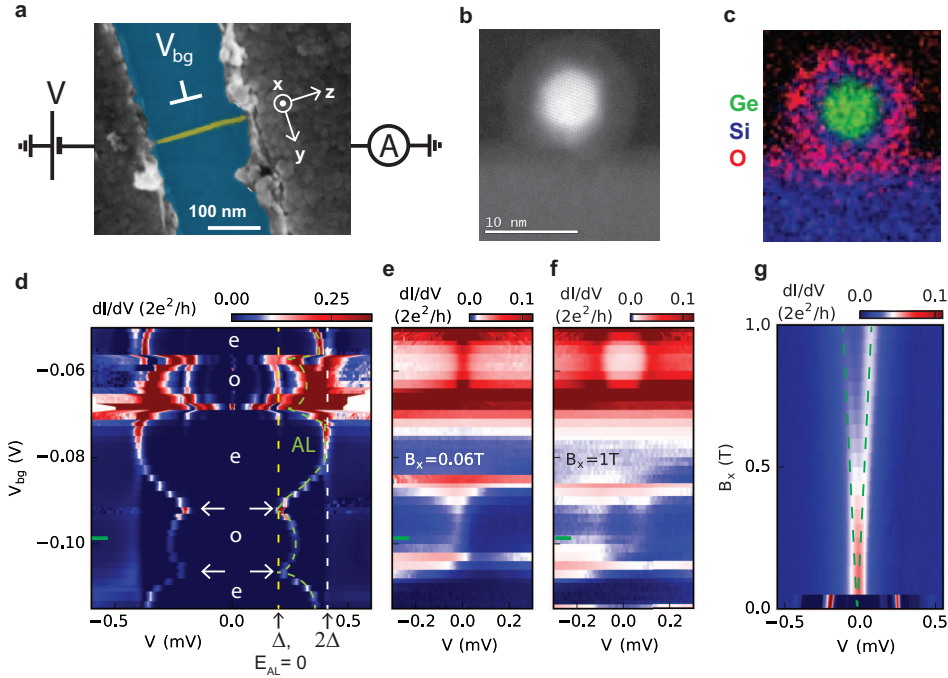


Figure 4.1: **Superconducting quantum dot device.** **a** False colored scanning electron microscope image of the device with the NW (yellow) with aluminum contacts (gray) on a Si/Si<sub>x</sub> wafer (blue). The magnetic field axes, voltage bias measurement setup, and global bottom gate are indicated. **b** Transmission electron microscope (TEM) image of the cross section of the NW. **c** Energy dispersive X-ray spectroscopy of the area displayed in **b**. The colors represent different elements, Ge is green, Si blue and oxygen (O) is red, respectively. The Ge-Si core-shell wire is capped by a SiO<sub>x</sub> shell. **d** Voltage bias tunneling spectroscopy measurement of the superconducting quantum dot as the bottom gate voltage  $V_{bg}$  is altered. The superconducting gap, an Andreev level (AL) and multiple Andreev reflections appear as peaks in differential conductance ( $dI/dV$ ). The AL,  $\Delta$  and  $2\Delta$  are marked by the dashed green, yellow and white lines, respectively. The even or odd occupation is indicated, and the kink in the observed Andreev level is highlighted by the arrows. **e-f** Same measurement as **d** with a magnetic field,  $B$ , applied perpendicular to the substrate ( $x$ -direction) of 60 mT and 1 T, respectively. A zero bias Kondo peak is observed as the quantum dot is occupied by an odd number of electrons. At  $B = 1$  T, the resonance is split due to the Zeeman effect. **g** Linear splitting of the Kondo peak at  $V_{bg} = -0.098$  V as a function of  $B$ . The Zeeman effect splits the spinful Kondo peak, which is indicated by the dashed green line.

persists as we suppress the superconductivity in the device by applying a small magnetic field (60 mT) perpendicular to the substrate (Fig. 4.1e). A zero bias peak appears when the quantum dot has odd parity. This is a signature of the Kondo effect [5, 6]. When increasing the magnetic field to 1 T, the Kondo peak splits due to the Zeeman effect by  $2g\mu_B B$ . The energy splitting of the two levels is linear as shown in Fig. 4.1g, and thus can be used to extract a Landé  $g$ -factor,  $g$ , of 1.9. In the remainder of the chapter, we will discuss the three magnetic field regimes of Fig. 4.1d-f (0 T, 60 mT and 1T, respectively) in more detail.

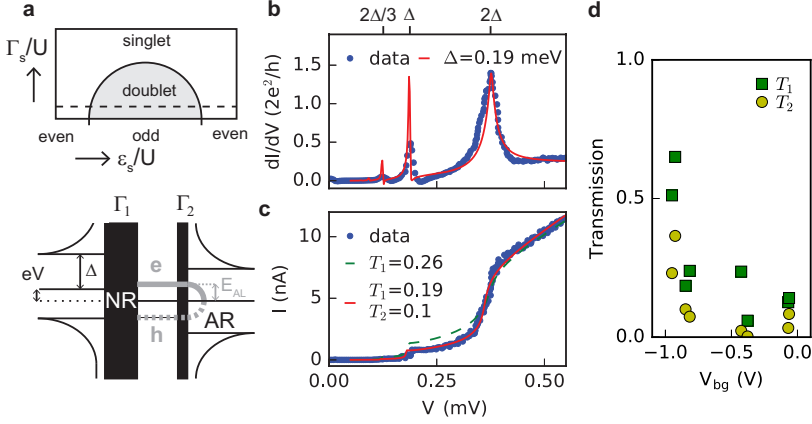


Figure 4.2: **Andreev processes in the quantum dot.** **a** In the top panel a phase diagram of the ground state in the superconducting quantum dot is sketched as a function of the quantum dot energy,  $\epsilon_0$ , versus the coupling to the superconducting reservoir  $\Gamma_s$ , both normalized to the charging energy,  $U$ . Because of the large  $U$  we expect to trace the dashed line. The bottom panel shows the Andreev level (dashed gray line) with energy  $E_{AL}$  that is formed by Andreev Reflection (AR) at one side and Normal Reflection (NR) at the other side of the dot. The reflection processes are different due to asymmetric barriers  $\Gamma_1$  and  $\Gamma_2$ , indicated as the barrier width. The density of states in the NW is probed by the superconductor on the left side by doing voltage bias tunneling spectroscopy. **b** Tunneling spectroscopy measurement at  $V_{bg} = -0.85$  V. The first- and second-order multiple Andreev reflection are observed. A two-mode model fits the data well with  $\Delta = 190 \mu\text{eV}$ . **c** Measured current of **b**. The data is fitted with a single- and two-mode model. The latter resembles the data better and is therefore used to extract transmission values. **d** Transmission of the first and second mode,  $T_1$  and  $T_2$ , extracted from the fit of multiple Andreev reflections different  $V_{bg}$ . The transmission increases significantly below  $V_{bg} = -0.8$  V.

#### 4.4. ANDREEV PROCESSES

The resonance that disperses with  $V_{bg}$  in Fig. 4.1d is an Andreev Level (AL), which is the energy transition from the ground to the excited state in the dot [81, 82]. The ground state of the dot switches between singlet and doublet if the occupation in the dot changes, as sketched in the phase diagram in the top panel of Fig. 4.2a. Since our charging energy is large, we trace the dashed line in the phase diagram. The AL undergoes Andreev reflection at the side of the quantum dot with large coupling ( $\Gamma_2$ ) and normal reflection at the opposite side that has lower coupling ( $\Gamma_1$ ), as schematically drawn in bottom panel of Fig. 4.2a. The superconducting lead with the low coupling serves as a tunneling spectroscopy probe of the density of states. To be more precise, the coherence peak of the superconducting gap probes the Andreev level energy,  $E_{AL}$ . For example, if  $E_{AL} = 0$ , we measure it at  $eV = \Delta$ , the resonance thus has an offset of  $\pm\Delta$  in the measurement in Fig 4.1d. The ground state transition is visible as a kink of the resonance at  $V = \Delta$  at  $V_{bg} = -0.09$  and  $-0.11$  mV. At a more negative  $V_{bg}$  the coupling of the hole gas to the superconducting reservoirs is strongly enhanced. This eventually leads to the observation of both the DC and AC Josephson effects (Fig. 4.S8).

In the upper part of Fig. 4.1d, we measure multiple Andreev reflection (MAR): resonances at integer fractions of the superconducting gap. Fig. 4.2b presents a line trace

at  $V_{bg} = -0.85$  V that shows the gap edge and first- and second- order Andreev reflection. Fitting the differential conductance [83, 84] (see supplementary material) allows us to extract  $\Delta = 190 \mu\text{eV}$ , close to the bulk gap of Al. We also fit the measured current to extract the transmission of the spin degenerate longitudinal modes in the NW (Fig. 4.2c) [85, 86]. The two-mode fit resembles the data better than the single-mode fit. Also, we checked that fitting with more than two modes results in  $T = 0$  outcomes for the extra modes. Therefore the first provides us with an estimate for the transmission in the two modes,  $T_1$  and  $T_2$ . We interpret the two modes as two semiconducting bands in the NW. The MAR fitting analysis is repeated at different  $V_{bg}$ , and the resulting  $T_1$  and  $T_2$  are plotted in Fig. 4.2d. The strong increase of the transmission below  $V_{bg} = -0.8$  V is attributed to the increase of the Fermi level, and  $\Gamma_1$  and  $\Gamma_2$ .

## 4.5. LANDÉ G-FACTOR ANISOTROPY AND SPIN-ORBIT INTERACTION

4

The Landé  $g$ -factor  $g$  is investigated further by measuring the Kondo peak splitting as a 0.9 T magnetic field is rotated from  $y$ - to  $z$ -,  $x$ - to  $z$ - and  $x$ - to  $y$ -direction as presented in the second row of Fig. 4.3a-c. Interestingly, we find a strong anisotropy of the Kondo peak splitting and accordingly of  $g$  at  $V_{bg} = -0.79$  V and  $V_{bg} = -0.82$  V; see the bottom row Fig. 4.3a-c and Fig. 4.S10, respectively. Both directions perpendicular to the NW show a strongly enhanced  $g$ . Similar anisotropy has been reported before in a closed quantum dot, where  $g$  is even quenched in the  $z$ -direction [87–89]. In our experiment, the highest  $g$  of 3.5 is found when the magnetic field is pointed perpendicular to the NW and almost perpendicular to the substrate.

On the contrary, at a  $V_{bg} = -0.5$  V we find an isotropic  $g$  (bottom row of Fig. 4.3a-c), all of which have a value of around 2. The anisotropies at different  $V_{bg}$  are summarized in Fig. 4.3d. The strong anisotropy seems to set in around  $V_{bg} = -0.7$  V. This sudden transition from isotropic to anisotropic  $g$ , which has not been observed before in a quantum dot system, is correlated with the increase in transmission in Fig. 4.2d. We speculate that the change from isotropic to anisotropic behavior is related to the occupation of two bands in the NW. To test this hypothesis and get an understanding of the origin of the anisotropy, we theoretically model the band structure of our NW and focus on the two lowest bands.

We use the model described in Ref. 16 and apply it to our experimental geometry (see supplementary material for details). Simulating the device as an infinite wire, we first consider the anisotropy of  $g$  between the directions parallel and perpendicular to the NW. We find that there are two contributions to the anisotropy: the Zeeman and the orbital effect of the magnetic field [18, 90]. The anisotropy of the Zeeman component is similar for the two lowest bands, where for the orbital part the anisotropy differs strongly. The anisotropy of the total  $g$  therefore shows a strong difference for the two lowest bands (Fig. 4.S2 and Fig. 4.S3). This agrees qualitatively with earlier predictions[17], but we find additionally that strain lifts the quenching of  $g$  along the NW such that  $g_{\parallel}/g_{\perp} \sim 2$ , in agreement with our measurements. From these observations, we conclude that the observed isotropic and anisotropic  $g$  with respect to the NW-axis is due to the orbital effect.

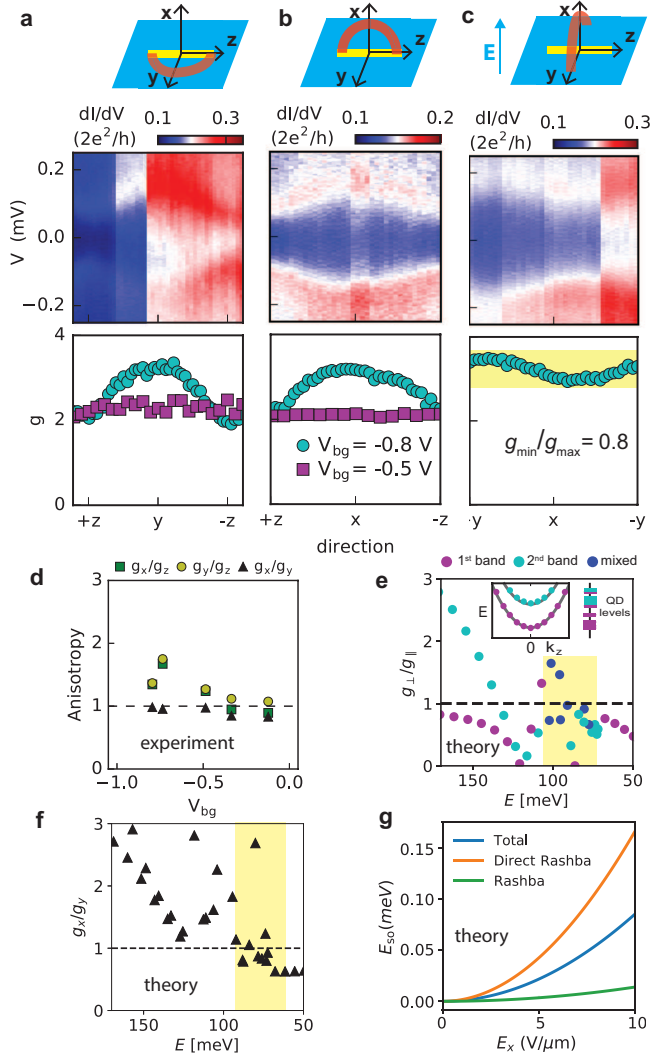


Figure 4.3: **Landé g-factor anisotropy and spin-orbit interaction.** **a-c** Rotations of the magnetic field with a 0.9 T magnitude in the  $yz$ -,  $xz$ - and  $xy$ -plane, respectively, at  $V_{bg} = -0.79$  V. The upper panel shows the schematic of the device and the magnetic field rotation performed. The differential conductance data is plotted in the center panel, the splitting of the Kondo peak changes as the angles are swept. The sudden changes in conductance are due to small switches in  $V_{bg}$ . The lower shows the extracted  $g$  of the center panel in cyan and  $g$  at  $V_{bg} = -0.5$  V in magenta. For the  $xy$ -plane the anisotropy is highlighted and calculated. **d** Summary of the measured anisotropies of  $g$  at different  $V_{bg}$ . **e** Simulation result of the quantum dot. The colors represent the band from where the quantum dot level predominantly stems. The highlighted part shows a similar behaviour in the anisotropy values as the data in **d**. The inset depicts a schematic representation of the energy ordering of the quantum dot levels originating from two bands along the NW. **f** Simulation as in **e**, now with an applied electric field of  $10$  V/ $\mu$ m. The SOI causes anisotropy with respect to the electric field direction as  $g_x$  is pointed perpendicular and  $g_y$  parallel to the electric field. The anisotropy increases as the Fermi level is raised. The same range as in **e** is highlighted. **g** Simulated spin-orbit energies for the first band ( $k = 0$ ) of the infinite wire model as a function of electric field along the  $x$ -direction. The direct Rashba term is the leading contribution.

In addition, we include the confinement along the NW, such that a quantum dot is formed and the energy levels are quantized in the  $z$ -direction. Besides the lowest energy states studied before, [75, 87] we also consider a large range of higher quantum dot levels. In the regime where two bands are occupied, we observe that the quantum dot levels originating from the first and second band have a unique ordering as a function of Fermi energy, this situation is sketched in the inset of Fig. 4.3e. We also find that some of the quantum dot levels are a mixture of the two bands (Fig. 4.S5), resulting in a different anisotropy for each quantum dot level. In the simulation results (Fig. 4.3e and Fig. 4.S6), the anisotropy values are colored according to the band they predominantly originate from. To compare the simulation with the measured data, we note that a more negative  $V_{bg}$  in the experiment increases the Fermi level for holes  $E$ . In the simulation we observe a regime in  $E$  (highlighted in Fig. 4.3e), where the anisotropy  $g_{\perp}/g_{\parallel}$  is around 1 and goes up toward 2 as  $E$  increases. This behaviour qualitatively resembles the measurement of  $g_x/g_z$  and  $g_y/g_z$  in Fig. 4.3d.

Now we turn to the magnetic field rotation in the  $xy$ -plane, the two directions perpendicular to the NW that are parallel and perpendicular to the electric field induced by the bottom gate. The measured anisotropy is  $g_{min}/g_{max} = 0.8$  (Fig. 4.3c). The maximum  $g$  of 3.5 is just offset of the  $y$ -direction, which is almost parallel to the electric field. This anisotropy with respect to the electric field direction is a signature of SOI [87, 88]. As discussed before, the Ge-Si NWs are predicted to have both Rashba SOI and direct Rashba SOI [17, 75]. The electric field could also cause anisotropy via the orbital effect or geometry, due to an anisotropic wavefunction. However we can rule that out since our simulations show that the wavefunction does not significantly change as electric field is applied (Fig. 4.S4). In the simulation (Fig. 4.3f) with a constant electric field of  $10 \text{ mV}/\mu\text{m}$ , we observe anisotropy of  $g$  parallel ( $g_x$ ) and perpendicular ( $g_y$ ) to the electric field. Similar to our data the anisotropy starts below 1 and goes to 1 as the Fermi level is increased. The spread in the anisotropy values is due to the mixing of the bands for each quantum dot level. Furthermore, we calculated the magnitude of the Rashba and direct Rashba contribution to the SOI using the infinite wire model and find the direct Rashba SOI is dominating in the small diameter nanowires of our study (Fig. 4.3g). This agrees with the effective Hamiltonian derived in Ref. 17, which predicts that the direct Rashba SOI dominates in NWs with a Ge core of 3 nm radius. To summarize, we observe anisotropy with respect to the electric field direction that is caused by SOI, which is likely for the largest part due to the direct Rashba SOI.

## 4.6. HARD SUPERCONDUCTING GAP

Finally, in Fig. 4.4, we take a detailed look at the superconducting gap as a function of magnetic field. We find the critical magnetic field  $B_c$  for different directions:  $B_{c,z} = 220 \text{ mT}$  (Fig. 4.4a),  $B_{c,y} = 220 \text{ mT}$  (Fig. 4.4b), and  $B_{c,x} = 45 \text{ mT}$  (Fig. 4.1g and Fig. 4.S9), consistent with an Al thin film. Future devices could be improved by using a thinner Al film to increase the critical magnetic field [69]. In this case, the topological phase could be reachable, with the measured  $g$  of 3.5 [77]. In the tunneling regime at  $V_{bg} = -0.12 \text{ V}$ , we observe a clean gap closing (Fig. 4.4a). The conductance inside the gap is suppressed by two orders of magnitude, signaling a low quasiparticle density of states in the superconducting gap. This large conductance suppression remains as the gap size decreases

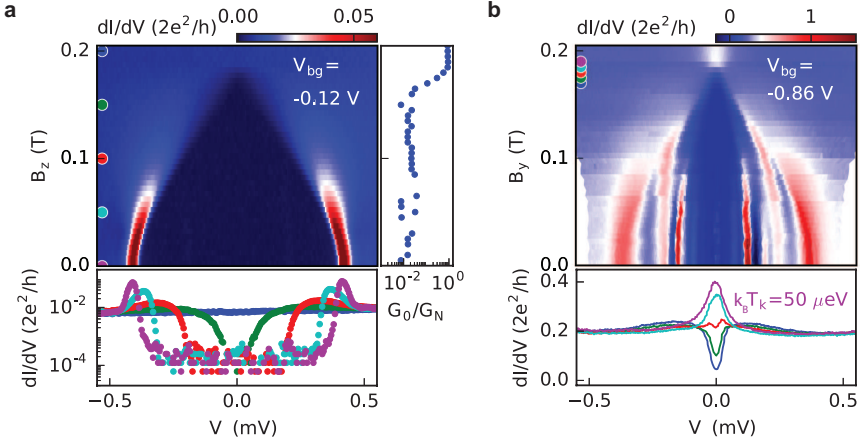


Figure 4.4: **Hard superconducting gap.** **a** Closing of the superconducting gap, as  $B$  is ramped up in the  $z$ -direction. The line traces below are taken at 50 mT intervals and show the induced superconducting gap. The vertical line trace shows the conductance at  $V=0$  V normalized to the conductance extracted at  $V=0.5$  mV. A two orders of magnitude conductance suppression is observed. **b** The superconducting gap closes, and a Kondo peak appears as the magnetic field is increased in the  $y$ -direction. The resonances within the gap stem from Andreev processes. The line traces depict the transition from the superconducting gap to the Kondo peak, which takes place from 170 mT to 190 mT (5 mT step). From the pink trace, a Kondo energy  $k_B T_K$  of 50  $\mu\text{eV}$  is extracted with an Lorentzian fit.

towards  $B_c$  (bottom panel in Fig. 4.4a). In the low conductance regime, we thus measure a hard superconducting gap persisting up to  $B_c$  in Ge-Si NWs.

The closing of the superconducting gap in a higher conductance regime is presented in Fig. 4.4b. Since the transmission is increased, Andreev reflection processes cause a significant conductance within the superconducting gap [91]. Therefore, the conductance suppression in the gap becomes an ill-defined measure of the quasiparticle density of states and with that the quality of the induced superconductivity. However, here we can use the Kondo peak to examine the quasiparticle density of states in the superconducting gap. The Kondo peak is formed by coupling through quasiparticle states within the window of the Kondo energy ( $k_B T_K$ ). In the regime where  $k_B T_K \leq \Delta$ , the existence and size of the Kondo peak is then an indication of the quasiparticle density of states inside the superconducting gap [92, 93]. In our measurement  $\Delta$  is indeed larger than  $k_B T_K$  up to a magnetic field  $B = 170$  mT (see the blue and magenta line traces in bottom panel of Fig. 4.4b). Since in the measurement the Kondo peak only arises once the gap is fully closed, we have a low quasiparticle density of states within the superconducting gap. This supports our observation of a hard superconducting gap up to  $B_c$ . It also illustrates a new way of gauging whether the superconducting gap is hard in a high conductance regime.



## 4.7. CONCLUSION

Combining all three magnetic field regimes of Fig. 4.2-4.4, we observed Andreev levels showing a ground state transition, SOI from the coexistence of two bands in Ge-Si core-shell NWs, and a hard superconducting gap. The combination and correlation of these observations is a crucial step for exploring this material system as a candidate for creating an one-dimensional topological superconductor.

## 4.8. SUPPLEMENTARY MATERIAL

### 4.8.1. CALCULATION OF MULTIPLE ANDREEV REFLECTION AND THE FITTING PROCEDURE

The conductance and the current response of the voltage biased nanowire Josephson junction are calculated following the scattering approach introduced by Averin and Bardas in Ref. [83]. The model accounts for sequential Andreev reflections of electrons and holes accelerated by the voltage bias  $V_{sd}$  that propagate through the normal part of a SNS junction. The total DC current  $I_{th}(V_{sd})$  of a multimode junction is obtained [94] as a sum of the currents  $I_i$  carried by individual modes of the transverse quantization

$$I_{th}(V_{sd}) = \sum_i^N I_i(V_{sd}, T_i, \Delta), \quad (4.S1)$$

where  $T_i$  is the transmission probability of the  $i$ 'th mode and  $\Delta$  is the superconducting gap.

The transmission probabilities  $T_i$  and the superconducting gap  $\Delta$  of the measured nanowire junction are inferred by fitting the numerically obtained current to the experimental one through minimization of  $\chi = \int [I_{exp}(V_{sd}) - I_{th}(V_{sd})]^2 dV_{sd}$ .  $N$  is a free parameter of the fitting procedure. We have checked that increase of  $N$  above 2 results in the transmission probabilities  $T_{i>2} = 0$  evidencing the presence of only two conducting modes in the structure as described in the main text. The analogous procedure is performed for the differential conductance traces, obtained in the numerics by differentiation of the calculated current over the bias voltage.

### 4.8.2. NUMERICAL CALCULATIONS

#### DISCUSSION OF PREVIOUS RESULTS AND OVERVIEW

Our experimental data shows a g-factor with a gate-tunable anisotropy. A g-factor anisotropy for Ge-Si core-shell nanowires with a circular cross section and in the absence of electric fields was predicted for the lowest two subbands in Ref. 17: At  $k_z = 0$ , the g-factors for the lowest subband were computed to be  $g_z = 0.12$  and  $g_{x,y} = 5.78$ , for the second subband  $g_z = 3.12$  and  $g_{x,y} = 5.1$ . Comparing to the experimentally measured values, we observe that (i) the computed anisotropy in the lowest subband is larger than in the second subband, whereas we observe a quenched anisotropy for lower densities, and (ii) the experimentally measured  $g_z$  never drops below 2. A later numerical simulation including strain found for the lowest subband  $g_z = 1.8$  and  $g_{x,y} = 8.3$  [16], i.e. bringing the g-factor for field parallel to the wire closer to our experimental results. However, no results were given for the second subband there. Ref. 87 discussed the electric field



dependence of the g-factor anisotropy for the ground state in a quantum dot in the Ge-Si core-shell nanowire, and found that the anisotropy was quenched with increasing electric field due to the direct Rashba SOI. Again, this is opposite to our experimental observation that the anisotropy is quenched for small (absolute) gate voltages.

We can thus not directly interpret our results in terms of existing theory. For this reason we apply the model described in Ref. 16 to our experimental geometry and strain values. As we show below, strain can change g-factor values up to an order of magnitude and even reverse anisotropies. We also find that we need to consider excited quantum dot states to find agreement with the experimental data.

#### MODEL FOR NANOWIRE ALONG [110]

We use the Luttinger-Kohn Hamiltonian for holes that has been established for modeling Ge-Si core shell nanowires [16, 17]. Below we give this Hamiltonian in detail, the description was adapted from Ref. 16. The bulk Hamiltonian of the Ge core is

$$H = H_{\text{LK}} + H_Z + H_{\text{dir}} + H_{\text{R}} + H_{\text{BP}}, \quad (4.S2)$$

where  $H_{\text{LK}}$  is the Luttinger-Kohn (LK) Hamiltonian,  $H_{\text{dir}}$  the coupling to the electric field that is known to give rise to the direct Rashba spin-orbit interaction (SOI) [17],  $H_{\text{R}}$  is the indirect Rashba SOI due to coupling to other bands, and  $H_{\text{BP}}$  is the Bir-Pikus Hamiltonian describing the effects of strain. The magnetic field is included through the Zeeman term  $H_Z$ , and the orbital effect. We consider the orbital effect of the field through kinetic momentum substitution. We include a global “-” sign in our Hamiltonian such that hole states have a positive effective mass. In the following we take a detailed look at each term in the Hamiltonian separately.

**Luttinger-Kohn Hamiltonian** We use the Luttinger-Kohn (LK) Hamiltonian [95, 96]

$$H_{\text{LK}} = \frac{\hbar^2}{2m} \left[ \left( \gamma_1 + \frac{5}{2} \gamma_2 \right) k^2 - 2\gamma_2 \left( k_{x'}^2 J_{x'}^2 + k_{y'}^2 J_{y'}^2 + k_{z'}^2 J_{z'}^2 \right) - \gamma_3 \left( \{k_{x'}, k_{y'}\} \{J_{x'}, J_{y'}\} + \text{c.p.} \right) \right] \quad (4.S3)$$

where  $\gamma_{1,2,3}$  are the Luttinger parameters,  $m$  is the electron mass,  $J_i$  are the spin- $\frac{3}{2}$  matrices,  $k^2 = k_{x'}^2 + k_{y'}^2 + k_{z'}^2$ , “c.p.” stands for cyclic permutation, and  $\{A, B\} = AB + BA$  is the anticommutator.

For Ge,  $(\gamma_3 - \gamma_2)/\gamma_1 = 10.8\%$  and one can use the so called spherical approximation [16]. By setting  $\gamma_2 = \gamma_3 = \gamma_s$ , where  $\gamma_s = (2\gamma_2 + 3\gamma_3)/5$ , in Eq (4.S3) the Hamiltonian becomes spherically symmetric, and we may use a simulation coordinate system with  $z$  being the direction along the nanowire and the cross section laying in the  $xy$ -plane.

**Magnetic field** We include magnetic field through the Zeeman term [9, 96]

$$H_Z = 2\kappa \mu_B \mathbf{B} \cdot \mathbf{J} \quad (4.S4)$$

and the orbital effect by the following substitution in the Hamiltonian

$$\mathbf{k} \rightarrow \mathbf{k} + \frac{2\pi}{\phi_0} \mathbf{A}, \quad (4.S5)$$

where  $\mathbf{k} = (k_x, k_y, k_z) = -i\nabla$ ,  $\mathbf{A}$  the vector potential,  $\phi_0 = \frac{h}{e}$  is the flux quantum with  $e$  being positive elementary charge and  $h$  the Planck constant. The anisotropic Zeeman term  $2q\mu_B \mathbf{B} \cdot \mathcal{J}$  [9, 96], where  $\mathcal{J}_i = J_i^3$ , is omitted as  $|q| \ll |\kappa|$  for Si and Ge [16, 97].

**Electric field** We include the electric field by the direct coupling [16, 17] to the electrostatic potential

$$H_{\text{dir}} = -e\mathbf{E} \cdot \mathbf{r}, \quad (4.S6)$$

We also consider indirect coupling originating from higher bands, excluded from the LK Hamiltonian, in form of a standard Rashba SOI term [9]

$$H_{\text{R}} = \alpha\mathbf{E} \cdot \mathbf{k} \times \mathbf{J}, \quad (4.S7)$$

where  $\mathbf{E}$  is electric field and  $\alpha$  is the Rashba coefficient.

**Strain effect** In our numerical calculations we only simulate the Ge core, and include the presence of the Si shell through the strain that it induces in the core [17]. We model the strain using the Bir-Pikus Hamiltonian [19]

$$\begin{aligned} H_{\text{BP}} = & - \left( a + \frac{5b}{4} \right) \left( \epsilon_{x'x'} + \epsilon_{y'y'} + \epsilon_{z'z'} \right) \\ & + b \left( \epsilon_{x'x'} J_{x'}^2 + \epsilon_{y'y'} J_{y'}^2 + \epsilon_{z'z'} J_{z'}^2 \right) \\ & + \frac{d}{\sqrt{3}} \left( \epsilon_{x'y'} \{ J_{x'}, J_{y'} \} + \text{c.p.} \right), \end{aligned} \quad (4.S8)$$

where  $a, b, c$  are the deformation potentials and  $\epsilon_{ij} = \epsilon_{ji}$  are the strain tensor elements. Similarly to the Luttinger-Kohn Hamiltonian the spherical approximation can be used and strain may assumed to be constant in the Ge core [98]. Thus,  $d = \sqrt{3}b$ ,  $\epsilon_{\perp} = \epsilon_{xx} = \epsilon_{yy}$ , and  $\epsilon_{xy} = \epsilon_{xz} = \epsilon_{yz} = 0$ . The Bir-Pikus Hamiltonian then simplifies to the spherical symmetric form [98]

$$H_{\text{BP}} = b(\epsilon_{zz} - \epsilon_{\perp})J_z^2, \quad (4.S9)$$

where a global energy shift has been omitted.

**Material parameters** Material parameters used in the simulation are given in Table 4.S1. We take the structure parameters for Ge from Ref. 97, the effective Rashba coefficient from Ref. 16, the deformation potentials from Refs. 19 and 98, and the strain parameters of the sample from Ref. 50.

Table 4.S1: Band structure parameters for Ge [16, 97] and strain parameters [19, 50]. All parameters are for  $T = 0\text{K}$ .

$\gamma_1$	$\gamma_2$	$\gamma_3$	$\gamma_s$	$\kappa$	$\alpha$ [nm <sup>2</sup> e]	$b$ [eV]	$d$ [eV]	$\epsilon_{zz}$	$\epsilon_{rr}$
13.25	4.25	5.69	5.114	3.13	-0.4	-2.5	-5.0	-1.5	3.5

**Numerical method** We perform our numerical calculations using Kwant [99]. We use the finite difference method to discretize the Hamiltonian (4.S2) on a cubic grid with spacing  $a$ . Depending on the geometry we use two slightly different methods.

The first approach is suitable for simulating a translation invariant infinite wire system, by considering the Hamiltonian

$$H(k_x = -i\partial_x, k_y = -i\partial_y, k_z). \quad (4.S10)$$

The transverse momenta  $k_x$  and  $k_y$  are treated as differential operators, which are discretized as finite difference operators. The Hamiltonian is then represented in a tight-binding form, and a finite system in the  $xy$ -plane is generated that represents the wire cross section. The cross section has either a square or hexagon shape. The momentum along the wire,  $k_z$ , remains a scalar parameter.

In the second approach we treat all momenta as differential operators:

$$H(k_x = -i\partial_x, k_y = -i\partial_y, k_z = -i\partial_z). \quad (4.S11)$$

In addition to a finite cross section in the  $xy$ -plane we terminate the wire in the  $z$ -direction, effectively obtaining a quantum dot of length  $L$ .

The Landé  $g$ -factors are extracted from the energy spectrum of the system as a split in energies caused by the finite magnetic field

$$\Delta E_n = g_n \mu_B B, \quad (4.S12)$$

where  $n$  is band number,  $\mu_B$  is Bohr magneton, and  $B$  is the magnitude of the magnetic field. For the infinite wire we use the energy split at  $k_z = 0$ . We note that this numerical approach goes beyond the effective Hamiltonian approach in Ref. 17 and also takes into account the effects of higher states. The accuracy of our approach is controlled by the grid spacing  $a$ .

**Model geometry and verification** The nanowires used in our experiment have a hexagonal cross-section with a corner-to-corner width of 6 nm. Faithfully representing this shape with a cubic lattice requires a rather small lattice spacing  $a$  that is computationally unfavorable. Figure 4.S1 shows the comparison of the band structure between the

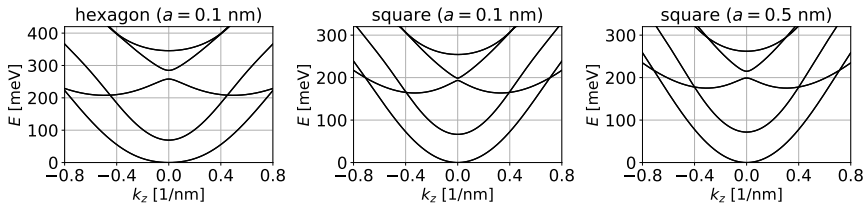


Figure 4.S1: **Band structure for different cross sections.** Dispersion of an infinite wire with hexagon (left) and square (middle, right) cross sections for different discretization grid spacings  $a = 0.1$  nm (left, middle) and  $a = 0.5$  nm (right).

wires with hexagon (left) and square (middle) shaped cross sections calculated using

the grid spacing  $a = 0.1$  nm. We observe that the impact of the cross section shape on the qualitative result is small, in agreement with what was reported for the comparison between a circular and square cross section [16]. Hence we use a square cross section with 6 nm side length in further calculations.

This choice allows us to use a larger grid spacing ( $a = 0.5$  nm) that significantly reduces the computational cost of the calculation. For grid spacing  $a = 0.5$  nm the square cross section preserves the symmetries of the system and key features of the dispersion of two lowest subbands, see middle and right panel on Fig. 4.S1. We also note that the band structures we observe agree qualitatively with what was reported earlier [16, 17], further verifying the accuracy of our approach.

**Simulation code and dataset** All simulation codes used in this project are available under (simplified) BSD licence together with raw simulation data [100].

## RESULTS

**Infinite wire** We first investigate the infinite wire system. In Fig. 4.S2 we present the anisotropy of the  $g$ -factors when a magnetic field is included only through the Zeeman term, only the orbital effect, and both of these contributions, respectively. The direction of magnetic field changes from along the  $+z$  axis (parallel to the wire) to the  $-z$  axis (antiparallel to the wire). No electric field is present in the system. The results show that the  $k_z = 0$  states behave differently in the lowest two subbands. In the lowest state the anisotropy originates almost exclusively from the Zeeman term. On the other hand, in the second state the Zeeman and orbital contributions both have significant anisotropies but opposite signs, such that they partially cancel (note that the graphs show absolute values of the  $g$ -factors). Comparing to Ref. 17 we find increased  $g$ -factor values, such as an order-of-magnitude enhancement of  $g_z$  in the lowest subband. We can attribute this to strain, as our numerical simulations yield  $g$ -factor values comparable to Ref. 17 in the absence of strain. Also, strain leads to  $g_z > g_{x,y}$  in the second subband, reversing the anisotropy. Note also that our results for the lowest subband agree better with the results of Ref. 16 with a somewhat weaker strain than in our situation.

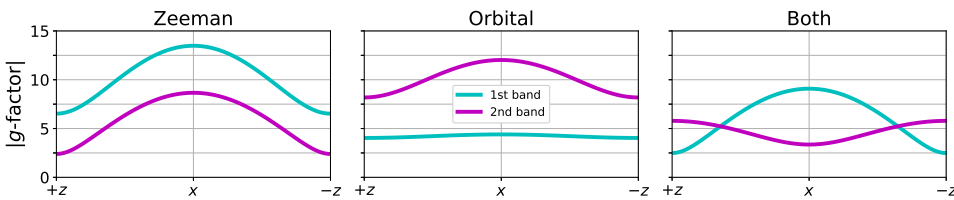


Figure 4.S2: **Anisotropy parallel and perpendicular to the NW.** Anisotropy of the  $g$ -factors of the two lowest states in an infinite wire with square cross section. The magnetic field is included through the Zeeman term only, the orbital contribution only, and through both on the left, middle, and right panel respectively. The direction of the magnetic field changes from parallel to antiparallel to the wire. No electric field is present in the system.

In Fig. 4.S3 we analyse the anisotropy as the magnetic field orientation changes with respect to the wire from the parallel to antiparallel direction (left and middle) and around

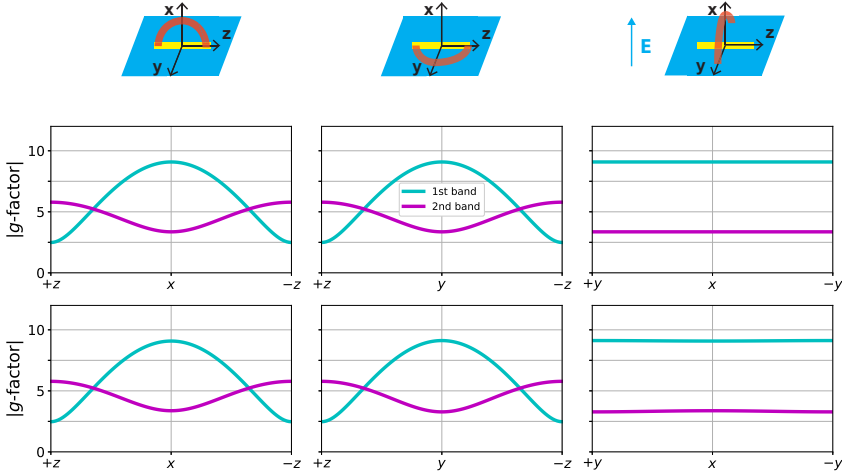


Figure 4.S3: **All anisotropies for the infinite wire model.** Anisotropy of the  $g$ -factors of the two lowest states in an infinite wire with square cross section. The upper panels correspond to zero electric field whereas on the lower panel a perpendicular electric field of  $10\text{V}/\mu\text{m}$  is applied.

the perpendicular directions (right), in the absence and presence of electric fields. The magnetic field is rotated from  $+z$  to  $-z$  axis through  $+x$  (left) and  $+y$  (middle). In the right panel magnetic field changes from  $+y$  through  $+x$  to  $-y$ . The upper row corresponds to systems with no electric field whereas the bottom row corresponds to systems with perpendicular electric field  $E_x = 10\text{V}/\mu\text{m}$  that we estimate for our experimental situation. Due to the fourfold rotational symmetry,  $g$ -factors are identical for  $x$  and  $y$  directions in the absence of electric field as expected. This symmetry is in principle broken by the applied field, but the anisotropy between  $x$  and  $y$  remains small for experimentally relevant field strengths. Indeed, we observe that due to the large confinement energy (around  $80\text{meV}$ , see Fig. 4.S3) the effect of the electric field on the  $k_z = 0$  states in the infinite wire is almost negligible, as demonstrated in Fig. 4.S4 (note that the shape of these wave functions in the absence of electric fields is in agreement with previous results [16, 17, 101]).

In summary, we find that the  $g$ -factor anisotropy of the lowest subbands is modified considerably by strain. However, the results also do not agree with our experimental finding of a quenched anisotropy at lower densities. For this reason, we now turn to quantum dots.

**Quantum dot** As explained in the main text, the experiment accesses higher states of the quantum dot, which originate from different subbands. In this section we show results for a quantum dot of length  $L = 170\text{ nm}$  (with hard-wall boundary conditions), corresponding to the experimental setup. The discretization grid has  $a = 0.5\text{ nm}$ .

Fig. 4.S5 shows the energy levels in the quantum dot as a function of  $\sqrt{\langle k_z^2 \rangle}$  evaluated in the given eigenstate. The states near the bottom of the lowest subband trace

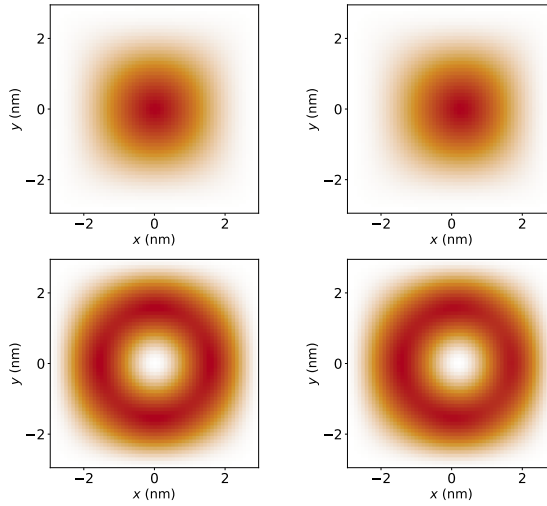


Figure 4.S4: **The wavefunction of the two lowest bands for  $k_z = 0$ .** On the left panel we show the calculations done without electric field whereas on the right panel we show calculation under the electric field  $10\text{V}/\mu\text{m}$ .

the infinite wire's dispersion very accurately, confirming the particle-in-box momentum quantization picture. When the second subband enters, the quantum dot levels significantly deviate from the infinite wire dispersion. This is a finite size effect, the result of mixing between states from different subbands with different  $\langle k_z^2 \rangle$  (note that in a finite wire  $k_z$  is not a conserved quantity). For most of the energy window with two subbands the two branches of the dispersion are clearly distinguishable, supporting the view that consecutive quantum dot states inherit properties from different subbands.

Fig. 4.S6a,b show the  $g$ -factors and  $g$ -factor anisotropies in the finite quantum dot respectively. At low energies, Fig. S9a reveals  $g_{x,y} > g_z$  in the absence of an electric field ( $E_x$ ) and  $g_y > g_x$  in the presence of  $E_x$ . This is in qualitative agreement with previous calculations for the ground states in Ge-Si NW quantum dots [87]. Also,  $g_y > g_x$  at finite  $E_x$  has recently been observed experimentally [88]. Where the second subband enters, the  $g$ -factor values split into two branches corresponding to the first and second subbands, this is especially visible in the  $g_z$  values. The external electric field induces a much larger anisotropy between  $g_x$  and  $g_y$  in higher states compared to the lowest one accessed at small  $k_z$ , that was discussed previously in Ref. 87. Since the effect of the electric field on the  $g$ -factor in the infinite wire case is small, we attribute the increased anisotropy to spin-momentum locking present at nonzero  $k_z$ .

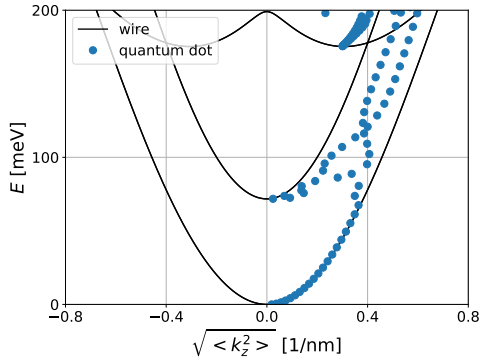


Figure 4.S5: **Quantum dot energy levels.** Quantum dot energies in function of  $\sqrt{\langle k_z^2 \rangle}$  overlaid with the dispersion of the infinite wire.

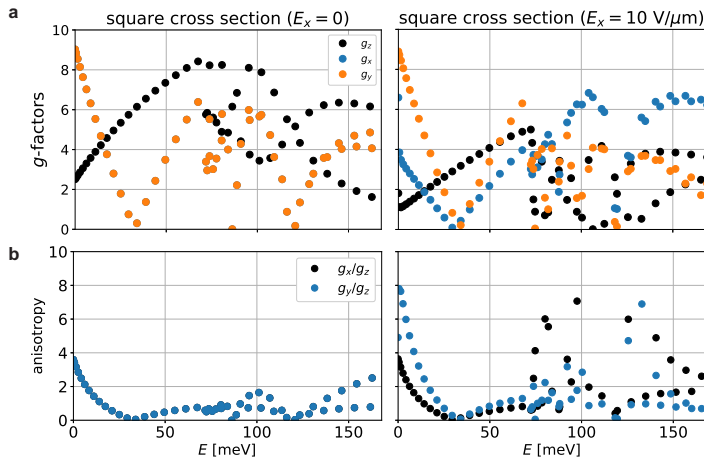


Figure 4.S6: **Anisotropies for quantum dot model.** **a**  $g$ -Factors in the quantum dot of length  $L = 170$  nm with a square cross section. Without applied electric field  $g_x$  and  $g_y$  are identical. **b**  $g$ -Factor anisotropy calculated from the values found in **a**.

## 4.8.3. SUPPLEMENTARY FIGURES

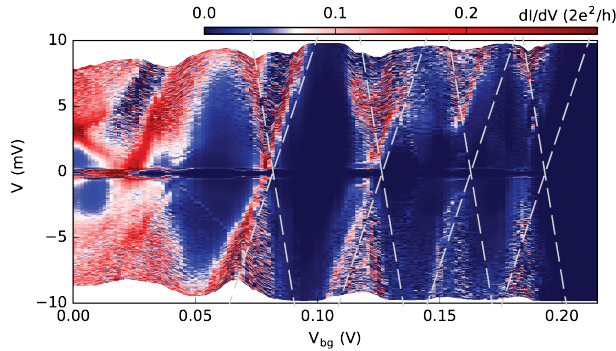


Figure 4.S7: **Coulomb diamonds.** Large  $V$  tunneling spectroscopy measurement of the superconducting quantum dot. The differential conductance ( $dI/dV$ ) as a function of  $V_{bg}$  reveals Coulomb diamonds that are highlighted by the dashed lines. From  $V_{bg} = 0.2$  V on the hole transport is pinched off. The charging energy of 12 meV, barriers' asymmetry of  $\Gamma_1/\Gamma_2 = 0.2-0.5$  and lever arm of 0.3 eV/V are estimated from this graph.

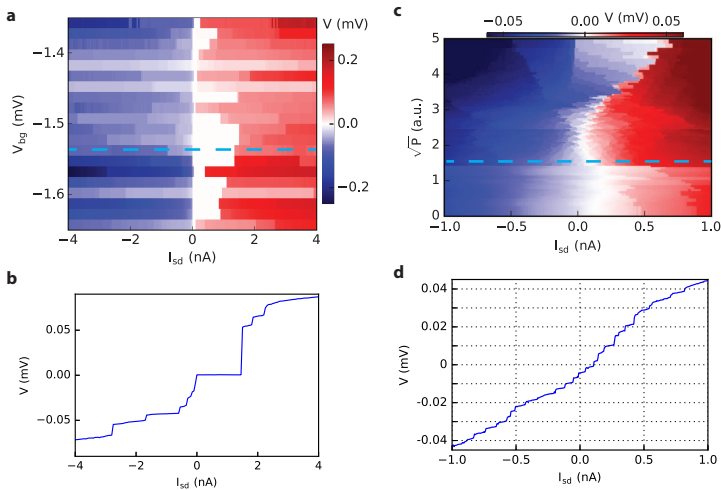


Figure 4.S8: **AC and DC Josephson effect.** **a** Voltage measurement as a function of current bias  $I_{sd}$  and  $V_{bg}$ . The measured voltage shows supercurrent as zero voltage plateaus. **b** Linetrace at  $V_{bg} = -1.3$  V. A switching current of 1.7 nA is observed. **c** Voltage measurement as a function of current bias at  $V_{bg} = -1.53$  V while a microwave excitation is applied with a varying power at a frequency  $f$  of 1.23 GHz. **d** A linetrace at  $\sqrt{P} = 1.46$  reveals Shapiro steps with stepsize corresponding to the frequency  $V = fh/2e = 2.5\mu V$ .



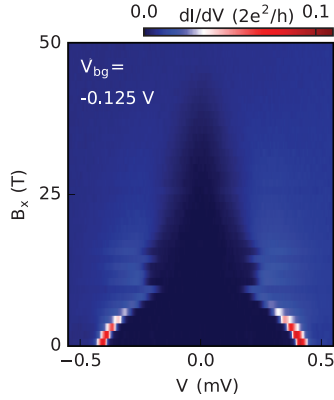


Figure 4.S9: **Superconducting gap closing as a function of  $B_x$ .** Tunneling spectroscopy measurement of the superconducting gap as a function of  $B_x$ , a magnetic field applied perpendicular to the substrate. The superconducting gap closes at a critical magnetic field of 45 mT. At 10 mT the gap closing seems to set in early. This dual gap closing is seen also in a similar experiment, where it is attributed to a superconducting material that is created during the annealing process and that is composed of Al and Si [58].

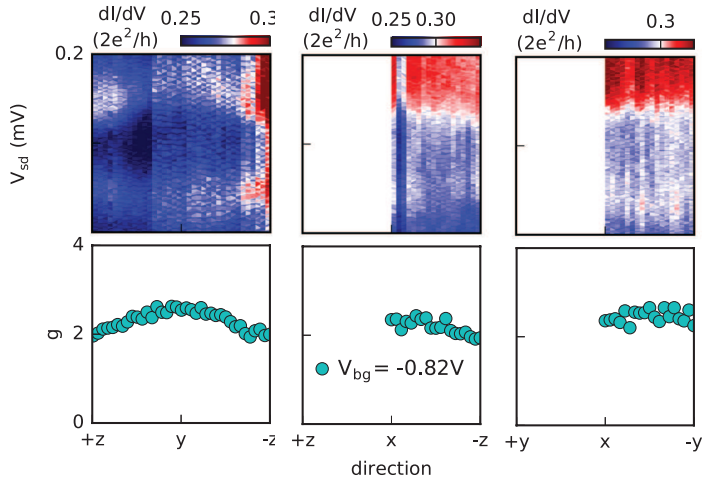


Figure 4.S10: **Measured anisotropy in a second device.** Rotations of the magnetic field with a 0.9 T magnitude in the  $yz$ -,  $xz$ - and  $xy$ -plane, respectively, at  $V_{bg} = -0.82$  V. The differential conductance data is plotted in the top row. The bottom row shows the extracted  $g$  of the center panel. The anisotropy in  $g$  has the same trend as Fig. 3 in the main text, although the amplitude is smaller.

# 5

## SPIN-ORBIT INTERACTION IN A DUAL GATED INAS/GASB QUANTUM WELL

*The spin-orbit interaction is investigated in a dual gated InAs/GaSb quantum well. Using an electric field, the quantum well can be tuned between a single-carrier regime with exclusively electrons as carriers and a two-carrier regime where electrons and holes co-exist. The spin-orbit interaction in both regimes manifests itself as a beating in the Shubnikov–de Haas oscillations. In the single-carrier regime the linear Dresselhaus strength is characterized by  $\beta = 28.5 \text{ meV}\text{\AA}$  and the Rashba coefficient  $\alpha$  is tuned from 75 to 53  $\text{meV}\text{\AA}$  by changing the electric field. In the two-carrier regime a quenching of the spin splitting is observed and attributed to a crossing of spin bands.*

---

This chapter has been published as, *Spin-orbit interaction in a dual gated InAs/GaSb quantum well*, A.J.A Beukman, F. K. de Vries, J. van Veen, R. Skolasinski, M. Wimmer, F. Qu, D. T. de Vries, B.-M. Nguyen, W. Yi, A. A. Kiselev, M. Sokolich, M. J. Manfra, F. Nichele, C. M. Marcus and L. P. Kouwenhoven, *Physical Review B* 96, 241401(R) (2017).

## 5.1. INTRODUCTION

The semiconductors InAs and GaSb have small band gaps together with a crystal inversion asymmetry resulting from their zinc-blende structure. These materials are therefore predicted to have strong spin-orbit interaction (SOI) [9, 102] which has been measured experimentally [103]. Moreover, tuning of the Rashba strength by electrostatic gating has been shown for InAs quantum wells [104, 105]. Strong and *in-situ* control over the SOI is a promising route towards novel spintronic devices [102, 106, 107], and a strong SOI together with a large  $g$ -factor and induced superconductivity are ingredients for a topological superconducting phase [76].

Combining InAs and GaSb in a quantum well gained much interest because of the type-II broken-gap band alignment [64]. As a result, the GaSb valence band maximum is higher in energy than the InAs conduction band minimum, opening a range of energies where electrons in the InAs coexist with holes in the GaSb. The spatial separation of these electron and hole gases allows for tunability of the band alignment using an electric field. Therefore, a rich phase diagram can be mapped out using dual gated devices [108, 109]. Although spatially separated, strong coupling between the materials allows for electron-hole hybridization which opens a gap in the energy spectrum when the density of electrons equals that of holes [110, 111], driving the band structure topologically nontrivial [108].

Interestingly, the magnitude of this hybridization gap is spin dependent due to the SOI [112–114]. Therefore, a spin-polarized state is seen at energies close to the hybridization gap [115], and at higher energies a dip in the spin splitting is expected [116]. The latter has yet to be observed and indicates a competition between electron-hole hybridization and the spin-orbit interaction. Here, we experimentally study SOI through the difference in density of the spin-orbit split bands of an InAs/GaSb quantum well. This zero-field density difference ( $\Delta n_{ZF}$ ) is extracted from magnetoresistance measurements. First, the SOI is investigated in the regime where the GaSb is depleted from carriers. Rashba and Dresselhaus SOI strengths can be extracted from measurements of  $\Delta n_{ZF}$ . Second, SOI is investigated just above the hybridization gap where  $\Delta n_{ZF}$  almost vanishes, consistent with band-structure calculations.

## 5.2. EXPERIMENTAL SETUP

A 20- $\mu\text{m}$ -wide and 80- $\mu\text{m}$ -long Hall bar device is defined using chemical wet etching techniques. A top gate is separated from the mesa by a 80-nm-thick  $\text{SiN}_x$  dielectric layer. The Hall bar is fabricated from the same wafer used in Refs. 68, 109. The quantum well consists of 12.5 nm InAs and 5 nm GaSb between 50 nm AlSb barriers. The doped GaSb substrate acts as a back gate. All measurements are done at 300 mK using standard lock-in techniques with an excitation current of 50 nA.

Figure 5.1 presents the longitudinal resistance of the Hall bar device as a function of top gate voltage  $V_{\text{tg}}$  and back gate voltage  $V_{\text{bg}}$ . The measurement is performed in a 2 T perpendicular magnetic field and therefore shows quantum oscillations resulting from the changing electron density. Quantum oscillations corresponding to holes are less pronounced as the mobility of holes in this system is much lower than the mobility of electrons [109]. For lines parallel to these oscillations, such as line I in Fig. 1(a), the

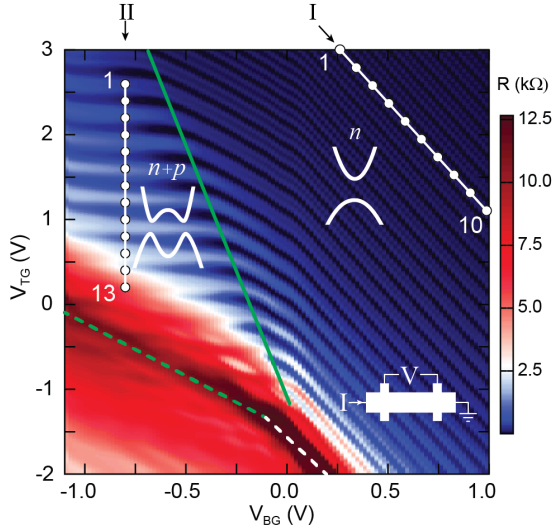


Figure 5.1: **Resistance map of the Hall bar device.** Longitudinal resistance of the Hall bar device (see bottom right inset) as a function of top gate voltage ( $V_{TG}$ ) and back gate voltage ( $V_{BG}$ ) at 2 T out-of-plane magnetic field. Oscillations in resistance originate from Landau levels and denote lines of constant electron density. The dashed green and white lines indicate regions with the Fermi level located inside an energy gap. The solid green line separates the region with electrons as carriers (right) from a region where electrons and holes coexist (left). Line I is situated in the electron regime and Line II in the two-carrier regime. The insets show the schematic band alignment for both cases.

electron density is constant while the electric field changes. Regions of high resistance, indicated by the dashed white and green lines, correspond to having the Fermi level inside an energy gap. A detailed description of the phase diagram obtained from measurements on the same wafer was reported by Qu et al. [109].

The green solid line in Fig. 5.1 divides the phase diagram into two regimes. To the right-hand side of this line is the electron-only regime, where the GaSb is depleted. The system effectively is an asymmetric InAs quantum well with a trivial band alignment and a Fermi level residing in the conduction band (see the inset of Fig. 5.1). In this regime we investigate  $\Delta n_{ZF}$  along line I, where the electron mobility is highest while only the lowest subband remains occupied. The regime to the left of the green line is the two-carrier regime where electrons and holes coexist. Line II is chosen to evaluate  $\Delta n_{ZF}$  close to the hybridization gap (highlighted by the dashed green line). Before discussing the spin-orbit interaction in the two-carrier regime (along line II) we first study the electron-only regime (line I).

### 5.3. ELECTRON REGIME

Figure 5.2a shows magnetoresistance traces for 10 points along line I. The density of electrons is fixed (see Fig. 5.2c) while the electric field is changed. We first consider trace 1. Clear oscillations in the longitudinal resistance  $R_{xx}$  are observed as a function

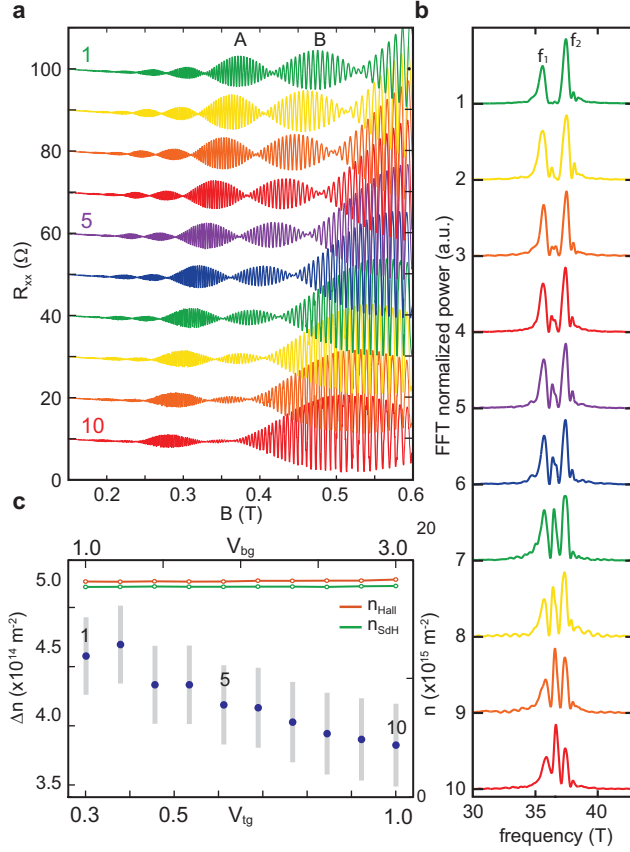


Figure 5.2: **Spin splitting at a constant electron density in the electron regime.** **a** Magnetoresistance traces for data points 1-10 along line I indicated in Fig. 5.1, a constant background is subtracted from the traces and they are offset 10 Ω from each other. **b** Fourier power spectra  $|\mathcal{F}[R_{xx}(1/B)]|^2$  of the traces in **a**. **c** Electron density extracted from Hall resistance and Shubnikov-de Haas period (right axis) together with the  $\Delta n_{ZF}$  at each data point along line I (left axis), with error bars in gray.

of perpendicular magnetic field  $B$  modulated by a beat pattern. These Shubnikov-de Haas (SdH) oscillations appear for each single spin band and are periodic in  $1/B$  with a frequency that relates to the carrier density via  $n = e/h \cdot f$  [103, 117]. The beat modulation observed in trace 1 is caused by two slightly different SdH frequencies  $f_1, f_2$ . This is also evident from the fast Fourier transform (FFT) of the magnetoresistance trace  $\mathcal{F}[R_{xx}(1/B)]$  presented in the first curve of Fig. 5.2b (see Supplementary Material for details on the Fourier procedure Sec. 5.7). These two SdH frequencies indicate two distinct densities  $n_1, n_2$ . They must correspond to different spin species because their sum  $n_1 + n_2$  equals the Hall density  $n_H$  (see Fig. 5.2c). Subsequently, one spin species has a larger density than the other,  $n_1 > n_2$ , implying that the system favors one spin-orbit eigenstate over to the other. The difference,  $\Delta n_{ZF} = n_2 - n_1$ , is a measure for the zero-field spin splitting energy,  $\Delta E_{ZFSS} = \Delta n_{ZF} (m^* / \pi \hbar^2)^{-1}$ .

Upon moving from point 1 to 10 along line I, two trends are observed. First, an extra frequency peak emerges in the FFTs at  $(f_1 + f_2)/2$ . This originates from the asymmetry between adjacent beats in the SdH oscillations, visible both in amplitude and number of oscillations of beats A and B in Fig. 5.2a and Fig. 5.S1. Second, the spacing between the outer peaks in the FFT spectrum decreases, as is evident from the decreasing  $\Delta n_{ZF}$  over line I (Fig. 5.2c). This arises from an increasing number of oscillations in both beats A and B (Fig. 5.S1), which also pushes the beat nodes to lower magnetic fields. Before we extract the actual SOI strengths and show its electric field dependence, we first elucidate the origin of the emerging center frequency peak.

The center frequency, interestingly, does not correspond to an actual density. The sum of the densities  $n_1$  and  $n_2$  (corresponding to the outer peaks in the FFT) still equals the Hall density. There are, however, mechanisms involving scattering between Fermi surfaces that can result in extra frequency components. Such mechanisms are magnetic inter subband scattering (MIS) [118, 119], magnetophonon resonances (MPR) [120, 121] and magnetic breakdown (MB) [122–124].

We exclude MIS and MPR. By changing electron density all the frequency peak positions shift with equal strength (Fig. 5.S2). However, the oscillation frequency of MIS and MPR is determined by the subband spacing and a specific phonon frequency, respectively. Both do not depend on the electron density. In contrast, for MB the spurious peak always appears in between  $f_1$  and  $f_2$ . The MB mechanism explains this spurious central peak as carriers tunneling between spin-polarized Fermi surfaces at spin-degeneracy points. The interplay of Dresselhaus and Rashba SOIs in our heterostructure could lead to such an anisotropic Fermi surface [122, 125]. In order to confirm this hypothesis, we extract the individual Rashba and Dresselhaus contributions by comparing our data to quantum mechanical Landau level simulations that include the MB mechanism.

## 5.4. LANDAU LEVEL SIMULATIONS

The quantum well in this electron-only regime is modeled by a Hamiltonian with spin-orbit interaction in two-dimensional (2D) electron systems subject to a perpendicular magnetic field  $B$ , as given by [9, 102]:

$$H = \frac{(\hat{p}_x^2 + \hat{p}_y^2)}{2m^*} \sigma_0 + \alpha(\hat{p}_y \sigma_x - \hat{p}_x \sigma_y) / \hbar + \beta(\hat{p}_x \sigma_x - \hat{p}_y \sigma_y) / \hbar + \gamma(\hat{p}_y \hat{p}_x \hat{p}_y \sigma_x - \hat{p}_x \hat{p}_y \hat{p}_x \sigma_y) / \hbar^3 + \frac{1}{2} g \mu_B B \sigma_z \quad (5.1)$$

Where  $p_i \rightarrow p_i + eA_i$  is the canonical momentum,  $\sigma_i$  Pauli spin matrices,  $\alpha, \beta, \gamma$  the Rashba, linear Dresselhaus and cubic Dresselhaus coefficients, respectively,  $\hbar$  the reduced Planck's constant,  $\mu_B$  the Bohr magneton. An electron effective mass  $m^*$  of  $0.04m_0$  is measured from the temperature dependence of the SdH oscillations (Fig. 5.S3) and a  $g$ -factor of  $-11.5$  is used in the calculations<sup>1</sup> [66]. We solve for the Landau level energies in a perpendicular magnetic field  $B_z$  and extract the resistivity as a function of magnetic field (see Supplementary Material for details see Sec. 5.7).

<sup>1</sup>Note that this  $g$ -factor value of  $-11.5$  is measured on a slightly different stack with an InAs layer of 11.0 nm thick. We have checked in the simulations that changing the  $g$ -factor to  $-5$  or  $-15$  has negligible influence on the SdH oscillations.

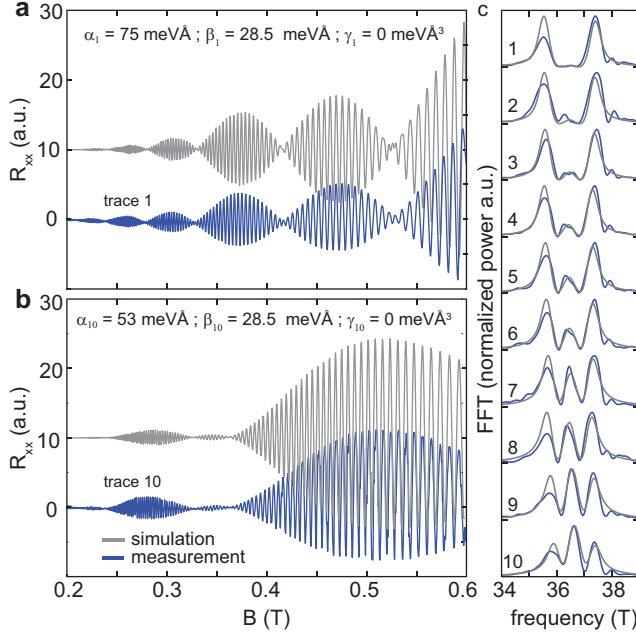


Figure 5.3: **Landau level simulations for a 2DEG with Rashba and Dresselhaus spin-orbit interactions.** **a** and **b** depict the measured trace (blue) together with the simulated magnetoresistance trace (gray) which is offset by ten units. The values for  $\alpha$ ,  $\beta$ , and  $\gamma$  used are mentioned in the figure. In all the simulations the Landau level broadening is set to  $\Gamma = 0.45$  meV. **c** Fast Fourier transform of the simulated and measured magnetoresistance at points 1-10 along line I. All simulated magnetoresistance traces can be found in the Supplementary Material Fig. 5.S4.

The parameters  $\alpha$ ,  $\beta$ ,  $\gamma$  in the model are estimated and fine tuned to match the node positions and the number of oscillations in a beat of the measured SdH traces. Figures 5.3a and 5.3b show the measured SdH data together with the simulated data for traces 1 and 10. Trace 1 is fitted with  $\alpha_1 = 75$  meVÅ,  $\beta_1 = 28.5$  meVÅ,  $\gamma_1 = 0$  meVÅ<sup>3</sup> and trace 10 is fitted with  $\alpha_{10} = 53$  meVÅ,  $\beta_{10} = 28.5$  meVÅ,  $\gamma_{10} = 0$  meVÅ<sup>3</sup>. The node positions and amplitude modulation of the simulated data agrees well with the measured SdH oscillations.

Curiously, only good fits are obtained when setting the cubic Dresselhaus term  $\gamma$  to zero. In 2D systems,  $\beta$  is related to  $\gamma$  via  $\beta = \langle k_z^2 \rangle \gamma$ , where  $\langle k_z^2 \rangle \approx (\pi/d)^2$  is the expectation value of the transverse momentum [9, 102] in a quantum well of thickness  $d$ . So  $\gamma$  should be non-zero. Currently we do not understand this discrepancy. A recent experimental study on a similar material system also found that the cubic Dresselhaus term could be neglected [126].

Now we consider all traces (1-10) and show that the two trends of Fig. 5.2 (emerging center FFT peak and approaching outer FFT peaks) are reproduced by changing only the Rashba SOI strength. Figure 5.3c shows the FFTs of the simulated traces where  $\alpha$  is linearly interpolated between  $\alpha_1$  and  $\alpha_{10}$  while fixing  $\beta = 28.5$  meVÅ and  $\gamma = 0$  meVÅ<sup>3</sup>. Linear interpolation is used because the electric field changes linearly along line I, and

Rashba SOI strength depends linearly on electric field [9, 127, 128]. All simulated FFTs and the SdH traces (Fig. 5.S4) match the measured data very well, clearly reproducing the emerging central peak and the approaching outer peaks.

## 5.5. TWO-CARRIER REGIME

In the remainder of this chapter we switch to the two-carrier regime, located left of the solid green line in Fig. 5.1. Electrons in InAs are present alongside with holes in GaSb ( $n + p$ ). Here, we study the influence of the hybridization of electrons with holes on  $\Delta n_{ZF}$  by investigating magnetoresistance traces on the points 1-13 along line II.

Before continuing with the measured magnetoresistance traces, it is insightful to examine the expected band structures at points 1 and 13, as illustrated in Fig. 5.4b. The first point of line II is located near the boundary between the two-carrier and single carrier regimes. A small amount of holes with a large amount of electrons is present. At point 13, close to the hybridization gap, the electron and hole densities are roughly equal, hence the Fermi level  $E_f$  is close to the hybridization gap. Note also that  $k_{\text{cross}}$  decreases from 1 to 13, since the electric field changes.

Figure 5.4a shows the magnetoresistance traces 1-13 along line II. Starting from trace 1 towards trace 13 we find series of traces with or without beating, depicted in blue and red, respectively. For traces 1-3, at large electron density, beating is observed from which we extract  $\Delta n_{ZF} = 1.7 \cdot 10^{14} \text{ m}^{-2}$ <sup>2</sup>. Remarkably, traces 4 and 5 do not show any beating, therefore no zero-field density difference can be extracted. For traces 6-10, the beating revives, showing strong beating. Finally, traces 11-13 show no beating. Figure 5.4c depicts the extracted  $\Delta n_{ZF}$  along line II, which shows a nonmonotonic behavior as a function of gate voltage along line II.

In order to understand this nonmonotonic  $\Delta n_{ZF}$  near the hybridization gap (points 1-10) we performed band structure calculations of our InAs/GaSb quantum well. The  $\Delta n$  extracted from these calculations is plotted in Fig. 5.4d, which qualitatively agree with the observed dip in  $\Delta n_{ZF}$  at points 4 and 5 (Fig. 5.4c). In order to understand the simulated  $\Delta n$ , the band structure near the hybridization gap is depicted in the inset of Fig. 5.4d (the zoom-in on Fig. 5.4b indicated by the red box). The blue and red lines represent different spin bands. The bands cross at the black arrow, indicating the vanishing of  $\Delta n$ , such as observed in the experiment. We found this feature to be robust for different electric fields and crystal directions, see Fig. 5.S6. Interestingly, the crossing of spin bands implies a sign change in SOI strength. Opposite signs of SOI can thus be reached by adjusting the chemical potential. Usually, electric fields are applied to reach such a sign change [129].

Note that only a qualitative comparison between experiment and calculations is possible as only the Fermi energy is varied in the simulation, while in the experiment the band structure ( $k_{\text{cross}}$ ) and Fermi energy are expected to change. The fact that  $\Delta n_{ZF}$  in Fig. 5.4d does not completely vanish is because the crossing of the spin bands in the [110] occurs at a slightly different energy than in the [100] direction.

The lack of beating of traces 11-13 is not captured with the simulation. There are

<sup>2</sup>We cannot directly extract the spin-orbit strength from this  $\Delta n$  by comparing to the single-carrier case, since the effective mass in this region is unknown.



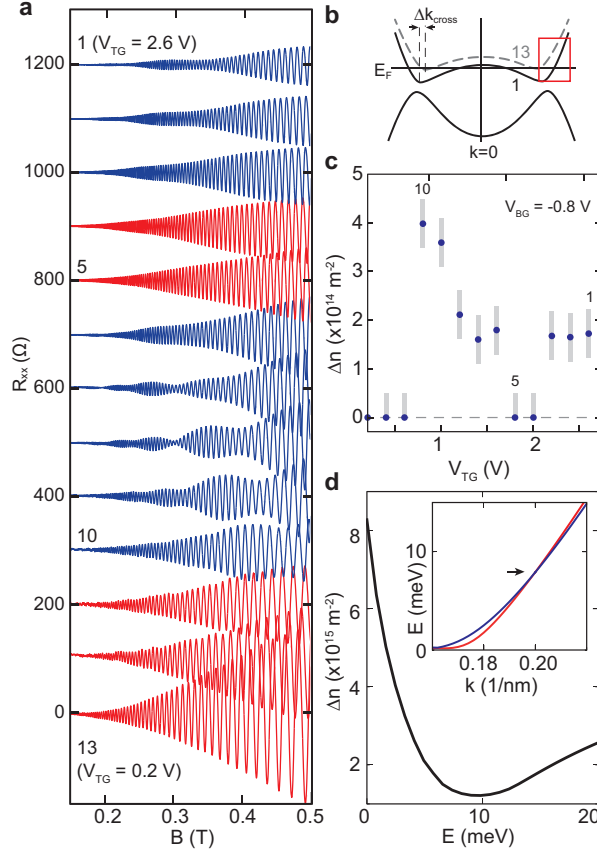


Figure 5.4: **Spin-splitting in the two-carrier regime.** **a** Magnetoresistance traces for points 1 to 13 along line II indicated in Fig. 1. For each trace the  $R_{xx}(B=0)$  background resistance is subtracted and afterwards the traces are offset by  $100 \Omega$ . Beating is (not) observed for (red) (blue) colored traces. **b** Schematic band structure tuning when moving from point 1 to 13. **c**  $\Delta n_{ZF}$  extracted from the Fourier transform of magnetoresistance traces (see Fig. 5.S5) of **a**. Error bars are indicated by the light blue bar. **d**  $\Delta n_{ZF}$  extracted from band structure calculation for our InAs/GaSb quantum well at zero electric field. The inset shows the corresponding band structure in the [100] direction.

two possible reasons for this deviation. First, a strong asymmetry in SdH amplitudes of the two spin species ( $A_{\text{up}} \gg A_{\text{down}}$ ) determines the visibility of the beating pattern. The single spin band SdH oscillation amplitude depends on effective mass  $m^*$  and scattering time according to  $A_{\text{SdH}} \sim (eB/m^*)^3 \exp(-\pi/\omega_c\tau)$  [130]. Both the effective mass and scattering time for the two spin bands become very dissimilar when approaching the hybridization gap (Fig. 5.S7), as a result that the beating visibility is reduced to below the experimentally detectable visibility. Second, Nichele et al. [115] shows there is an energy window with only one single spin band present. In such a spin-polarized state no beating can occur. Here, we cannot discriminate between these two reasons that explain the lack of beating in traces 11-13.

## 5.6. CONCLUSION

In conclusion, we presented a study of the spin-orbit interaction in an InAs/GaSb double quantum well. The Fermi level and band structure are altered by top and bottom gates. In the electron-only regime we find a electric field tunable spin-orbit interaction, and extract the individual Rashba and Dresselhaus terms. In the two-carrier regime we observe a nonmonotonic behavior of the spin splitting which we trace back to the crossing of the spin bands due to the hybridization of electrons and holes.

## 5.7. SUPPLEMENTARY MATERIAL

### 5.7.1. FOURIER TRANSFORMS

The Fourier transforms in this manuscript are obtained using the method described here. Starting from a magnetoresistance curve, first a magnetic field range is chosen. The lower bound is fixed at 0.15 T. The upper bound is chosen such that the interval ends at 40% of a beat maximum. Truncating the signal in this way causes minimal deviation from the true frequency components. Next, the background resistance is estimated using a 6<sup>th</sup> order polynomial fit, which subsequently is subtracted from the signal. The remaining signal is interpolated on a uniform grid in  $1/B$  and padded with zeros on both sides. No extra window function is applied. A fast Fourier transform converts the signal to the frequency domain  $R(\omega)$  and the power spectrum is obtained using  $P(\omega) = R(\omega) \times R^*(\omega)$ . All Fourier transforms are normalized such that the maximum is 0.8 a.u.

### 5.7.2. DETAILS ON THE LANDAU LEVEL SIMULATION

This section describes the calculations used to simulate the magnetoresistance traces to extract the Rashba and Dresselhaus coefficients as shown in Fig. 3a of the main text. We closely follow the method presented in Ref. 130 and Ch. 4 of Ref. 9.

The Hamiltonian in the momentum basis is presented in Eq. 1 of the main text, here repeated for convenience:

$$H = \frac{(\hat{p}_x^2 + \hat{p}_y^2)}{2m^*} \sigma_0 + \alpha(\hat{p}_y \sigma_x - \hat{p}_x \sigma_y) / \hbar + \beta(\hat{p}_x \sigma_x - \hat{p}_y \sigma_y) / \hbar + \gamma(\hat{p}_y \hat{p}_x \hat{p}_y \sigma_x - \hat{p}_x \hat{p}_y \hat{p}_x \sigma_y) / \hbar^3 + \frac{1}{2} g \mu_B B_z \sigma_z \quad (5.S1)$$

For the perpendicular magnetic field  $B = (0, 0, B_z)$ , the symmetric gauge  $\mathbf{A}(x, y) = \frac{B_z}{2}(-y, x, 0)$  is used. The canonical momentum can be written as

$$\hat{p} = -i\hbar\nabla + e\mathbf{A}. \quad (5.S2)$$

Raising and lowering operators are defined as

$$\begin{aligned} a^\dagger &= \frac{\lambda_c}{\sqrt{2}\hbar} (\hat{p}_x + i\hat{p}_y), \\ a &= \frac{\lambda_c}{\sqrt{2}\hbar} (\hat{p}_x - i\hat{p}_y), \end{aligned} \quad (5.S3)$$

where  $\lambda_c = \sqrt{\hbar/eB}$  is the magnetic length. The raising operators act on the Landau levels, i.e.  $a^\dagger|n, \uparrow\rangle = \sqrt{n+1}|n+1, \uparrow\rangle$ . The momentum operators are rewritten in the raising and lowering operators, which are then substituted into the Hamiltonian. We take a basis of  $N = 400$  Landau levels in order to capture magnetic fields  $\gtrsim 0.1$  T for the electron density  $n_s \approx 17.6 \cdot 10^{15} \text{ m}^{-2}$ . Solving the Hamiltonian results in the Landau level energies at a particular magnetic field  $E(n, B_z)$ .

Following Luo et al. [130] the conductance is written as:

$$\sigma_{xx} = \frac{e^2}{\pi^2 \hbar} \sum_{n, \uparrow \downarrow} \left( n \pm \frac{1}{2} \right) \exp \left( -\frac{(E_f - E_{n, \uparrow \downarrow})^2}{\Gamma^2} \right). \quad (5.S4)$$

We assume a fixed Fermi energy at  $E_f = (\pi \hbar^2 n_s) / m^*$ . To obtain the resistivity we use the approximation that for quantizing magnetic fields ( $\sigma_{xy}^2 \gg \sigma_{xx}^2$ ) the transverse resistivity  $\rho_{xx}$  is given as [130]:

$$\rho_{xx} = \sigma_{xx} / (\sigma_{xy}^2 + \sigma_{xx}^2) \approx \sigma_{xx} / \sigma_{xy}^2 \approx \sigma_{xx} (B_z / e n_s)^2 \quad (5.S5)$$

5

### 5.7.3. SUPPLEMENTARY FIGURES

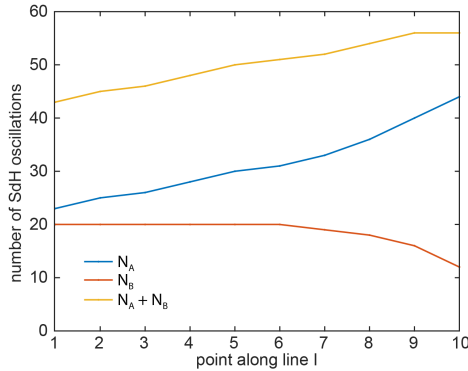


Figure 5.S1: **Number of oscillations in a beat.** Number of SdH oscillations in beat A ( $N_A$ ), beat B ( $N_B$ ) and the sum ( $N_A + N_B$ ) for each trace in Fig. 2a of the main text. The two trends discussed in the main text are clearly visible here. First, moving from point 1 to 10 the asymmetry  $r = (N_A - N_B) / (N_A + N_B)$  increases. Second, the total number of oscillations  $N_A + N_B$  increases.

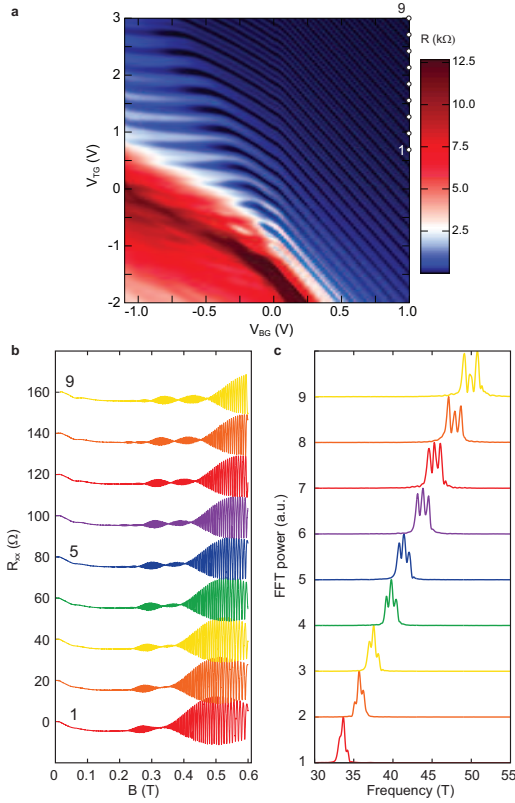


Figure 5.S2: **Peaks shift upon changing electron density.** **a** Phase diagram of the InAs/GaSb quantum well at  $B_{\perp} = 2$  T showing 9 additional points investigated. Moving from point 1 to 9 several SdH oscillations are crossed, hence the electron density increases from point 1 to 9. **b** Magnetoresistance traces  $R_{xx}(B)$  for points 1 to 9. Traces are offset by 20  $\Omega$ . **c** Fourier transforms of the traces in **b**, showing that the center frequency shifts together with the outer frequency peaks. This density dependence of the central frequency peak excludes MIS and MAR.

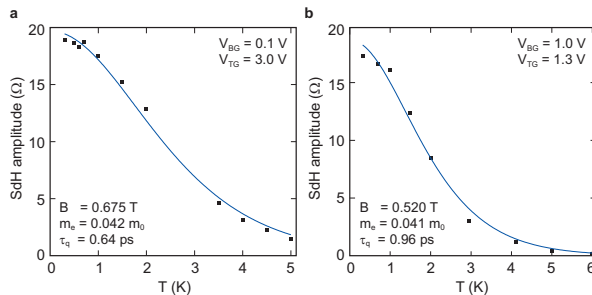


Figure 5.S3: **Dingle plot of the effective mass.** **a, b** Temperature dependence of the SdH oscillations (Dingle plots) measured at point 1 and 10 on line I, respectively. Effective mass  $m^*$ , indicated in the figures, is extracted by fitting these data to the Dingle formula (blue curve).

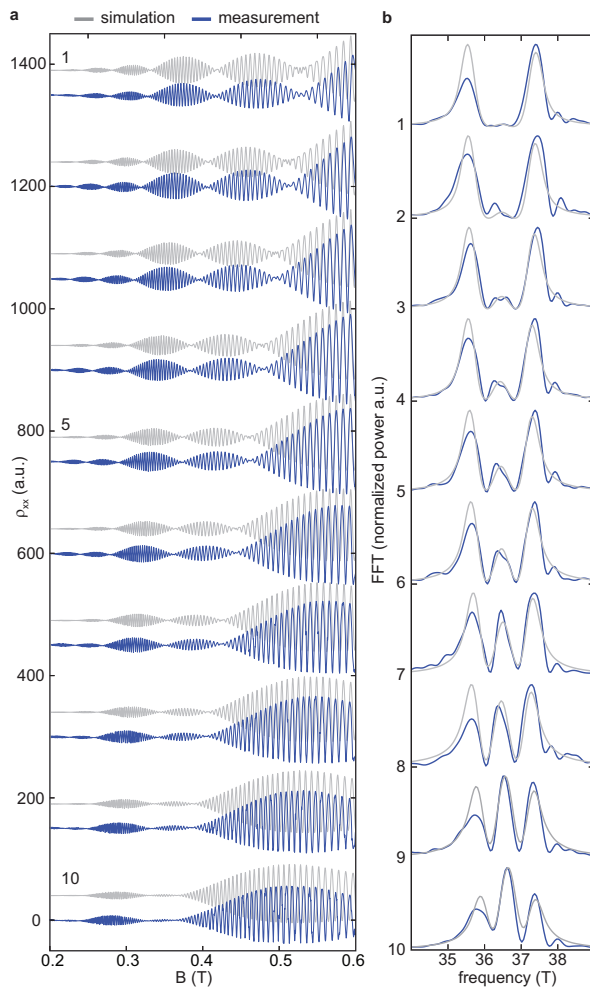


Figure 5.S4: **SdH traces of the Landau level simulations.** **a** Measured magnetoresistance traces (blue) for points 1-10 along line I together with the simulated traces (gray). The simulated traces are offset 40 a.u. from the measured traces; the measured traces are offset by 150 a.u. from each other. The value of Rashba spin-orbit interaction strength  $\alpha$  is linearly changed from 73 to 53 meVÅ going from trace 1 to 10. The linear and cubic Dresselhaus interaction strength are kept constant at  $\beta = 28.5$  meVÅ and  $\gamma = 0$  meVÅ<sup>3</sup>. **b** Corresponding Fourier transforms of the measured traces (blue) and simulated traces (gray), i.e. a reproduction of Fig 5.3c.

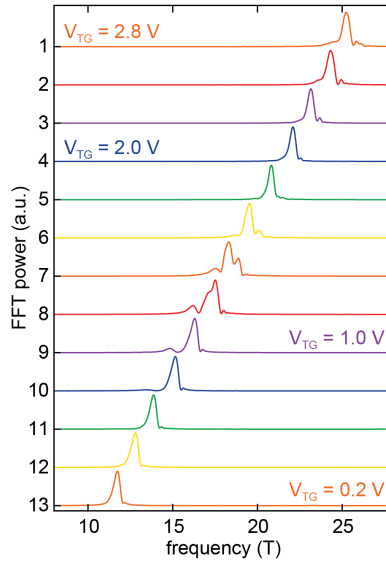


Figure 5.S5: **Fourier transforms for the 13 points along line II in the two-carrier regime.** All traces are normalized such that the maximum is set to 0.8 a.u.

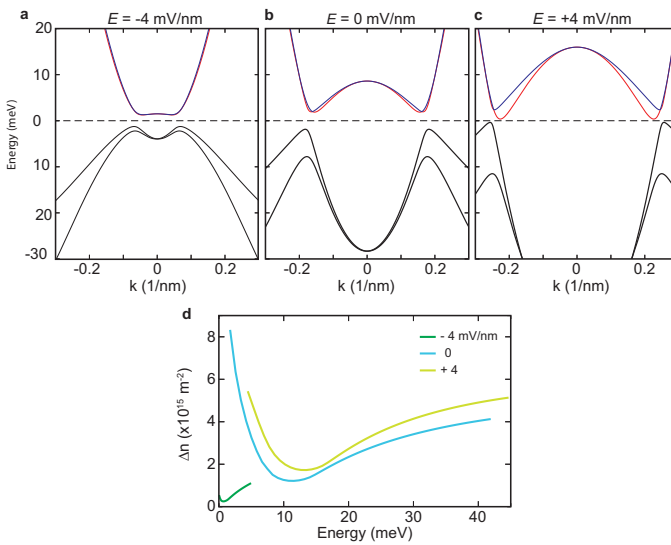


Figure 5.S6: **Band structure calculations for multiple electric fields/ a-c** Result of band structure calculations along [100] for electric fields  $\vec{E} = -4$  mV/nm, 0 mV/nm and +4 mV/nm, respectively. The spin-split bands of the conduction band are colored red and blue for clarity. **d** The ZFSS extracted from these band structures. For all electric fields a minimum in spin-splitting is found, making this a robust feature of an inverted band structure.

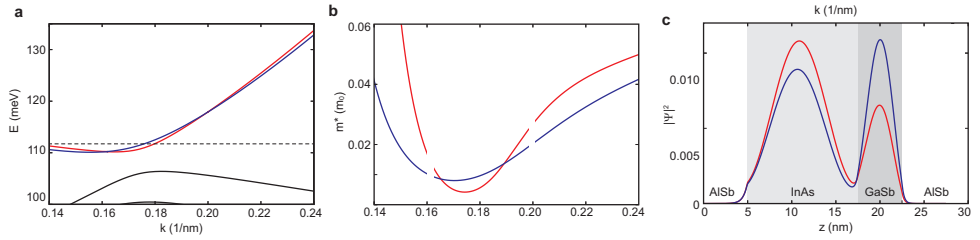


Figure 5.S7: **Effective mass & wave function in the quantum well** **a** Zoom-in on the calculated band structure (at  $\vec{E} = 0$ ) close to the hybridization gap. Red and blue correspond to different spin species. **b** Effective mass calculated from  $m^* = \hbar^2 (\partial^2 E / \partial k^2)^{-1}$ . The effective mass around  $k = 0.16$  nm $^{-1}$  and  $k = 0.20$  nm $^{-1}$  is omitted due to numerical artifacts. **c** Simulated normalized wave functions at the energy indicated by the dashed line in **a**. It is clear that the distribution of the wave function is spin dependent, which could result in a spin dependent scattering.

# 6

## $h/e$ SUPERCONDUCTING QUANTUM INTERFERENCE THROUGH TRIVIAL EDGE STATES IN INAs

*Josephson junctions defined in strong spin-orbit semiconductors are highly interesting for the search for topological systems. However, next to topological edge states that emerge in a sufficient magnetic field, trivial edge states can also occur. We study the trivial edge states with superconducting quantum interference measurements on nontopological InAs Josephson junctions. We observe a SQUID pattern, an indication of superconducting edge transport. Also, a remarkable  $h/e$  SQUID signal is observed that, as we find, stems from crossed Andreev states.*

---

This chapter, except for parts of Sec. 6.1.1, has been published as,  *$h/e$  Superconducting Quantum Interference through Trivial Edges States in InAs*, Folkert K. de Vries, Tom Timmerman, Viacheslav P. Ostroukh, Jasper van Veen, Arjan J. A. Beukman, Fanming Qu, Michael Wimmer, Bin-Minh Nguyen, Andrey A. Kiselev, Wei Yi, Marko Sokolich, Michael J. Manfra, Charles M. Marcus and Leo P. Kouwenhoven, in *Physical Review Letters* 120, 047702 (2018).



## 6.1. INTRODUCTION

Topological systems are a hot topic in condensed matter physics [131]. This is largely motivated by the existence of states at the interface between two topologically distinct phases, for example helical edge states in a quantum spin Hall insulator (QSHI) [132, 133]. Inducing superconductivity in these edge states would form a topological superconductor [131]. Superconducting edge transport has already been found in materials that are predicted to be QSHI [134, 135]. However, edge states can also have a non-topological origin. Trivial edge conduction is found in InAs alongside the chiral edge states in the QH regime [136] and recently in the proposed QSHI InAs/GaSb as well [137, 138]. To be able to discriminate between topological and trivial states it is crucial to study transport through trivial edges also and clarify differences and similarities between them. In this work we study the superconducting transport through trivial edge states in nontopological InAs Josephson junctions using superconducting quantum interference (SQI) measurements. We find supercurrent carried by these edge states and an intriguing  $h/e$  periodic signal in a superconducting quantum interference device (SQUID) geometry.

### 6.1.1. TRIVIAL EDGE STATES

Trivial edge states arise when the Fermi level resides in the band gap in the bulk, while being pinned in the conduction band at the surface. Then, band bending leads to electron accumulation at that surface as schematically drawn in Fig. 6.3a. The Fermi level pinning can have several origins: truncating the Bloch functions in space [139, 140], a work function difference [3], the built-in electric field in a heterostack [141] and the surface termination [142]. In our 2D InAs Josephson junctions the accumulation surface is located at the edge of the mesa that is defined by wet etching.

Experimental evidence of trivial edge conduction at these surfaces is reported by us before [137, 138]. Since we use a very similar heterostructure here, we revisit and discuss those results. We consider the electron regime of an InAs/GaSb double quantum well only, where the InAs is populated with electrons and the GaSb is gapped. Two measurement geometries are used, a Hall bar and a corbino disc (insets Fig. 6.2a-b), both have a top and bottom gate. In the first, all contacts are connected via both the bulk and the edge of the material, where for the latter the contacts are solely connected by the bulk. Details on the device fabrication and the measurements can be found in Ref. 138.

Local measurements, probing both the bulk and edge, and non-local measurements, probing the edge only, are performed on the Hall bar device of  $100\ \mu\text{m}$  long and  $20\ \mu\text{m}$  wide (Fig. 6.1a-b). For the local measurement (Fig. 6.1c) the resistance map as a function of top and bottom gate shows a region (I) with a large resistance, where we expect the semiconductor band gap.<sup>1</sup> Note that the resistance measured in region I is only a few  $\text{M}\Omega$  (see also the linetrace in Fig. 6.2a), which is low for a band gap. Region II is the electron regime described before. The non-local resistance ( $R_{\text{NL}} = V_{\text{NL}}/I$ ) as plotted in Fig. 6.1d is obtained by applying a current in one corner and measuring the voltage at the other corner of the Hall bar (Fig. 6.1b). In region II, there is almost no resistance, there is no current flow along the voltage measurement apparatus because the bulk conducts.

<sup>1</sup>For a more detailed description of the resistance map see chapter 5 Fig. 5.1 and Ref. 109.

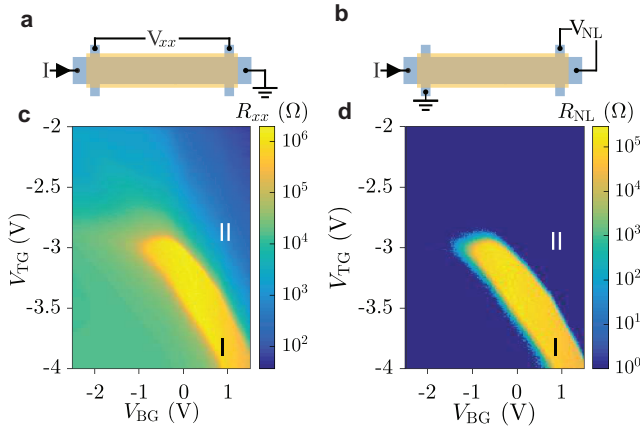


Figure 6.1: **Local and non-local conductance in a Hall bar.** **a** Schematic Hall bar devices are presented with the electrical setup for a local measurement ( $V_{xx}$ ) and **b** non local measurement ( $V_{NL}$ ). **c-d** The colorplots show the longitudinal and non-local resistance ( $R_{xx}$  and  $R_{NL}$ ) as function of top and bottom gate voltages ( $V_{TG}$  and  $V_{BG}$ ). A region of high (I) and low (II) resistance are indicated. This figure is adapted from Ref. [138].

In contrast, in region I a resistance of the order of 100 k $\Omega$  is measured, which could either be due to diffusive transport through the bulk, or edge transport. The diffusive transport is unlikely because the longitudinal resistance is only suppressed by a factor of  $10^{-1}$ . Theoretically a suppression of  $e^{-\pi S} \xrightarrow{S=5} 10^{-7}$  is expected, where  $S$  is the number of squares in the geometry [143]. In case the edges of the sample conduct, the suppression is governed by the ratio of the path lengths, which is of the order 10. Therefore we conclude that significant edge transport is observed in region I.

In order to study the origin of the resistance in region I, a temperature dependence measurement is performed. In Fig. 6.2b the inverse longitudinal resistance is plotted at different temperatures. The resistance depends on temperature following  $e^{-\sqrt{1/T}}$ , which is not consistent with the expected Arrhenius law of  $e^{-1/T}$ . This temperature dependence is found for models describing variable range hopping in one dimension or Coulomb dominated hopping in one or two dimensions [144], consistent with one-dimensional edge channels.

Exclusively investigating the bulk properties is done with a corbino disc, since no edges connect the two contacts directly. This allows us to study whether the current measured in the non local measurement is entirely edge current, or there is still a bulk component. Two terminal measurement are performed on a corbino with inner radius 50  $\mu\text{m}$  and outer radius 120  $\mu\text{m}$ . The conductivity reaches the minimum value we could measure in region I, on the order of  $10^{-10} \Omega^{-1}$  (Fig. 6.2c). In Fig. 6.2d, the temperature dependence of the conductivity fits the Arrhenius law, as expected. The bulk conductivity is thus suppressed, suggesting that the edge conduction is dominant in the non-local Hall bar measurement. A study of a multi-terminal corbino geometry revealed the carriers in the edge channels are electrons [137]. In summary, edge conduction due to electron accumulation at the physical edges of the InAs quantum well is measured.

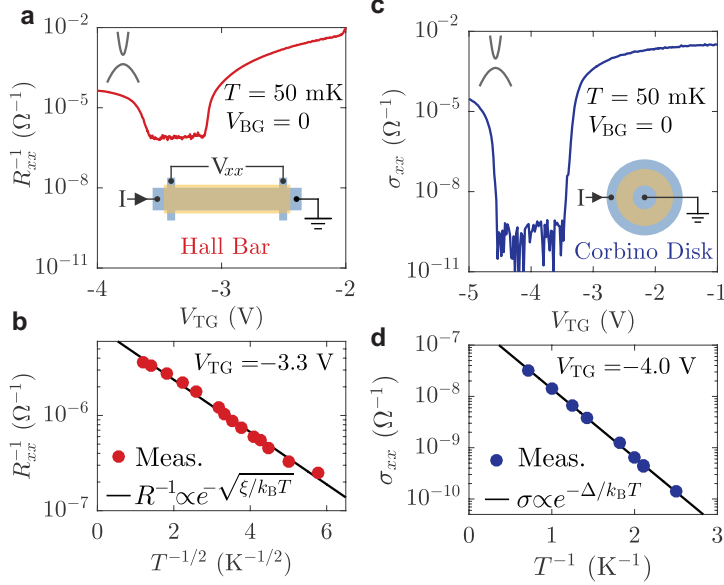


Figure 6.2: **Temperature dependence of conductance in Hall bar and corbino geometry.** **a,c** The inverted longitudinal resistance  $R_{xx}^{-1}$  and longitudinal conductivity  $\sigma_{xx}$  as a function of top gate voltage  $V_{TG}$  for the Hall bar and corbino geometries, respectively. The devices are schematically shown in the insets and the bottom gate voltage and temperature are indicated. **b,d** Temperature dependence and fit of  $R_{xx}^{-1}$  and  $\sigma_{xx}$  with the functional form presented at the indicated  $V_{TG}$ . The gap extracted from the Arrhenius law is  $2\Delta/k_B = 6.2$  K. This figure is adapted from Ref. [138].

## 6.2. EXPERIMENTAL SETUP

The quantum well is MBE grown on a GaSb substrate serving as a global bottom gate (Fig. 6.S4). The superconducting electrodes are made of sputtered NbTiN with a spacing of 500 nm and a width of 4  $\mu\text{m}$ . NbTiN has a bulk superconducting gap of 2 meV and a critical temperature of 13 K. A SiN<sub>x</sub> dielectric separates the top gate from the heterostructure. Electrical quasi-four terminal measurements (see Fig. 6.3b) are performed in a dilution refrigerator with an electron temperature of 60 mK unless stated otherwise.

The electron density in the InAs quantum well is altered by using the electrostatic gates,  $V_{tg}$  and  $V_{bg}$ , located above and below the 2DEG. Decreasing the density subsequently increases the normal state resistance  $R_n$  and reduces the switching current  $I_s$  as shown in Fig. 6.4a. A full resistance map as a function of top and bottom gate is shown in the Fig. 6.S5. The Josephson junction is first characterized at  $V_{tg} = 0$  V and  $V_{bg} = -1.65$  V, where the largest switching current is observed. From the IV trace in Fig. 6.4a we estimate an induced superconducting gap of 0.4 meV and, using the corrected OBTK model [145], a transmission of  $T = 0.73$ . The junction is quasi-ballistic because the mean free path of 2.8  $\mu\text{m}$  (extracted from a Hall bar device on the same wafer (see Fig. 6.S1) is larger than its length  $L$  of 500 nm. The large superconducting gap and high transmission value indicate a high quality InAs Josephson junction.

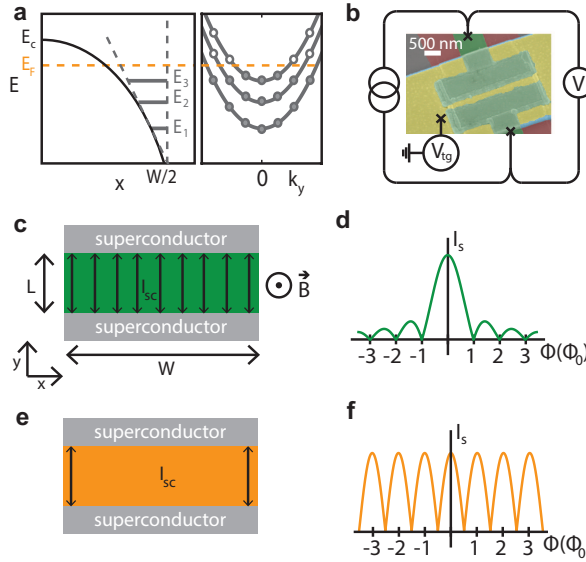


Figure 6.3: **Fermi level pinning and superconducting quantum interference.** **a** Sketch of the conduction band minimum around the edge of a 2DEG with Fermi level pinning at  $W/2$ . The band bending leads to a roughly triangular quantum well in the vicinity of the edge, therefore one-dimensional sub bands form of which three are drawn, as an example. The orange dashed line indicates the Fermi level corresponding to the current distribution in **e**. **b** False colored SEM image of the device with dimensions  $W = 4 \mu\text{m}$  and  $L = 500 \text{ nm}$ , where the quasi-four terminal measurement setup is added. Red is the mesa, green the NbTiN contacts, blue  $\text{SiN}_x$  dielectric and yellow the gold top gate. **c** Schematic representation of a Josephson junction of width  $W$  and length  $L$ . A homogeneously distributed supercurrent  $I_{sc}$  is running through the whole junction, resulting in **d** a Fraunhofer SQUID pattern. **e** If supercurrent only flows along the edges of the sample, **f** a SQUID pattern is observed.

### 6.3. SUPERCONDUCTING QUANTUM INTERFERENCE

SQUID measurements have successfully been used before to gather information on the supercurrent density profile in Josephson junctions [134, 135, 146]. This is typically done, using Dynes-Fulton approach [27], which connects the critical current dependency on magnetic field  $I_c(B)$  and the zero-field supercurrent density profile  $j(x)$  with a Fourier transform. It was originally developed for tunnel junctions, but can also be applied to transparent junctions under several assumptions. Firstly, we should have a sinusoidal current-phase dependency, which is in accordance with the transmission value and temperature in our experiment [147]. Secondly, the Andreev levels, that carry supercurrent in the junction, may only weakly deviate from the longitudinal propagation. Our junction satisfies this constraint since the superconducting coherence length  $\zeta = \hbar v_F / \Delta \approx 1.3 \mu\text{m} > L$  [28]. If both assumptions hold, we expect a Fraunhofer SQUID pattern in the case of homogeneous current distribution (Fig. 6.3c and 6.3d) and a SQUID pattern in the case of current flowing along the edges (Fig. 6.3e and 6.3f).

A SQUID measurement at the largest switching current reveals a Fraunhofer like pattern as shown in Fig. 6.4b. The central lobe is twice as wide as the side lobes and the amplitude decreases as expected. The slight asymmetry in the amplitudes we attribute to

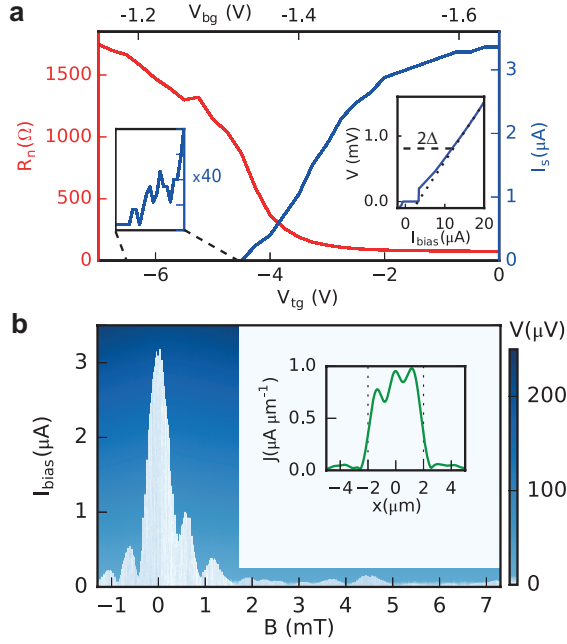


Figure 6.4: **Characterization of the Josephson junction.** **a** Normal state resistance  $R_n$  and switching current  $I_S$  at the respective top gate  $V_{tg}$  and bottom gate  $V_{bg}$  voltages. The left inset depicts a separate measurement at the indicated gate voltages, where a smaller current bias step size is used for higher resolution. The right inset shows an IV trace at  $V_{tg} = 0$  V and  $V_{bg} = -1.65$  V, where two dashed lines are added for extraction of the induced superconducting gap  $\Delta$  and the excess current. **b** The measured voltage as function of the applied current  $I_{bias}$  and perpendicular magnetic field  $B$  at  $V_{tg} = 0$  V and  $V_{bg} = -1.65$  V. The inset depicts the calculated supercurrent density along the width of the device that is indicated by the dotted lines.

breaking of the mirror symmetry of the sample in the direction along the current [32]. The effective length of the junction [ $\lambda = \delta B_{lobe}/(\Phi_0 \cdot W)$ ] of 1.2  $\mu\text{m}$  is extracted from the periodicity of the SQI pattern. Flux focusing due to the Meissner effect causes it to be larger than the junction length ( $\lambda > L$ ) [33]. The extracted current density profile, plotted in Fig. 6.4b, is close to uniform. The supercurrent is thus dominated by bulk transport as expected at these gate voltages.

The interference pattern in Fig. 6.4b deviates from the expected pattern after the second lobe. Recently a similar distorted Fraunhofer tail was observed and discussed in graphene [148]. The perpendicular magnetic field exerts a Lorentz force on the electron and holes suppressing the formation of Andreev bound states. The suppression becomes relevant at a magnetic field scale of  $\Delta/eLv_F$ , equal to 1 mT in our case, roughly agreeing with the observation. The analysis only holds for the bulk of the junction, since the scattering at the edges reduces the difference in the electron and hole motion in a magnetic field.

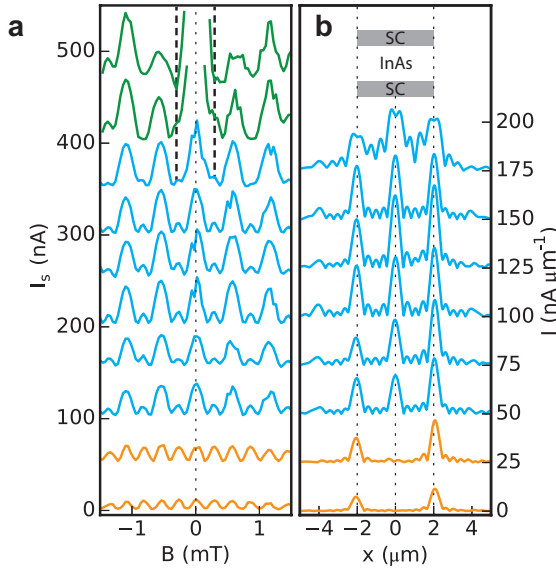


Figure 6.5: **Gate voltage dependence of SQI pattern.** **a** The switching current plotted as function of perpendicular magnetic field and **b** the corresponding current density along the width of the device (see inset), assuming the validity of the Dynes-Fulton approach. The gate values used are from bottom to top:  $V_{\text{tg}}$  -5.4 V to -3.6 V (0.2 V step) and  $V_{\text{bg}}$  -1.270 V to -1.396 V (0.014 V step). The green, blue and orange traces are Fraunhofer, even-odd and SQUID patterns, respectively. Since the current is only swept up to 100 nA, the green traces are not suitable for extracting a supercurrent density profile. The traces are offset by 50 nA in **a** and 25 nA/ $\mu\text{m}$  in **b**.

## 6.4. GATE DEPENDENCE

Next we study the SQI pattern as the Fermi level is decreased by tuning the top gate to more negative values. The upper two (green) traces in Fig. 6.5a have a wide central lobe, stemming from a Fraunhofer pattern. The side lobes however do not decrease in amplitude as expected but seem to be constant, as for an SQUID pattern. We conclude that we are in the transition regime from bulk to edge transport. The effective length is  $\lambda = 1.7 \mu\text{m}$ , different from before, which we believe is due to different vortex pinning because of the larger magnetic field range of the measurement (details in Sec. 6.8.2). In the third (first blue) trace we observe that the first nodes turn into peaks, which is highlighted by the dashed lines. Therefore the transition to a SQUID pattern is completed. Curiously the amplitude and width of the peaks are alternating in the blue traces in Fig. 6.5a. The even-odd pattern is composed of an  $h/e$  and  $h/2e$  periodic signal. An even-odd pattern was observed before in Pribiag *et al.* [135]. In comparison, in this work the amplitude difference in the lobes is much larger and the pattern is visible over a large gate range. The calculated supercurrent density profiles in Fig. 6.5b have a central peak that is physically unlikely considering the device geometry. The cause of this intriguing interference pattern will be discussed in more detail later. Reducing  $V_{\text{tg}}$  further we find a clear  $h/2e$  periodic SQUID interference pattern in the bottom two (orange) traces. This is a strong indication of edge conduction in our device, confirmed by the edge transport

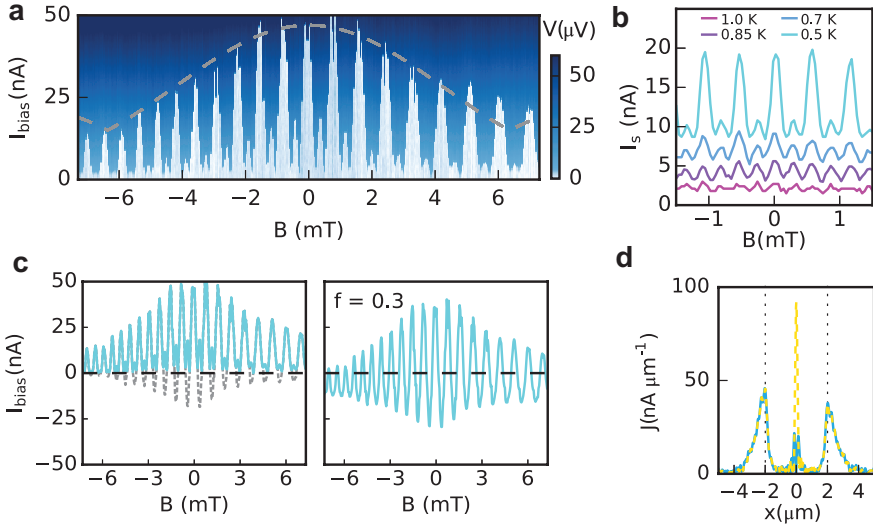


Figure 6.6:  $h/e$  SQUID pattern. **a** Measured voltage as a function of  $I_{\text{bias}}$  and magnetic field  $B$  at  $V_{\text{tg}} = -5$  V and  $V_{\text{bg}} = -1.29$  V. **b** Switching current versus the magnetic field for different temperatures at the same gate voltages as **a**. The traces are offset by 5 nA for clarity. **c** In the first panel, the blue line is the switching current as a function of magnetic field as extracted from **a**. The gray dashed line depicts the pattern after flipping every other node as is usually done in the Dynes-Fulton analysis [27]. The second panel shows the same pattern as **a** with an offset of 11 nA subtracted, equal to a factor of 0.3 times the switching current at zero magnetic field. **d** Current density profile, calculated from the SQI pattern of **a**. The blue trace uses equation (1), thus correcting the vertical offset in the SQI pattern. The yellow dashed trace is extracted without this correction.

6

only in the extracted supercurrent density profiles in Fig. 6.5b. The transition from bulk to edge transport as a function of gate voltage is measured in several other Josephson junctions (Fig. 6.S6). Since we observe supercurrent through the trivial edge states of an InAs quantum well, we conclude that a clear demonstration of superconducting edges alone does not prove induced superconductivity in topological edge states.

### 6.5. EVEN-ODD PATTERN

We now return to the remarkable  $h/e$  SQUID signal to investigate its origin. Figure 6.6a shows a more detailed measurement in this gate regime, the even-odd pattern is observed over more than 25 oscillations. The envelope of the peaks is attributed to the finite width of the edge channels. The effect is suppressed by raising the temperature (see Fig 6.6b), for  $T > 850$  mK a regular  $h/2e$  SQUID pattern remains. The origin cannot lie in effects that occur beyond a certain critical magnetic field, like  $0 - \pi$  transitions [41], edge effects [29, 149] and a topological state, because we observe the even-odd pattern around zero magnetic field as well. An effect that does not rely on magnetic field and is strongly temperature dependent is crossed Andreev reflection [150].

The lowest order crossed Andreev reflection (up to electron-hole symmetry) is schematically depicted in Fig. 6.7a. An electron travels along one edge, whereafter a hole is

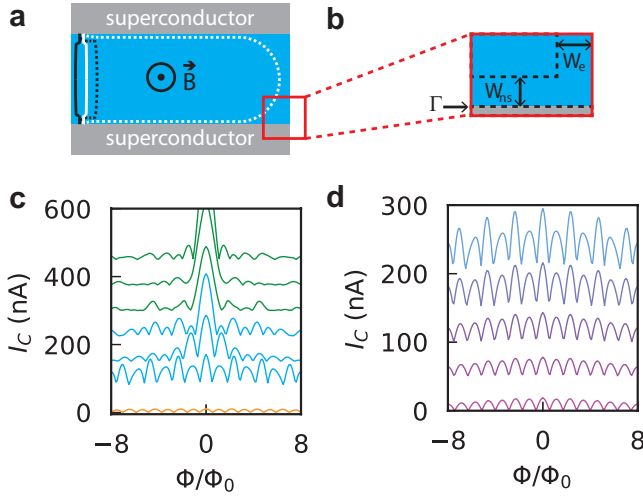


Figure 6.7: **Tight binding model of the Josephson junction.** **a** Schematic representation of two crossed Andreev processes. The black and white lines indicate electron and hole trajectories or vice versa. The solid lines represent a single edge Andreev state and the dotted lines a crossed Andreev state. **b** Detailed sketch of one corner of junction in our tight binding mode indicating the widths  $W_{ns}$  and  $W_e$ , and tunnel barrier  $\Gamma$ . **c** Calculated SQI patterns at overall chemical potential ranging from  $-0.06$  eV to  $0.18$  eV ( $0.04$  eV step) at  $0.46$  K and **d** at temperatures  $0.4$  K,  $0.9$  K,  $1.4$  K,  $1.9$  K,  $2.3$  K at a chemical potential of  $-0.2$  eV. Traces are offset by  $10$  nA for clarity. In **c** the color represents the type of interference pattern, green for Fraunhofer, blue for even-odd and orange for SQUID, respectively.

retroreflected over the other edge. This process alone is independent of the flux through the junction, but still adds to the critical current [151]. Higher order processes that include an electron that encircles the junction completely pick up an  $h/e$  phase when a flux quantum threads through the junction, hence the supercurrent becomes  $h/e$  periodic [152, 153]. Additionally, interference processes between crossed Andreev and single edge Andreev states could lead to a  $h/e$  contribution [154]. It is important to note that the critical current is  $h/e$  periodic in flux through the sample, but still  $2\pi$  periodic in superconducting phase difference.

Forming crossed Andreev states in the junction is only possible if the particles can flow along the contacts. Electrostatic simulations indeed show a large electron density close to the contacts at gate voltages where the bulk is already depleted (see Fig. 6.S7), because of local screening of the top gate. Nevertheless the needed coherence length for a crossed Andreev reflection is on the order of  $10$   $\mu\text{m}$ , where the estimated superconducting coherence length (from bulk values) is  $1.3$   $\mu\text{m}$ . The difference between these values remains an open question.

## 6.6. PHENOMENOLOGICAL AND TIGHT BINDING MODEL

The phenomenological model proposed by Baxevanis *et al.* considers both single edge and crossed Andreev states [151]. In our device we expect the lowest order crossed Andreev states to contribute most because of the short coherence length. Combining



their flux insensitive contribution to the critical current and the usual  $h/2e$  periodic contribution from single edge Andreev bound states, the model predicts an even-odd or  $h/e$  SQUID pattern:

$$I_c(\Phi) = I_0 |\cos(\pi\Phi/\Phi_0) + f|. \quad (6.1)$$

Where  $I_0$  the critical current at zero magnetic field and  $\Phi$  is the applied flux. Constant  $f$  can be arbitrarily large, it depends on the ratio  $\Gamma$  between the probability to Andreev reflect on a node versus the probability to scatter to another edge and is exponentially suppressed by the width of the sample:

$$f \sim \Gamma^{-1} \frac{k_B T}{\Delta} e^{-2\pi(k_B T/\Delta)(W/\zeta)}. \quad (6.2)$$

The predicted pattern is thus the absolute value of a vertically offsetted cosine function. That is exactly the pattern we measured in Fig. 6.5a and 6.6a,c as both the amplitude and width of the lobes alternate. From the data we estimate  $f = 0.3$  (Fig. 6.6c) and, using the other known parameters, find  $\Gamma \sim 10^{-1}$ . Taking the Fourier transform in the Dynes-Fulton analysis, offset  $f$  leads to a non-physical current density around zero, like we observe in the current density profiles in Fig. 6.5b and the yellow dashed line in Fig. 6.6d. Moreover, the Dynes-Fulton approach is not valid here since crossed Andreev reflection does not meet the second assumption of having straight trajectories only. We can compensate the crossed Andreev contribution by subtracting the constant offset of  $f \cdot I_0 = 11$  nA. This results in a current distribution with mainly current along the edges, as plotted in the blue trace of Fig. 6.6d. We did not take into account that  $I_0$  is actually not constant due to the Fraunhofer envelope of the SQI pattern, so the current density in the center of the junction is not entirely eliminated.

Even though the SQI pattern from the phenomenological model is in qualitative agreement with our data, we also present a tight binding model of system in order to connect it directly to experimentally accessible parameters (for details see Sec. 6.8.3). In the microscopic model we include the superconducting gap as measured, the width of the paths along the contacts  $W_{ns}$  of 20 nm (extracted from the Fraunhofer envelope in Fig. 6.6a), and Fermi level pinning on the edges leading to edge current in the region  $W_e$ . It is crucial to also take into account a tunnel barrier  $\Gamma$  at the contacts that has a magnitude consistent with the measured transmission value. This barrier enhances normal reflection and therefore elongates the length electrons and holes travel before Andreev reflecting (Fig. 6.S8). Incorporating these experimental values we find an  $h/e$  SQUID pattern. Emulating the experimental gating effect by changing the overall chemical potential results in a crossover from even-odd to Fraunhofer (Fig. 6.7c), consistent with the measurement in Fig. 6.5. As a check,  $W_{ns}$  is reduced in steps to zero, which results in a SQUID pattern (Fig. 6.S9). Additionally, in Fig. 6.7d we observe that increasing the temperature indeed smears out the even-odd pattern and leaves us with a regular SQUID pattern, similar to the experimental data in Fig. 6.6b. Summarizing, both the phenomenological model and the microscopic model support our hypothesis of the  $h/e$  SQUID originating from crossed Andreev states.

## 6.7. CONCLUSION

We have experimentally shown that trivial edge states can support highly coherent superconducting transport that also becomes visible in an  $h/e$  periodic SQI pattern. Both effects have been considered as possible signatures for inducing superconductivity in topological edge states before [134, 135]. Therefore we conclude that superconducting edge transport and an  $h/e$  SQUID pattern only, cannot distinguish between topological and trivial edge states, nor can it be considered a definite proof for a topological phase.

## 6.8. SUPPLEMENTARY MATERIAL

### 6.8.1. HALL BAR MEASUREMENT

A Hall bar device with length  $80\ \mu\text{m}$  and width  $20\ \mu\text{m}$  is fabricated on the same wafer. The mobility and density as a function of top and bottom gate are shown in Fig. S3. The following parameters are extracted and calculated at  $V_{tg} = 0\ \text{V}$  and  $V_{bg} = 0\ \text{V}$ , using the effective mass of InAs  $m^* = 0.04\ m_e$  [109] and Lande g-factor 11.5 [66].

$$n = 1.1 \cdot 10^{16}\ \text{m}^{-2}$$

$$\lambda_{MFP} = \hbar\mu/e\sqrt{2\pi n} = 2.8\ \mu\text{m}$$

$$\mu = 1.6 \cdot 10^5\ \text{cm}^2/(\text{Vs})$$

$$E_{\text{thouless}} = \hbar v_F/L = 6.3\ \text{meV}$$

$$v_F = \hbar\sqrt{2\pi n}/m^* = 7.6 \cdot 10^5\ \text{m/s}$$

$$E_{\text{zeeman}} = g\mu_B B \stackrel{10\text{mT}}{=} 0.0066\ \text{meV}$$

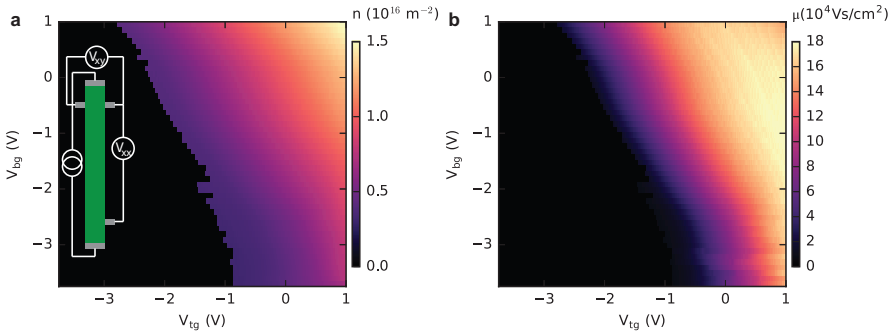


Figure 6.S1: **Hall bar measurement.** **a** The density of the Hall bar device (inset) is plotted as a function of top gate and bottom gate voltage. Each line is cut off at the point where the density became too low to measure. In **b** the mobility is plotted for the same gate voltage ranges as in **a**.

### 6.8.2. FLUX FOCUSING AND VORTICES

The contact geometry causes a part of the flux to be focused in the junction due to the Meissner effect. The NbTiN contacts have a width of  $4\ \mu\text{m}$  and a length of  $1\ \mu\text{m}$ . If there are no vortices in the NbTiN (type II superconductor), the maximum amount of flux will be threaded to the junction. If there are vortices, a flux quantum per vortex penetrates the superconductor and will therefore not be focused through the junction. Experiments

on strip geometry Nb films show that the critical field at which vortices appear in the strip is given by  $B_m = \Phi_0/W^2$  [155], in our system equal to 2 mT. We assume that the vortices settle at the beginning of a measurement, since the magnetic field is swept relatively fast to the starting point, whereafter it is changed in small steps before a current bias trace is measured. Then different sweep ranges will have different periodicities, since the number of vortices alter the flux focusing. More specifically, smaller sweep ranges will have smaller periodicity, because there are less vortices and therefore more flux focusing. This is what we see if we compare the flux periodicities in Fig. 2(b) and Fig. 3(a) in the main text. To reassure this observation we show a wider range magnetic field scan of the SQUID regime in Fig. S4. The observed periodicity is used to extract an effective length of  $1.2 \mu\text{m}$ , which is the same as for the Fraunhofer pattern in Fig. 2(b) and even-odd pattern in Fig. 4(a).

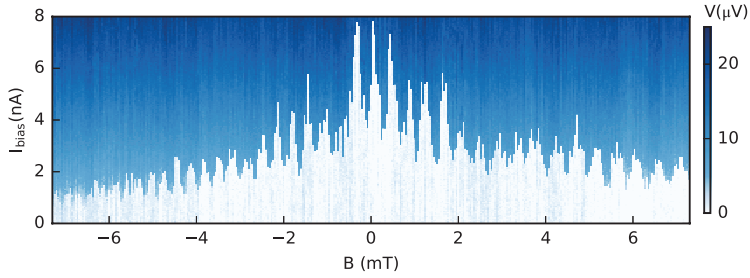


Figure 6.S2: **SQUID measurement.** SQUID measurement at  $V_{\text{tg}} = -7 \text{ V}$  and  $V_{\text{bg}} = -1.15 \text{ V}$ . The observed SQUID pattern has a period of 0.4 mT, from which an effective length of  $1.2 \mu\text{m}$  is estimated.

### 6.8.3. TIGHT BINDING MODEL

We have taken the following Hamiltonian for tight binding simulations:

$$H = \left( \frac{\hbar^2(k_x^2 + k_y^2)}{2m_{\text{eff}}} - \mu(x, y) \right) \tau_z + \alpha(k_x \sigma_y - k_y \sigma_x) \tau_z + g \mu_B B(x) \sigma_z + \Delta(x) \tau_x, \quad (6.S1)$$

where  $\sigma$  Pauli matrices correspond to the spin degree of freedom, and  $\tau$  – to the electron and hole one. It is discretized on a square lattice with lattice constant  $a = 2 \text{ nm}$ . The normal part of a SNS junction is represented as a rectangle  $-L/2 \leq x \leq L/2$  and  $-W/2 \leq y \leq W/2$ , the superconducting parts – as translationally invariant in  $x$  direction stripes with  $-W/2 \leq y \leq W/2$ . Proximity-induced pairing potential  $\Delta(x)$  is zero in a normal part and constant in a superconducting part of the system, with a step-like transition. The magnetic field is assumed to be fully screened by the superconductors. Its impact is included as Zeeman term and via Peierls substitution.

At first realistic values of  $\alpha = 5 \cdot 10^{-12} \text{ eV} \cdot \text{m}$  and  $g = 11.5$  for the Rashba and Zeeman term were used to verify that they do not play an important role in this parameter regime. After we were sure that Zeeman and Rashba terms can be neglected, we have put  $\alpha = 0$  and  $g = 0$  for the sake of numerical performance. This allowed to decouple spins and decrease the dimensionality of the Hamiltonian twice, since both decoupled subblocks contribute equally to the current.

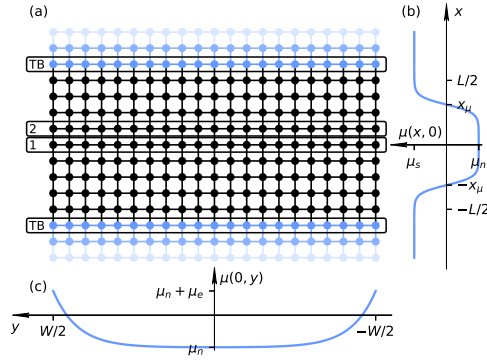


Figure 6.S3: **Tight binding model a** Schematic representation of a tight binding model. Bogolyubov-de Gennes Hamiltonian is discretized on a square lattice. Superconducting sites of the system have a blue color, normal – black. A tunnel barrier is created, using one row of sites with decreased chemical potential (marked TB on the scheme). The current was calculated from Green's function of sites, marked 1 and 2 on the scheme (see the detailed explanation below). **b** Chemical potential profile for  $y = 0$ . Offset between location of chemical potential step and superconducting region together with the tunnel barrier leads to formation of scattering channel between edges. **c** Chemical potential profile for  $x = 0$ . Band bending is represented with an increased chemical potential at the edges, leading to edge conductivity in a doped regime.

Chemical potential  $\mu(x, y)$  is selected to capture primary features of the device: band bending near the edges and screening near the NS boundaries top gate. It has the following form:

$$\mu(x, y) = \frac{\mu_{\text{norm}} + \delta\mu_{\text{edge}}(y)}{2} \left( \tanh \frac{x + x_\mu}{\lambda_\mu} - \tanh \frac{x - x_\mu}{\lambda_\mu} \right) + \frac{\mu_{\text{sc}}}{2} \left( 2 - \tanh \frac{x + x_\mu}{\lambda_\mu} + \tanh \frac{x - x_\mu}{\lambda_\mu} \right), \quad (6.S2)$$

where

$$\delta\mu_{\text{edge}}(y) = 2\mu_e e^{-W/2\lambda_e} \cosh \frac{y}{\lambda_e} \quad (6.S3)$$

is the term, that introduces band bending near the edges of a normal part.  $\mu_{\text{norm}}$  and  $\mu_{\text{sc}}$  are chemical potentials in gated area (primarily normal part) and area screened by the superconducting contacts. If normal part is governed to the insulating state with negative  $\mu_{\text{norm}}$ , the offset between  $L/2$  and  $x_\mu$  leads to formation of a conducting channel on the NS boundaries of the junction, with a width:

$$W_{\text{ns}} = L/2 - x_\mu. \quad (6.S4)$$

The tunnel barrier on the NS interface was represented as a single row of sites with a chemical potential reduced by  $\Delta\mu_{\text{TB}}$ .

The finite-temperature critical current of the SNS junction was calculated by maximizing the current-phase dependency, similarly to the approach, used in [156]. The

Green's function was numerically calculated for several Matsubara frequencies on two neighboring rows of the sites in the normal part of the junction, then the current was obtained by the summation:

$$I = \frac{2ek_B T}{\hbar} \sum_{n=0}^{N_{\max}} (\Im \text{tr} H_{21} G_{12}(i\omega_n) - \Im \text{tr} H_{12} G_{21}(i\omega_n)). \quad (6.S5)$$

Here  $H_{21}$  and  $G_{21}$  denote hopping matrix and Green's function subblock from cells of row 1 to row 2, indicated on Fig. 6.S3 (all the hoppings, that form a cut through the system), and vice versa.  $\omega_n = (2n + 1)\pi k_B T$  is the  $n$ -th Matsubara frequency. Value  $N_{\max}$  was obtained dynamically, based on the estimated convergence rate. The Green's functions were calculated, using package Kwant [99].

The numerical values of parameters, used for simulations, are presented in Table 6.S1. A lattice constant of  $a = 2$  nm was selected small enough to capture characteristic length scales of an edge and NS boundary current channels.

$W$ [nm]	$L$ [nm]	$\lambda_e$ [nm]	$\lambda_\mu$ [nm]	$x_\mu$ [nm]	$m_{\text{eff}}/m_e$	$\Delta$ [eV]	$\mu_{\text{sc}}$ [eV]	$\delta\mu_e$ [eV]
400	200	28	1	0 ÷ 50	0.04	$4 \cdot 10^{-4}$	0.2	0.15

Table 6.S1: Numerical parameters, used for tight-binding simulations.

### 6.8.4. SUPPLEMENTARY FIGURES

GaSb	3 nm
AlSb	50 nm
InAs	12.5 nm
AlAsSb	100 nm
GaSb	150 nm
GaSb	substrate

Figure 6.S4: **2DEG heterostructure stack.** The heterostructure is MBE grown and consists of the following layers: a doped GaSb substrate; a 150 nm GaSb buffer; the quantum well with an AlAsSb barrier of 100 nm, 12.5 nm InAs and a 50 nm AlSb top barrier; and a 3 nm GaSb capping layer. The latter is used to prevent oxidation of the AlSb. This stack, especially the capping layer, leads to unintentional doping in the InAs quantum well [141].

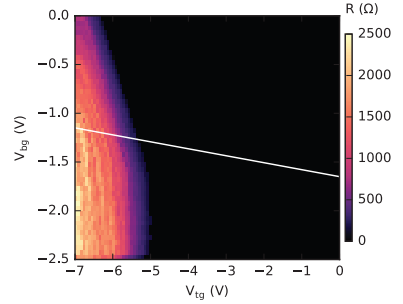


Figure 6.S5: **Resistance map.** Two terminal resistance of the Josephson junction is plotted as a function of top gate and bottom gate voltage ( $V_{\text{tg}}$  and  $V_{\text{bg}}$ ). The solid white line indicates the gate voltages at which the superconducting quantum interference is investigated in the main text.

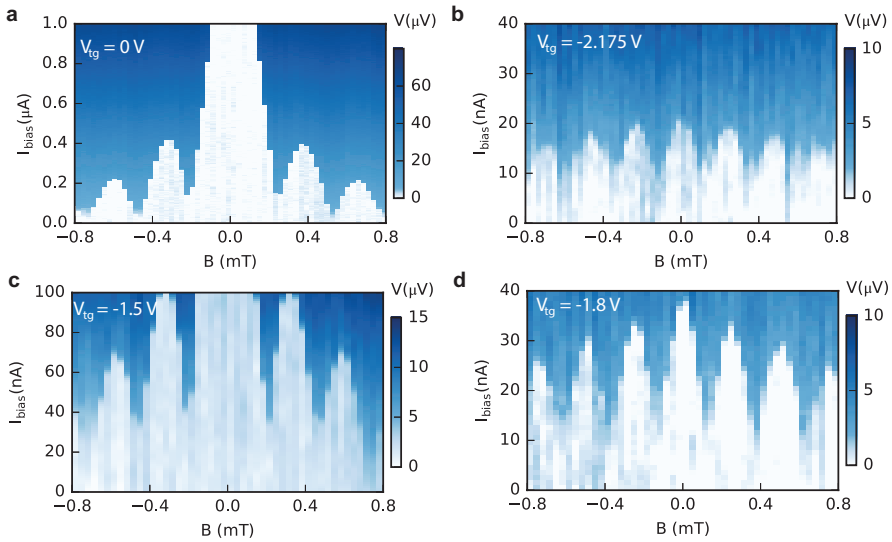


Figure 6.S6: **Fraunhofer to SQUID in two other devices.** SQI data at the indicated top gate voltages is shown of two lithographically similar devices ( $L = 500 \text{ nm}$ ,  $W = 4 \mu\text{m}$ ). The Fraunhofer SQI patterns are shown in **a** and **c**, and the SQUID patterns in **b** and **d** for device 2 and 3, respectively. For all figures  $V_{bg} = 0 \text{ V}$ . Clearly in both devices the SQI pattern turns from Fraunhofer to SQUID by decreasing the gate voltage.

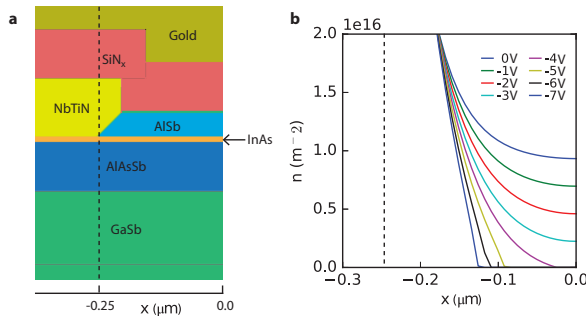


Figure 6.S7: **Simulation contact edge.** Electrostatic simulations are performed using a finite element Poisson solver. **a** The device geometry as used in the simulation. The  $\text{SiN}_x$  dielectric is 100 nm thick and the NbTiN 120 nm, all other thicknesses can be found in Fig 6.S4. **b** The electron density profile is changing as the top and bottom gate voltages are swept. The top gate voltage is indicated in the legend. In the lower gate voltage traces the electrons in the bulk are depleted while there is still a large electron density in the vicinity of the contacts. For clarification, the  $x$ -axis value where the NbTiN contact is on top of the InAs is indicated by the dashed line in both **a** and **b**. The top gate is screened close to the contacts due to the triangular shape of the top AlSb barrier. This shape is caused by isotropic wet etching of the mesa.

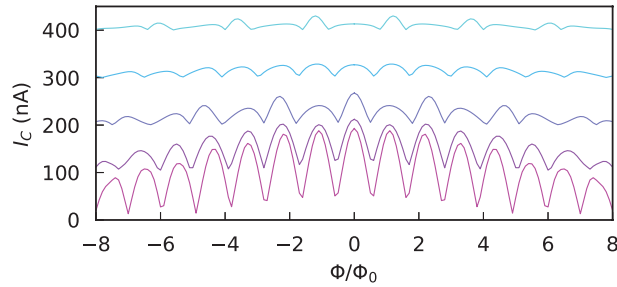


Figure 6.S8: **Tunnel barrier dependence in tight binding model.** Tight binding calculation of the superconducting quantum interference as a function of tunnel barrier strength at the contact. Increasing the tunnel barrier height leads to enhanced normal reflection with respect to Andreev reflection. The electrons or holes then have a higher chance of traversing along the contact before Andreev reflecting. Forming a crossed Andreev states requires the charge carriers to traverse around the junction fully. Therefore enhanced normal reflection is beneficial for forming these states and the resulting even-odd SQI pattern. Here we plot the SQI patterns for a tunnel barrier strength ranging from 0.6 eV to 1.40 eV (bottom to top) in 0.2 eV steps.

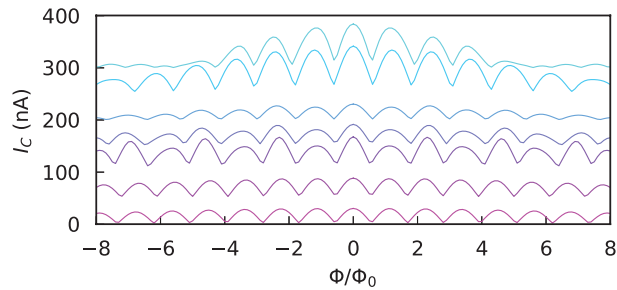


Figure 6.S9:  **$W_{ns}$  dependence in tight binding model.** Tight binding calculation of the superconducting quantum interference as a function of width of the channel along the edge. As a sanity check: if the width is 2 nm (bottom trace), we do not see even-odd effect. Increasing the width (in 8 nm steps up to 50 nm), increases the number of channels along the contact and the coherence length, up to the point that the 1D channel become 2D and the even-odd effect reduces again.

# 7

## EVEN-ODD SUPERCONDUCTING QUANTUM INTERFERENCE IN InSb JOSEPHSON JUNCTIONS

*We study superconducting quantum interference in Josephson junctions made from InSb flakes. An even-odd effect in the amplitude and periodicity of the superconducting quantum interference pattern is found. Interestingly, the occurrence of this pattern coincides with enhanced edge conduction at both edges of the flake. We argue the even-odd effect is due to crossed Andreev reflection, a process where the Andreev pair splits up over the two edges.*



## 7.1. INTRODUCTION

Induced superconductivity in semiconductors with strong spin-orbit interaction attracted much interest for its potential applications in topological quantum computation [76, 157, 158]. A semiconducting Josephson junction (JJ) offers a platform to study the induced superconductivity by means of superconducting quantum interference (SQI) [21]. This technique allows one to obtain the transport regime (ballistic or diffusive) of the JJ and reconstruct the current density distribution via the Dynes-Fulton approach [27]. Recently, induced superconductivity in edge channels in the quantum Hall regime [159] and in a predicted two-dimensional topological insulator [134, 135] are investigated using SQI. Additionally, an  $h/e$  periodic oscillation, before connected to topological edge states [135], is observed on top of a  $h/2e$  background in a trivial InAs quantum well [160]. Here, we observe and discuss an even-odd effect in the SQI pattern of InSb JJs, a material known for its large  $g$ -factor [54] and strong SOI [161]. Furthermore, a purely  $h/e$  periodic SQUID oscillation is reported at reduced gate voltages. Because of the correlation of the even-odd pattern and enhanced edge conduction at both edges, we argue the effect is caused by crossed Andreev reflection. The quasiparticles of a single Andreev pair are spatially separated over the two edges, leading to a flux independent offset of the supercurrent.

## 7.2. EXPERIMENTAL SETUP

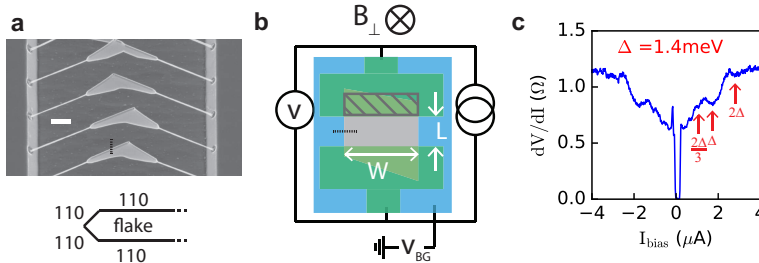


Figure 7.1: **InSb Flake Josephson junction.** **a** The top panel shows a scanning electron microscope (SEM) image of the InSb flakes, grown from two nanowires on an InP substrate [55]. The scale bar represents 500 nm. The bottom panel sketches the cross section of the flake, as highlighted by the dashed black line in **a** and **b**. All facets, top, bottom and edge have a 110 crystal direction. **b** Schematic Josephson junction device, where the flake (gray) is contacted by NbTiN (green), after being placed on the Si/SiO<sub>2</sub> substrate (blue). The superconducting contacts focus the perpendicular flux of the hatched area in the junction, due to the Meissner effect. The four terminal current bias measurement setup is indicated as well as the magnetic field direction. **c** Differential resistance  $dV/dI$  measurement of device I as a function of current bias  $I_{bias}$  at a bottom gate voltage  $V_{BG}$  of 2.4 V. A superconducting gap  $\Delta$  of 1.4 meV is extracted from the resonances at twice the gap edge and the multiple Andreev reflections, as indicated by the red arrows.

A flake is a small two-dimensional (2D) nanostructure that combines the flexibility of the nanowires in terms of fabrication and the possibility for more complex device geometries. Earlier works referred to flakes as nanosails [54] or nanosheets [52]. The InSb flakes are grown with the vapor-liquid-solid (VLS) technique, as described in detail in Ref. 55. For each flake, two nanowires are grown with a relative angle to each other,

governed by trenches in an InP substrate. Because of their perfect alignment, the two nanowires coalesce, and the growth continues in a two-dimensional manner, forming the flake (Fig. 7.1a). The two front and back facets of the flake, have a 110 crystal orientation. Additionally, the top facets of the flake that have two planes with a 110 crystal direction as sketched in the lower panel of Fig. 7.1a. This crystal direction is known for having electron accumulation at its surface [162, 163], due to doping via a lack of Sb atoms [164], what results in band bending. Considering the geometry we expect the band bending to be stronger at the edges of the flake that have two 110 facets, as schematically shown for device I and II in Fig. 7.2a,b.

The flakes are transferred to a Si/SiO substrate with a micromanipulator, that serves as a global bottom gate. Then, two NbTiN contacts are deposited after treating the surface with a sulfur solution to remove the native oxides [60, 61]. For devices I-III, the sulfur solution leaked underneath the etch mask, as apparent in the junction area in the scanning electron microscope (SEM) images in Fig. 7.2a,b and Fig. 7.5b. Compared to devices IV-VII, that do not show this underetching (Fig. 7.51), we did not observe a notable difference in the measurements. The contact separation  $L$ , width  $W$  of all devices are presented in Table 7.S1. The devices are measured in a four terminal current bias setup (Fig. 7.1b) at a temperature of 300 mK, unless stated otherwise.

The induced superconductivity is characterized with a differential resistance measurement of device I as a function of current bias (Fig. 7.1c). We observe the superconducting gap ( $\Delta$ ) and several multiple Andreev reflections within this gap, that we use to extract a value of  $\Delta = 1.4$  meV, consistent with values found earlier for NbTiN [61]. A transmission  $T$  of the JJ is 0.6 is estimated using the Octavio Blonder Tinkham Klapwijk model (Fig. 7.S2) [145]. The global bottom gate allows us to pinch off the switching current as presented for all devices in Fig. 7.S3.

### 7.3. EVEN-ODD SUPERCONDUCTING QUANTUM INTERFERENCE

Superconducting quantum interference (SQI) measurements are done by applying an out-of-plane magnetic field to the JJ. In case of a homogeneous supercurrent distribution, straight trajectories of the Andreev pairs, and  $W/L \gg 1$ , a Fraunhofer interference pattern is expected with a periodicity of one flux quantum ( $\Phi_0$ ) [21]. In Fig. 7.2c, we observe such a Fraunhofer pattern in device I at a bottom gate voltage  $V_{BG}$  of 15 V. However, the periodicity of  $1.5\Phi_0$  ( $\Phi_0 = h/2e$ ) is larger than expected. Note that the pattern is compensated already for flux focusing from the superconducting contacts, due to the Meissner effect (hatched area in Fig. 7.1b). The Andreev pairs are traveling mostly straight, since we estimate an induced superconducting coherence length  $\xi_s$  of  $1.2\mu\text{m}$  at  $V_{BG} = 15$  V, which is of the order of  $L$  [28]. Also, the current density distribution in Fig. 7.2e, reconstructed using Dynes-Fulton approach [27, 134], is homogeneous throughout the JJ. The JJ geometry of  $W = 1280$  nm and  $L = 240$  nm however, do not satisfy its constraint. Therefore we use a model for finite size JJs proposed by Barzykin *et al.* [31], where the supercurrent is calculated over all possible quasiparticle trajectories for either a ballistic or diffusive JJ. The final expressions for both are included in section 7.8.1 for convenience. We plot the ballistic model in Fig. 7.2c (dashed gray line), since the mean free path  $l_{MFP}$  at  $V_{BG} = 15$  V is similar to  $L$  (Fig. 7.3b). For the first three lobes of the SQI pattern, the calculated SQI pattern resembles the measured pattern well,

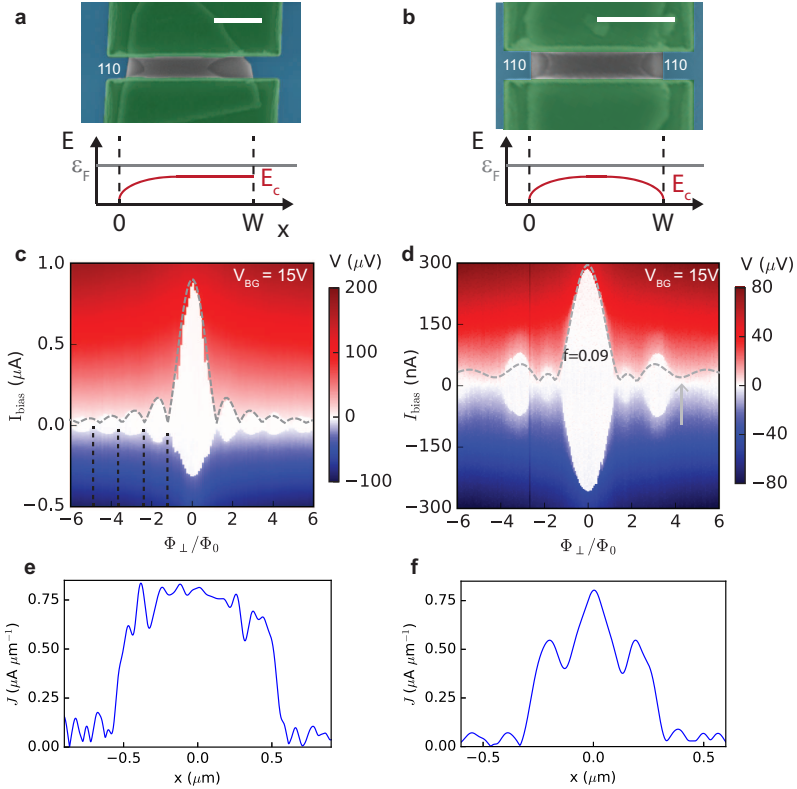


Figure 7.2: **Superconducting quantum interference.** **a-b** The upper panel shows a SEM image of device I and device II, respectively. The flake (grey) is deposited on a Si/SiO<sub>2</sub> substrate (blue) and contacted by NbTiN (green). The scale bar represents 500 nm. In the bottom panel, the energy of the bottom of the conduction band (red) is sketched along the width of the junction. Because of electron accumulation at the 110 surfaces, the band bottom bends down at the interface, and (a) conducting edge channel(s) remains, once the Fermi level  $\epsilon_F$  is lowered appropriately. **c** Voltage measured over device I as a function of current bias  $I_{\text{bias}}$  and normalized perpendicular magnetic flux  $\Phi_{\perp}/\Phi_0$ , at a bottom gate voltage  $V_{\text{BG}}$  of 15 V. The periodicity of the SQI pattern is highlighted by the dashed black lines. The dashed gray line is calculated following eq. 7.S3 [31], where we used device parameters as noted in section 7.8.1. **d** Same measurement as **c** of device II. The dashed gray line depicts the calculated SQI pattern (eq. 7.S3 [31]) with an offset  $f = 0.09$ . The gray arrow highlights the location of the third lobe, that is absent because the offset  $f$  is larger than its amplitude. **e** Current density distribution  $J$  extracted from the SQI pattern of **c**, using the Dynes-Fulton approach [27]. **f** Current density distribution extracted from **d**.

confirming the larger periodicity is due to the finite geometry of the JJ. The fourth lobe however is not well reproduced, which could be due to scattering off the edges, described in a recent theoretical work [149].

Interestingly, the SQI pattern of device II in Fig. 7.2d does not show the regular Fraunhofer pattern. The pattern displays an even-odd effect, the amplitude of the side lobes is not monotonically decaying, but alternating. The first side lobe has a smaller amplitude than the second, and the third side lobe amplitude is even absent. We hypothesize there is a positive, magnetic field independent offset from the expected interference pattern. We illustrate this argument by heuristically adding such an offset to an arbitrary interference pattern  $\mathcal{I}(\Phi)$ :

$$I_c(\Phi) = I_{c0} |\mathcal{I}(\Phi) + f| \quad (7.1)$$

Where  $I_{c0}$  is the critical current at zero magnetic field and  $f$  is the offset, it increases (decreases) the amplitude of the lobes with the same (opposite) sign. Examples of SQI patterns with different offsets are presented in Fig. 7.4c. In Fig. 7.2d, the dashed gray line represent a calculation using the the ballistic model (eq. 7.S3 [31]) with an offset of 0.09. The even-odd behaviour of the SQI pattern is qualitatively reproduced, supporting our hypothesis of a flux independent supercurrent.

The extracted current density distribution in Fig. 7.2f, reveals a large peak at the center of the device. Note that any magnetic field independent path through the junction would also show up at zero in the current density distribution, because the Dynes-Fulton analysis is based on a Fourier transform [27].

Taking these considerations into account, we formulate the following potential causes of the even-odd effect. Firstly, a current path through the center of the junction area could cause the even-odd SQI pattern. Secondly, it could show up in a junction with  $L > W$ , because of a restriction of the area spanned by quasiparticle paths that connect the two superconductors, effectively reducing the area of the junction [30, 31]. However, our device geometry is not in this regime, since the calculated SQI patterns, using our device parameters, do not show an even-odd effect without superficially adding an offset (Fig. 7.2). Thirdly, an Andreev pair of which one quasiparticle encircles the junction area could cause an even-odd SQI pattern. This process, called crossed Andreev reflection (CAR), either directly or by interference of two different CAR trajectories, results in a flux independent supercurrent [151, 165]. To find out whether a central current path, or crossed Andreev reflection causes the even-odd effect, we study gate dependent SQI measurements and investigate other devices in the remainder of the chapter.

## 7.4. GATE DEPENDENCE

In order to obtain an understanding of the gating effect on a regular SQI pattern, we consider the gate dependence of device I. The periodicity of the SQI patterns in Fig. 7.3a first grows slightly from  $1.3\Phi_0$  to  $1.5\Phi_0$  as  $V_{BG}$  is lowered from 30 V to 1.2 V (see dashed red line). Note that as  $V_{BG}$  is reduced, the mobility  $\mu$  and  $l_{MFP}$  decrease, as extracted from a Hall bar measurement in Fig. 7.3b (for details see Fig. 7.S4). For  $V_{BG} < 3$  V the length  $L$  of the device is larger than  $l_{MFP}$  and we expect to enter the diffusive transport regime. In Fig. 7.3c, calculated SQI traces for ballistic and diffusive transport (section 7.8.1), show that the latter has both a smaller periodicity and lower side lobe amplitudes than the

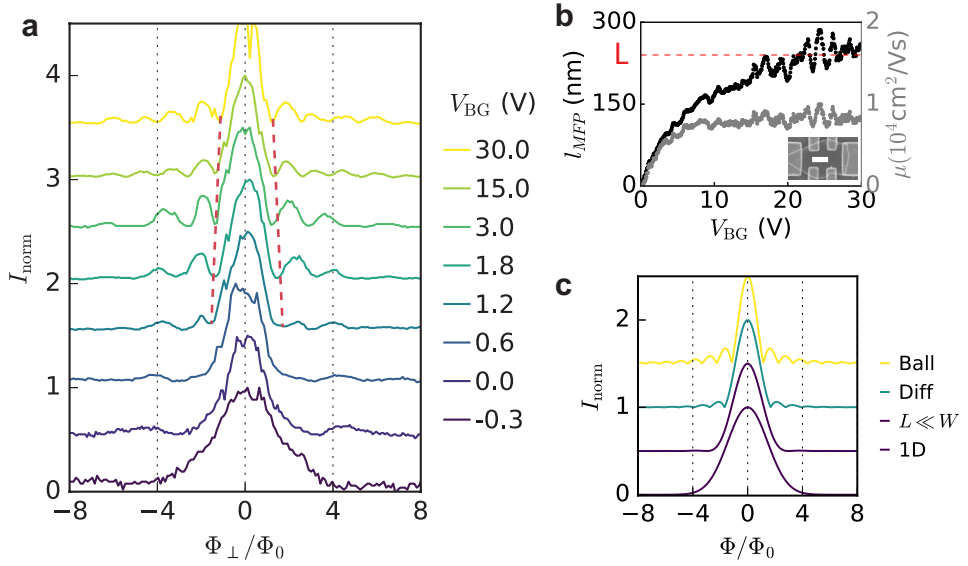


Figure 7.3: **Gate dependence of the Fraunhofer SQI pattern.** **a** Normalized switching current  $I_{\text{norm}}$  as a function of normalized flux  $\Phi_{\perp}/\Phi_0$  for the indicated bottom gate voltages  $V_{\text{BG}}$ . The dashed red lines highlight an increase in periodicity as  $V_{\text{BG}}$  is reduced. **b** Mean free path  $L_{\text{MFP}}$  and mobility  $\mu$  as a function of  $V_{\text{BG}}$ , extracted from Hall measurements (for details see Fig. 7.5.4). A SEM image of the Hall bar device is provided in the inset, with a scale bar representing 500 nm. The length  $L$  of device I is indicated by the dashed red line for comparison. **c** Theoretical predictions of SQI patterns. The ballistic (Ball), diffusive (Diff) and quasi one-dimensional ( $L \gg W$ ) are obtained from Ref. 31, and the one-dimensional (1D) case from Ref. 166. The expressions and input parameters of all curves are presented in section 7.8.1.

7

first. To conclude, reducing the gate voltage changes the transport regime of the JJ from ballistic to diffusive.

However, the model does not capture the strong increase of the periodicity, and suppression of the side lobe amplitudes for gate voltages below  $V_{\text{BG}} = 1.2 \text{ V}$ . Such a monotonically decaying switching current is reported before in case of a narrow JJ, either diffusive [166, 167] or ballistic [168, 169]. We fabricated several devices with different  $L$  and  $W$ , and find that an  $L/W$  ratio of 0.17 results in such a decay for a diffusive JJ (Fig. 7.S5). The theoretical SQI patterns in the limit of  $L \gg W$  [31], and by considering a one-dimensional diffusive (1D) JJ [166], are plotted in Fig. 7.3c. These patterns both resemble the measured SQI pattern at  $V_{\text{BG}} = -0.3 \text{ V}$  well. Remember that we expect electron accumulation at a single edge in device I, because it has crystal direction 110 (Fig. 7.2b). Therefore, we conclude that a (quasi) 1D diffusive edge channel is observed at reduced gate voltages in device I.

The even-odd SQI pattern from device II changes drastically as a function of gate voltage (Fig. 7.4a). The first side lobe disappears as  $V_{\text{BG}}$  is reduced (highlighted by the red arrows), and becomes zero at  $V_{\text{BG}} = 3 \text{ V}$ , because the amplitude of the first lobe decreases below the offset  $f$  of the SQI pattern. For the third lobe similarly, the offset it is larger than the amplitude for all gate voltages. Then, for the bottom two traces of

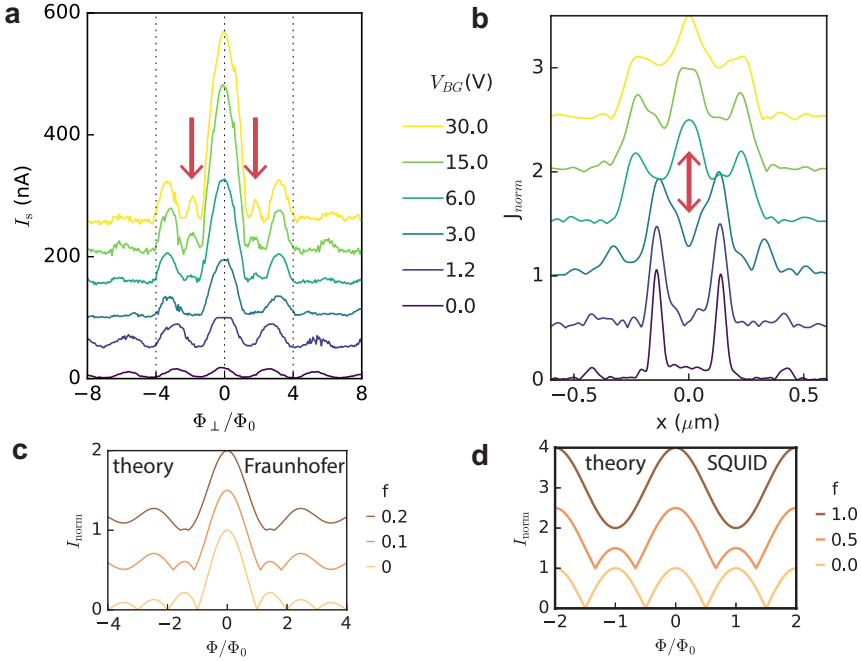


Figure 7.4: **Gate dependence of even-odd SQI pattern.** **a** Switching current  $I_s$  as a function of normalized perpendicular magnetic flux  $\Phi_{\perp}/\Phi_0$  for device II at the indicated gate voltages  $V_{BG}$ . The red arrows highlight the first lobe, which amplitude is diminished as  $V_{BG}$  decreases. **b** Normalized current density distributions  $J_{norm}$  extracted from the SQI patterns from **a**. The disappearance of the central peak is highlighted by the red arrow. **c,d** Calculated SQI patterns with a variable offset  $f$ , in case of an ideal Fraunhofer and SQUID pattern (section 7.8.1), respectively. Both show a change in periodicity once the offset becomes larger than the oscillation amplitude.

Fig. 7.4a, the SQI pattern takes a cosinusoidal shape, which is known as a superconducting quantum interference device (SQUID) pattern [21]. The smooth oscillation, without cusps, highlights that the offset remains larger than the amplitude and the pattern. For clarity and comparison we added examples of basic Fraunhofer and SQUID patterns with different offsets in Fig. 7.4c-d.

The SQUID pattern translates to a current density distribution with edge conduction only (bottom trace of Fig. 7.4b). This is in agreement with device II having two parallel edges with crystal direction 110, where we expect electron accumulation (Fig. 7.2a). The enhanced edge conduction at both sides of the JJ opens the possibility for CAR. For example, the Cooper pair becomes flux independent, once its two quasiparticles travel over a different edge [151, 160]. This suggests that CAR is causing the even-odd effect in the JJ.

Because the offset influences not only the amplitude but also the appearance of the side lobes, the periodicity of the SQI pattern changes as the gate voltage is reduced. The periodicity doubles from  $1.3\Phi_0$  at  $V_{BG} = 15\text{V}$  to  $2.7\Phi_0$  at and below  $V_{BG} = 3\text{V}$ . The SQI pattern thus becomes entirely  $h/e$  periodic in magnetic flux, the offset is larger than

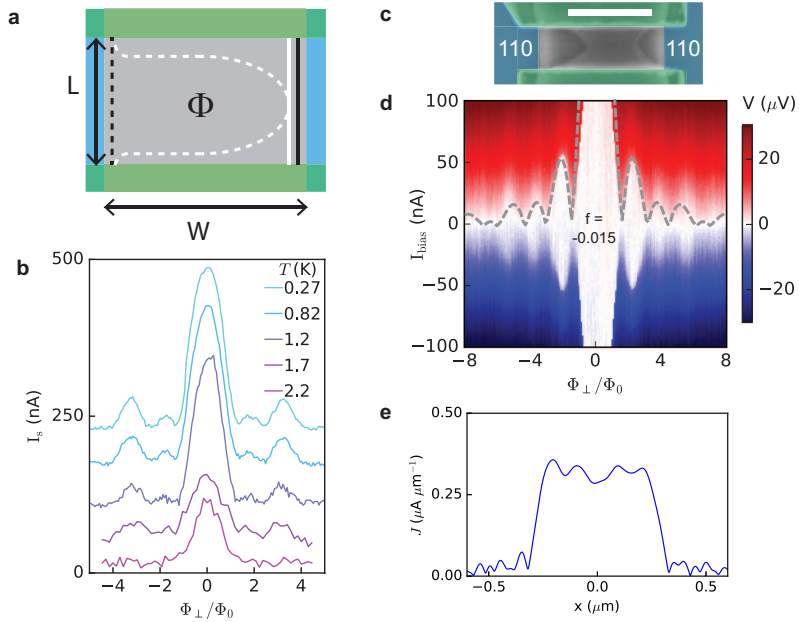


Figure 7.5: **Crossed Andreev reflection.** **a** The dashed (solid) line schematically represents a crossed (normal) Andreev reflection. The electron (white) encircles the junction, and picks up a phase due to flux  $\Phi$ , while the hole (black) flows along the opposite edge. **b** Temperature dependence of the SQI pattern of device II at  $V_{BG} = 15$  V. **c** SEM image of device III. The nanowire (grey) is deposited on a Si/SiO substrate (blue) and contacted by NbTiN (green). The scale bar represents 500 nm. **d** Voltage measured over device III as a function of current bias ( $I_{\text{bias}}$ ) and normalized perpendicular magnetic flux ( $\Phi_{\perp}/\Phi_0$ ), at a bottom gate voltage ( $V_{BG}$ ) of 15 V. The dashed grey line is a simulation following eq. 7.S3 [31] with offset  $f = -0.015$ , where we used device parameters as noted in section 7.8.1. **e** Current density distribution  $J$  extracted from the SQI pattern of **b**, using the Dynes-Fulton approach [27].

the amplitude of the SQUID pattern (see also Fig. 7.4d). This is different from the observed  $h/e$  SQUID in chapter 6, where the amplitude is larger than the offset and an  $h/2e$  background is observed at the same time. Our observation confirms that the  $h/e$  periodicity is not a unique signature of a topological JJ [160].

The doubling of the periodicity is also reflected in the extracted current density distributions in Fig. 7.4b. At  $V_{BG} = 3$  V, the current density profile is spanning half the width of the junction only, compared to  $V_{BG} = 6$  V. This is an artifact of the Dynes-Fulton approach, since the same area (and thus flux periodicity) is used for the calculation of all traces. Apart from the reduced width, the central peak in the current density suddenly disappears, which is very unlikely to be caused by the altered global bottom gate voltage. Also, the offset in the SQI patterns persists, while there is no current path at the center anymore. Therefore, we disregard a current path at the center of the JJ as an explanation for the even-odd effect.

## 7.5. TEMPERATURE DEPENDENCE

To further investigate CAR, we consider the length of the process and its dependence on temperature. For a quasiparticle to encircle the junction and pair up again, the superconducting coherence length should be in the order of the trajectory (Fig. 7.5a). We estimate the superconducting coherence length at  $V_{BG} = 15\text{ V}$  to  $1\ \mu\text{m}$ , which is smaller, but at the same order as the typical junction circumference of  $2(L + W) \sim 2\ \mu\text{m}$ . Because this circumference is smaller than  $L$ , we expect the CAR (even-odd effect) to disappear as a function of temperature before the normal Andreev reflection (Fraunhofer pattern) is suppressed. A temperature dependent measurement of the SQI of device II is however ambiguous, because the side lobes (and with that the even-odd effect) diminishes before the switching current is suppressed (Fig. 7.5b). The length consideration and temperature dependence neither support nor contradict the occurrence of CAR in the JJ.

## 7.6. ODD-EVEN EFFECT

Two other devices (III and VI) also reveal an even-odd SQI pattern, and show enhanced edge conduction in their parallel edges with a 110 crystal direction (Fig. 7.S6 and Fig. 7.S1). Additionally, other devices, without parallel edges, do not show an even-odd SQI pattern (Fig. 7.S5). For device VI, the offset  $f$  has a positive sign (Fig. 7.S6), similar to device II. However, the SQI pattern from device III in Fig. 7.5d shows a negative offset, or odd-even effect, where the third lobe is larger than the second lobe.<sup>1</sup> By adding a negative offset to the calculated SQI pattern (eq. 7.S3 [31]), we, again, find good agreement with the measured pattern. Also, the offset leads to a small reduction of the current density around zero in Fig. 7.5e, as we expected. Having either a positive or negative offset to the switching current due to CAR depends on microscopic details regarding the spin mixing in the JJ [151]. To be more precise, spin mixing with predominantly spin conserving or spin-flip processes, refer to a positive or negative offset, respectively. In our InSb flakes, the spin mixing is probably caused by the strong spin-orbit interaction. The observation of a negative offset is, to our knowledge, unique to CAR [151], and therefore strongly supports that CAR is causing the even-odd effect.

## 7.7. CONCLUSION

In conclusion, we observe an even-odd effect in the SQI patterns of InSb flake Josephson junctions, that is caused by crossed Andreev reflection. The crossed Andreev reflection exclusively takes place in samples where both edges show enhanced conduction. We identified the crystal axis (110) of the conductive edges, and can thus in the future choose to either study or circumvent them. Identifying the microscopic origin of sign of the even-odd effect would be an interesting next step for theoretical and experimental study.

<sup>1</sup>Such an odd-even pattern, or negative offset, cannot be caused by a restriction of the paths through a finite size junction [30, 31], ruling out that hypothesis for the second time.



## 7.8. SUPPLEMENTARY MATERIAL

### 7.8.1. SQI THEORY MODELS

#### BASICS

The expression for a basic Fraunhofer and SQUID interference patterns are given by [21]:

$$I_c = I_{c,0} \left| \frac{\sin(\pi\Phi/\Phi_0)}{\pi\Phi/\Phi_0} \right|, \quad (7.S1)$$

and

$$I_c = I_{c,0} |\cos(\pi\Phi/\Phi_0)|, \quad (7.S2)$$

where  $I_{c,(0)}$  is the critical current (at zero flux),  $\Phi$  is the magnetic flux applied and  $\Phi_0$  the flux quantum of  $h/2e$ .

#### BARZYKIN *et al.*

The superconducting quantum interference in a JJ with a finite length  $L$  and width  $W$  is described in the model. The final expressions for the critical current as a function of magnetic flux pattern in a ballistic JJ ( $I_{c,\text{ball}}$ ) and diffusive JJ ( $I_{c,\text{diff}}$ ) are [31]:

$$I_{c,\text{ball}}(\Phi) = \max_{0 \leq \phi \leq 2\pi} \frac{2e v_F}{\pi W \lambda_F L} \iint_{-W/2}^{W/2} \frac{dx_1 dx_2}{\left[1 + \left(\frac{x_1 - x_2}{L}\right)^2\right]^{3/2}} \sum_{k=1}^{\infty} (-1)^{k+1} \frac{L}{\xi_T \cos \theta_{x_1 - x_2}} \frac{\sin k \left(\frac{\pi\Phi}{W\Phi_0} (x_1 + x_2) + \phi\right)}{\sinh \frac{kL}{\xi_T \cos \theta_{x_1 - x_2}}} \quad (7.S3)$$

$$I_{c,\text{diff}}(\Phi) \propto f_{\text{diff}}(\nu) = \sum_{l=-\infty}^{\infty} (-1)^l S_l(L/2) \frac{d}{du} S_l(u) \Big|_{u=L/2} \left( \frac{\sin \pi(\nu+l)/2}{\pi(\nu+l)/2} - (-1)^l \frac{\sin \pi(\nu-l)/2}{\pi(\nu-l)/2} \right)^2, \quad (7.S4)$$

$$S_l(u) = \sqrt{|u|/2\pi} (q_T^2 + \pi^2 l^2 / W^2)^{1/4} K_{1/2} \left( \sqrt{u^2 (q_T^2 + \pi^2 l^2 / W^2)} \right)$$

where,  $\phi$  the superconducting phase difference,  $v_F$  and  $\lambda_F$  the Fermi velocity and wavelength,  $\xi_T$  the normal metal coherence length ( $\hbar v_F / 2\pi k_B T$ ),  $\theta_{x_1 - x_2} = \arctan(x_2 - x_1) / L$  is the angle of the Andreev reflection with respect to the normal of the contact.  $K_{1/2}$  is a modified Bessel equation and  $q_T = 1/\xi_T^2$  where  $\tilde{\xi}_T$  is the diffusive coherence length. The SQI pattern in the limit of  $L \ll W$  for a diffusive JJ (plotted in Fig. 7.3) is [31]:

$$f_{\text{diff}}(\nu) = \frac{\cos^2 \pi\nu/2}{(1 - \nu^2)^2}. \quad (7.S5)$$

The geometrical parameters used for the different devices, can be found in table 7.S1. Furthermore, we use an effective mass of 0.02 [170] and a temperature of 300 mK (or 50 mK) to extract parameters from the Hall bar measurement (Fig. 7.S4). For the calculated SQI patterns in Fig. 7.2c,d and Fig. 7.5a, at  $V_{\text{BG}} = 15$  V, we find  $v_F = 2.5 \cdot 10^6$  m/s,  $\lambda_F = 2.3$  nm, and  $\xi_T = 10$   $\mu\text{m}$ ; and for Fig. 7.3c, at  $V_{\text{BG}} = 3$  V,  $v_F = 1.5 \cdot 10^6$  m/s,  $\lambda_F = 4.0$  nm, and  $\xi_T = 5.9$   $\mu\text{m}$ . Because the devices are in the crossover regime from ballistic to diffusive

transport, we use the ballistic coherence length as diffusive coherence length, so we set  $\tilde{\xi}_T = \xi_T$ . With a transmission value of  $T \leq 0.6$  we expect to have a sinusoidal current phase relation [147], and therefore only use  $k = 1$  for eq. 7.S3. For eq. 7.S4 we sum up to  $l = 100$ . For both we checked that the periodicity does not change for summing over a larger integer. In all figures in the main text we plot the normalized critical current,  $I_c(\Phi)/I_c(0)$  or normalized functional form,  $f_{\text{diff}}(\Phi)/f_{\text{diff}}(0)$ .

### 1D DIFFUSIVE LIMIT

For a one-dimensional system in the diffusive limit, the critical current decays monotonically [166]:

$$I_c(\Phi) \propto f = e^{-0.238\Phi^2}, \quad (7.S6)$$

which is used in Fig. 7.3.

### 7.8.2. DEVICE GEOMETRIES

Device	I	II	III	IV	V	VI	VII
$W$ (nm)	1280	770	855	1360	970	790	1150
$L$ (nm)	240	240	185	205	465	425	670
$L/W$	0.19	0.31	0.22	0.15	0.48	0.54	0.58
$A_{\perp}$ ( $\mu\text{m}^2$ )	0.31	0.18	0.16	0.28	0.45	0.34	0.77
$A_{\perp \text{ eff}}$ ( $\mu\text{m}^2$ )	0.74	0.63	0.95	1.37	0.81	1.21	1.03

Table 7.S1: **Geometry parameters for all 7 devices.** The width  $W$  and length  $L$  obtained from the SEM images. The areas  $A$  for perpendicular magnetic field, where the effective area includes flux focusing due to the Meissner effect.

### 7.8.3. SUPPLEMENTARY FIGURES

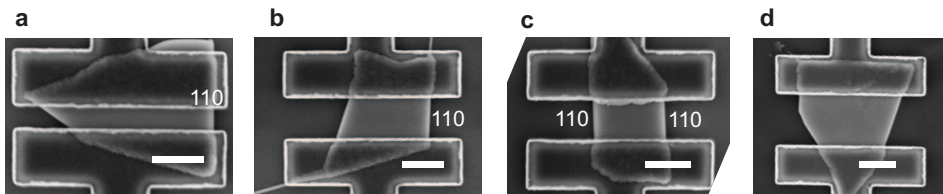


Figure 7.S1: **SEM images of device IV-VII (a-f).** All images do not show underetching from the sulfur solution. Note that device VII in c has parallel edges, both in the same crystal direction (110). The scale bar represents 500 nm.

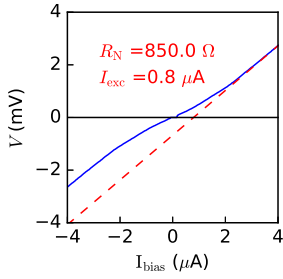


Figure 7.S2: **Estimation of the transmission of device I.** Voltage measured  $V$  of Device I as a function of current bias  $I_{\text{bias}}$  at  $V_{\text{BG}} = 2.4\text{V}$ . The excess current  $I_{\text{exc}}$  and normal state resistance  $R_{\text{N}}$  are extracted and used to estimate a transmission of 0.6, with the theory described in Ref. 145.

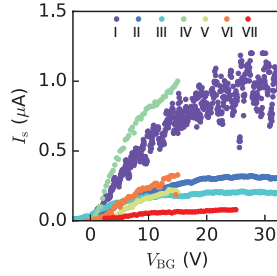


Figure 7.S3: **Switching current  $I_s$  as a function of bottom gate voltage  $V_{\text{BG}}$  for all devices.** In all devices the supercurrent is pinched completely at a  $V_{\text{BG}} = -3\text{V}$ .

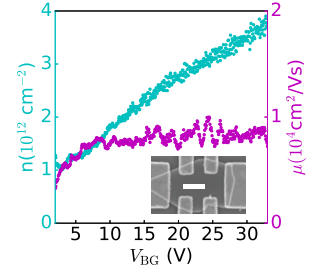


Figure 7.S4: **Electron density and mobility.** Hall bar measurements are used to extract the density  $n$  and mobility  $\mu$  as a function of bottom gate voltage  $V_{\text{BG}}$ . The Hall bar device (inset) has Cr/Au contacts, and the scale bar represents 500 nm.

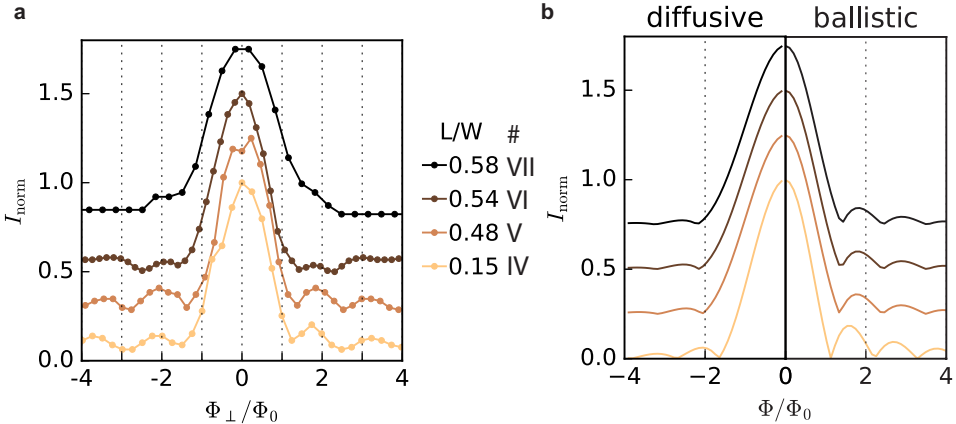


Figure 7.S5: **SQI patterns for devices IV-VII.** **a** Normalized switching current  $I_{\text{norm}}$  as a function of normalized out-of-plane magnetic flux  $\Phi_{\perp}/\Phi_0$ . The SQI patterns for the 4 devices with contact separation  $L$  and length width ratio  $L/W$  as indicated. The measurement is performed at  $V_{\text{BG}} = 15\text{V}$ , except for device IV ( $V_{\text{BG}} = 4.5\text{V}$ ) and VII ( $V_{\text{BG}} = 25\text{V}$ ). All measurements are done at a temperature of 50 mK. An even-odd SQI pattern is observed for device VI, see also Fig. 7.S6. The SQI pattern of device VII has no oscillations, but a monotonic decay instead. **b** Calculated normalized SQI patterns for the diffusive, left, and ballistic, right, models of Barzykin *et al.* [31]. The parameters used are presented in section 7.8.1. We observe that devices IV-VI are best resembled by the ballistic model, with a periodicity at or below  $1.5\Phi_0$ . Device VII however is diffusive, which is in accordance with its length of 670 nm being longer than the mean free path of 250 nm.

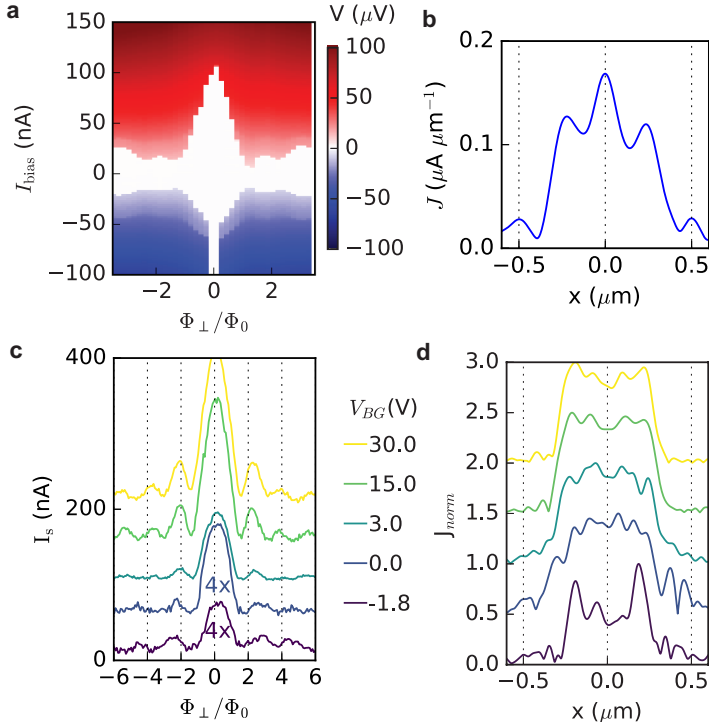


Figure 7.S6: **Even-odd SQI pattern of device VI and enhanced edge conduction in device III.** **a** Measured voltage  $V$  as a function of current bias  $I_{\text{bias}}$  and normalized out-of-plane flux  $\Phi_{\perp}/\Phi_0$  of device III. An even-odd pattern is observed, because the second lobe is larger than the first. This measurement is performed at a temperature of 50 mK. **b** Normalized current density distribution  $J_{\text{norm}}$  calculated from the pattern in **a**. The even-odd effect is represented in the central peak in the  $J$ . **c** Switching current  $I_s$  of device III as a function of normalized out-of-plane flux  $\Phi_{\perp}/\Phi_0$  at the indicated gate voltages. The bottom two traces are multiplied by 4 for visibility. **d** Normalized current density distribution  $J_{\text{norm}}$  calculated from the patterns in **a**. At  $V_{BG} = -1.8$  V the enhanced edge conduction shows up.



# 8

## PHASE BIASING INAs JOSEPHSON JUNCTIONS

*A Josephson junction (JJ) made from a two-dimensional electron gas (2DEG) with strong spin-orbit interaction is predicted to enter the topological regime once a sufficient in-plane magnetic field is applied. The superconducting phase difference over the JJ in the topological regime self tunes to value close to  $\pi$ . Controlling this phase difference enables one to switch the junction from the topological to the trivial regime and vice versa. In this chapter we study superconducting phase control in an InAs JJ with a planar geometry. We measure the oscillations of a superconducting quantum interference device (SQUID) under influence of an in-plane magnetic field, and look for  $0-\pi$ -transition induced by the Zeeman effect.*

---

In collaboration with Eric Leerssen, Sergei Gronin, Geoff Gardner, Candice Thomas, Michael J. Manfra, Leo P. Kouwenhoven and Srijit Goswami.

## 8.1. INTRODUCTION

Two recent theoretical works describe how to reach a topological regime in a planar JJ in a 2DEG with spin-orbit interaction [171, 172]. In the limit where the spin-orbit energy at the Fermi level and the superconducting gap are larger than the Zeeman energy ( $\Delta_{\text{SO}}, \Delta > E_Z$ ), the JJ is trivial or topological depending on whether its free energy minimum is at 0 or at  $\pi$  phase difference, respectively. The superconducting phase difference can thus be used to tune the device in and out of the topological regime. It is encouraging that the first experimental evidence for this is reported recently [173, 174].

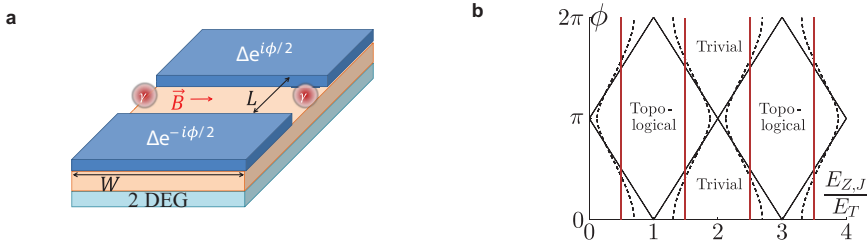


Figure 8.1: **Planar Josephson junction and its phase diagram.** **a** Schematic of a planar JJ. The two-dimensional electron gas (2DEG) is contacted by two superconducting electrodes (dark blue) that have a superconducting gap  $\Delta$  and phase  $\phi$ . The junction has width  $W$  and length  $L$ , and the magnetic field is applied in the plane of the junction perpendicular to the direction of the supercurrent. If the junction is in the topological regime, Majorana's ( $\gamma$ 's) show up at its edges. **b** Phase diagram of the JJ as a function of the ratio of Zeeman energy  $E_{Z,J}$  and Thouless energy  $E_T$  in the junction, and the superconducting phase difference  $\phi$ . The solid black line denotes the phase boundaries for a contact transparency of  $\tau = 1$ , the dashed black line for  $\tau = 0.75$ , and the solid red line for  $\tau \ll 1$ , respectively. Both figures are adapted from Ref. 171.

In order to obtain a  $\pi$ -junction, a magnetic field is applied that induces magnetic ordering in the system via the Zeeman effect [36, 37]. Without phase control, the junction will equilibrate its phase difference according to the energy minimum of the Josephson energy, and the phase diagram of the device (Fig. 8.1a) is indicated by the red solid lines in Fig. 8.1b. The device undergoes a  $0 - \pi$ -transition as the Zeeman energy  $E_Z$  exceeds half of the Thouless energy  $E_T$ , and the opposite transition,  $\pi$  to 0, at  $E_Z/E_T = 3/2$ , and repeats as long as  $E_Z < \Delta$  (section 2.2.3) [38, 39]. The Zeeman energy  $E_Z = g\mu_B B$ , where the Landé  $g$ -factor is a material constant, can be altered with the magnetic field  $B$  [43]. The Thouless energy  $E_T = \pi\hbar v_F/2L$ , depends on the distance  $L$  between the superconducting contacts and the Fermi velocity  $v_F$  in the semiconductor.

Additionally, the superconducting phase difference ( $\phi$ ) can be controlled by threading a magnetic flux through a loop geometry (section 8.7.1) [175]. In case of perfect transparency  $\tau$  of the junction, all reflections are Andreev reflections, and the phase diagram changes into a repeated diamond shape (Fig. 8.1b). At  $\phi = \pi$  the device enters the topological field for smaller magnetic fields, compared to the case without control over the superconducting phase. This is an advantage because an increased magnetic field generally reduces the superconducting gap, and could lead to unwanted orbital or interference effects. For imperfect SN interfaces ( $\tau \sim 0.75$ ), the diamonds are elongated (dashed black line in Fig. 8.1b) due to normal reflections, that make the Andreev states less sensitive to  $\phi$ . When normal reflection dominates, or  $\tau \ll 1$ , the Andreev states loose

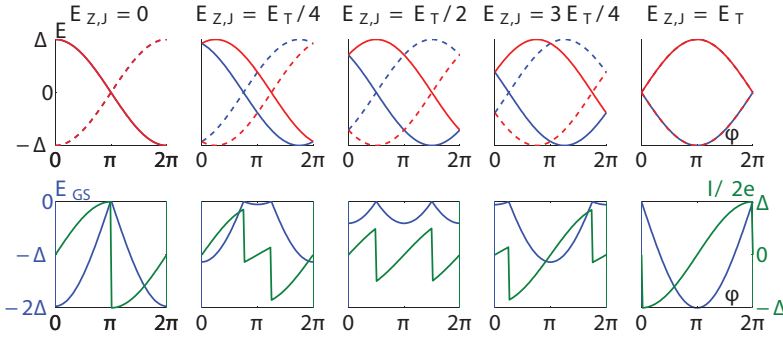


Figure 8.2: **Andreev state and current phase relation as a function of magnetic field.** The top row shows the Andreev state energy with transmission  $T = 1$  as function of superconducting phase  $\phi$ . The dashed and solid lines indicate different parity and red and blue denote a different spin. In the bottom row the ground state energy  $E_{GS}$  (blue) and CPR  $I/2e$  (green) of the JJ are shown. This figure is taken from Ref. 171.

their phase dependence, resulting in the striped phase diagram, as sketched with the solid red lines in Fig. 8.1b.

The phase diagram can be obtained by measuring the current phase relation (CPR) of the JJ while changing the in-plane magnetic field. A calculation of the Andreev state energies and CPR, done in Ref. 171, is presented in Fig. 8.2. They consider the narrow junction limit (where a single Andreev bound state is present in the junction), unity transmission and zero temperature. The ground state energy of JJ develops a local minimum around  $\phi = \pi$  as the Zeeman energy is increased, which reflects as a kink in the CPR. At the  $0 - \pi$ -transition ( $E_{Z,J} = E_T/2$ ) the  $\sin(\phi)$  the switching current  $[\max I/2e(\phi)]$  has a minimum. In an experimental situation the transmission is imperfect due to limited transparency of the contacts. Therefore, the CPR is expected to be less skewed [147], comparable to the effect of a non zero temperature [176, 177]. However, even in the limit of sinusoidal CPR, the  $\pi$ -state should show up as a dip in the ground state energy and a kink the CPR of the JJ [178, 179].

## 8.2. EXPERIMENTAL SETUP

The device consists of a DC SQUID, a superconducting loop that is intersected by two JJs (Fig. 8.3a). The SQUID is fabricated in an InAs quantum well with 7 nm of epitaxial aluminium (Al) on top (Fig. 8.S2). The defect and oxide free interface between the semiconductor and superconductor results in high quality superconducting contacts with transparencies between 0.7 and 1.0 [69, 84]. Furthermore, InAs 2DEGs are known for their strong SOI and large Landé  $g$ -factor [67, 103, 180, 181]. To fabricate the device we first etch the loop mesa with two wet chemical etches, then the junctions are defined by selectively etching the Al only. The JJs are  $5 \mu\text{m}$  wide and have a length of 0.2 and  $1.5 \mu\text{m}$ , for the reference and device JJ, respectively. Finally a global  $\text{AlO}_x$  dielectric is grown by atomic layer deposition, and top gates are deposited on the JJs. These top gates can be used to pinch off the supercurrent, which allows us to study the single junctions separately.



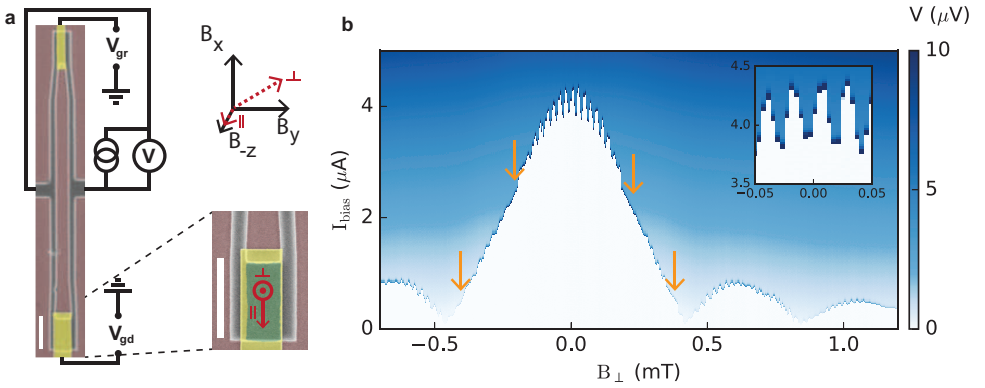


**Figure 8.3: DC SQUID device and magnetic field characterization.** **a** Scanning electron microscope image of the DC SQUID, and zoom in on one of the JJ with a scale bar of  $5 \mu\text{m}$ . The false coloring represents the different materials, gray is aluminium (Al) red is etched mesa, green uncovered mesa and gold is the top gate metal. The four terminal current bias measurement setup is schematically drawn. The black axes indicate the magnetic field directions of the vector magnet setup, and the red axes the directions perpendicular and parallel to the substrate (as in Fig. 8.1a). **b** A magnetic field applied perpendicular to the loop reveals SQUID oscillations (inset) on top of a Fraunhofer envelope. The SQUID oscillations are suppressed periodically (see the orange arrows).

The DC SQUID is measured in a four terminal current bias setup (Fig. 8.3a). A vector magnet is used to apply a field perpendicular ( $B_{\perp}$ ) and in the plane of the SQUID perpendicular to the current flow ( $B_{\parallel}$ ). The  $x$ - and  $y$ -axis of the magnet ( $B_x$  and  $B_y$ ) have a roughly  $30^\circ$  and  $60^\circ$  angle to  $B_{\perp}$ , respectively (Fig. 8.3b). A high resolution but small range current source controls  $B_y$ , and with that  $B_{\perp}$ . The magnet  $z$ -axis ( $B_z$ ) has a  $\sim 1^\circ$  offset from  $B_{\parallel}$ , of which the resulting unwanted  $B_{\perp}$  component is compensated with  $B_x$ . This compensation results in a magnetic field of the order of 10 mT, in-plane and parallel to the current flow, that does not have a relevant effect on the interference pattern of the reference junction (Fig. 8.54).

The switching current as a function of  $B_{\perp}$  (Fig. 8.3b) reveals three different oscillation periodicities. Firstly, the Fraunhofer envelope of the switching current corresponds to an area of  $2.2 \mu\text{m}^2$ , consistent with the sum of the area of the reference JJ and the flux focusing due to the Meissner effect. Secondly, the SQUID oscillations on top of the envelope have a periodicity of  $27 \mu\text{T}$  (inset in Fig. 8.3b), corresponding to an area of  $77 \mu\text{m}^2$ , close to the lithographic size of the loop of  $\sim 90 \mu\text{m}^2$ . From the SQUID pattern, we read off the switching currents for the reference junction  $I_{s,\text{ref}} = 4 \mu\text{A}$  and for the device junction  $I_{s,\text{dev}} = 300 \text{ nA}$ . Thirdly, the SQUID oscillation damps out at the points highlighted by the orange arrows in Fig. 8.3b. This is indicative of the Fraunhofer of the device junction, which has an estimated area is  $6.7 \mu\text{m}^2$ , slightly less than we expect from the geometry ( $7.5 \mu\text{m}$ ).

### 8.3. CURRENT PHASE RELATION MEASUREMENT PREREQUISITES

In order to measure the CPR in a DC SQUID, the superconducting phase difference should drop entirely over the device junction. In other words, the phase difference of the

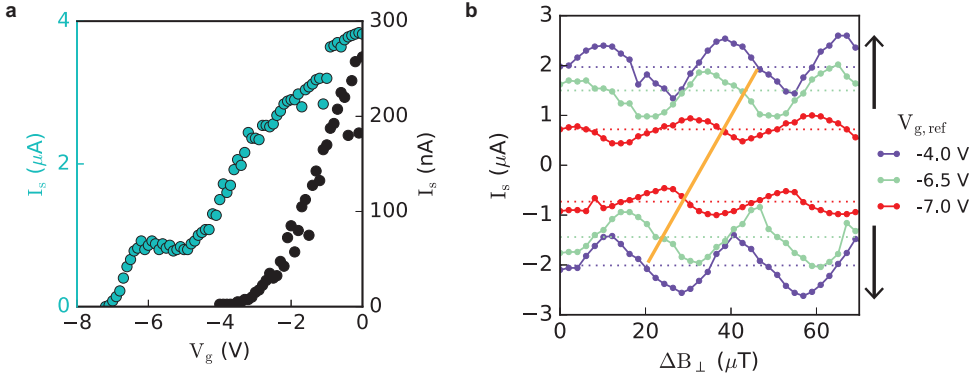


Figure 8.4: **Switching current asymmetry and SQUID inductance.** **a** The switching current  $I_s$  is suppressed as the gate voltage  $V_g$  of the reference and device junctions (magenta and black, respectively) is decreased. **b**  $I_s$  as function of perpendicular magnetic field for different asymmetries, induced by changing  $V_{g,\text{ref}}$ . The current is swept from zero in positive or negative direction as indicated by the arrows. The solid orange line highlights the flux shift of the oscillations due to inductance.

reference junction ( $\phi_{\text{ref}}$ ) should be constant [175, 182]. Strictly speaking this is the case if  $I_{c,\text{dev}} \ll I_{c,\text{ref}}$  (see also section 8.7.1). However, for a sinusoidal CPR,  $I_{c,\text{ref}}$  is not changing strongly for a small shift in  $\phi_{\text{ref}}$ , since a sine is flat up to the first order around  $\pi/2$ . Therefore, we loosen the constraint and aim for a switching current ratio ( $I_{s,\text{ref}}/I_{s,\text{dev}}$ ) of 10.

Additionally, to ensure the mapping from the applied flux to the superconducting phase is correct, we consider the inductance in the SQUID loop. We suppose the inductance of the two arms to be equal because they have an identical geometry (Fig. 8.3a). An inductance of  $L = \Delta\Phi/\Delta I_s = 0.48 \text{ nH}$  is extracted from the measured flux shift  $\Phi_T$  as a function of switching current  $I_s$  at different gate voltages  $V_{g,\text{ref}}$  (Fig. 8.4b). This inductance translates to a screening parameter  $\beta_L (LI_{\text{max}}/\Phi_0)$  of 1. With this screening, the minima in the SQUID oscillation are lifted slightly (Fig. 8.S1a)[175]. Also, the combination of a skewed CPR and a large phase shift could lead to a distortion of the measured oscillation due to reentrant behavior of the switching current [183]. For a switching current of 280 nA,  $\beta_L$  decreases to 0.1 and both the lifted minima and distorted shape are suppressed. In summary, the measured SQUID pattern represents the CPR as long as  $I_{s,\text{ref}}/I_{s,\text{dev}} \sim 10$  and  $I_{s,\text{ref}} \leq 300 \text{ nA}$ .

## 8.4. CPR IN AN IN-PLANE MAGNETIC FIELD

First, we consider a resistance measurement of the SQUID oscillation, which could reveal a global  $0$  to  $\pi$  phase shift of the CPR. Instead of sweeping the bias current, the voltage response at a constant current bias is measured, in order to explore the magnetic field parameter space efficiently. The voltage oscillations extend far above the switching current (Fig. 8.5a), so the approach is viable. An in-plane versus out-of-plane magnetic field sweep is plotted in Fig. 8.5b for a constant current bias of 250 nA, and in Fig. 8.5c for 350 nA. At  $B_{\parallel}$  between 0 T and -0.2 T, we observe the central and first sidelobes of

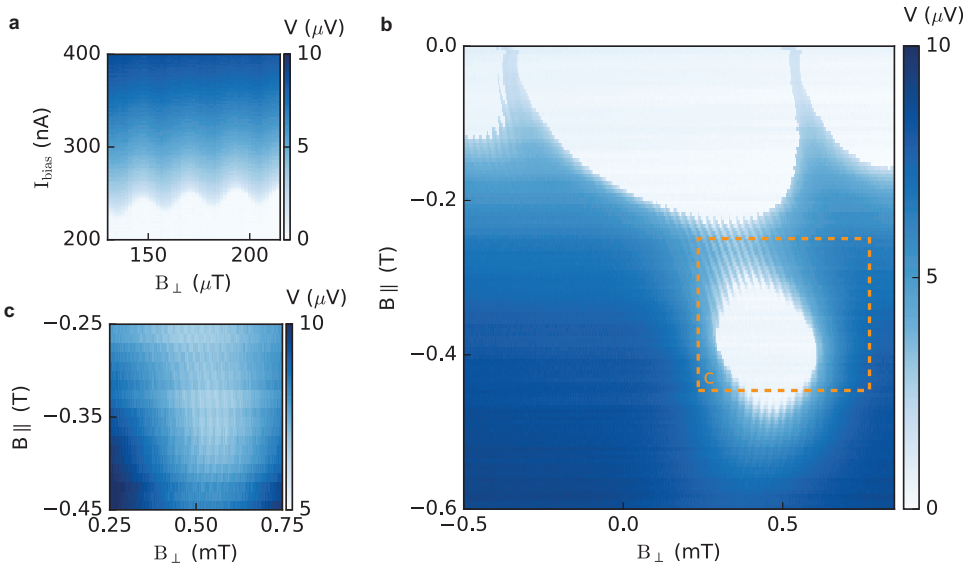


Figure 8.5: **SQUID oscillations in an in-plane magnetic field.** **a** A current bias  $I_{\text{bias}}$  versus perpendicular magnetic field  $B_{\perp}$  scan of the SQUID oscillations at an in-plane magnetic field  $B_{\parallel}$  of  $-0.3$  T. The switching current  $I_s$  is oscillating with a period of  $28 \mu\text{T}$ . This oscillation is resembled by the measured voltage at larger  $I_{\text{bias}}$ . **b** A voltage measurement at a constant  $I_{\text{bias}}$  of  $250$  nA as a function of  $B_{\perp}$  and  $B_{\parallel}$ . The central and first lobes of the Fraunhofer pattern are observed where  $I_{\text{bias}} < I_s$ . The SQUID oscillations show up as  $I_{\text{bias}}$  is larger but close to  $I_s$ . **c** Zoom in of **b** at the indicated window, here with  $I_{\text{bias}} = 350$  nA.

the Fraunhofer envelope. Up to  $B_{\parallel} = -0.3$  T the Fraunhofer lobes and SQUID oscillations have a constant slope in the graph, which is due to imperfect compensation of the perpendicular component of  $B_z$ . However, around  $B_{\parallel} = -0.4$  T the oscillations bend. This bending is observed in the reference junction only, so we speculate it related to the geometry of the reference junction or the SQUID loop itself. At larger fields, the most prominent feature is the revival of the central Fraunhofer lobe around  $B_{\parallel} = -0.4$  T, which we study in more detail in section 8.5 and find to be solely related to the reference JJ. Focusing on the SQUID oscillations, we do not observe a robust sudden or smooth shift of  $\pi$ . Also, the resistance shows a monotonic increase, what does not correspond to a minimum in the switching current. Therefore we conclude that no global  $0-\pi$ -transition is observed.

Furthermore, to investigate the CPR itself, we measure the switching current as a function of  $B_{\perp}$  for  $B_{\parallel} = -0.2$  T to  $-0.5$  T (Fig. 8.6). Remember the signature of the onset of a  $\pi$ -junction is a kink in the CPR around  $\pi$  phase difference (Fig. 8.2). Note that we satisfy the constraints for measuring the CPR in this regime, since  $I_{s,\text{ref}}/I_{s,\text{dev}} > 10$  and the  $I_s \leq 300$  nA. The CPR does not change shape for increasing  $B_{\parallel}$ , there is no kink present in any of the measured oscillations. Furthermore, the oscillation amplitude of the switching current does not cusp but decays monotonically, confirming the behavior of the resistance in Fig. 8.5. To investigate whether reducing  $E_T$  via the Fermi velocity results in a  $0-\pi$ -transition, we measured the oscillation at a lower gate voltage for  $B_{\parallel} =$

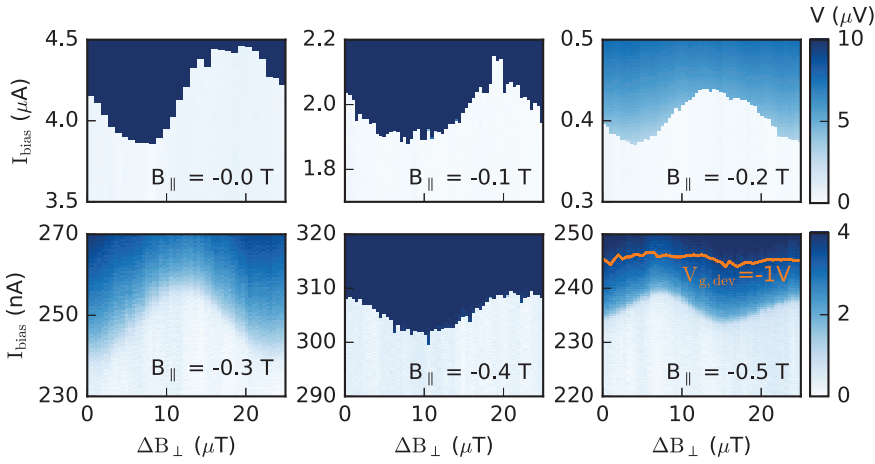


Figure 8.6: **Current phase relation at different in-plane magnetic fields.** The six panels show switching current measurements as a function of out plane magnetic field at different in-plane magnetic field values indicated. At an in-plane field of  $-0.5$  T the switching current (with  $+15$  nA offset) at a gate voltage on the device junction of  $-1$  V is shown in orange.

$-0.5$  T (orange line in panel six of Fig. 8.6). Unfortunately, the periodicity and pattern remain the same while the oscillation amplitude diminishes. In conclusion, we did not find evidence for the onset of a Zeeman induced  $\pi$ -state in the CPR of the device JJ.

$E_T$	$E_Z$ ( $g = 4$ , $B = 0.5$ T)	$\Delta_{SO}$	$\Delta$
$670 \mu\text{eV}$	$116 \mu\text{eV}$	$20 \text{ meV}$ [69]	$180 \mu\text{eV}$ [84]

Table 8.1: Estimated energy scales of the device junction.

In the following, we discuss the relevant parameters in the proposal and argue why we did not measure the  $0 - \pi$ -transition. The important energy scales are  $E_T$ ,  $E_Z$ ,  $\Delta_{SO}$  and  $\Delta$ , of which estimate values are presented in Table 8.1. An electron density of  $1.8 \cdot 10^{16} \text{ m}^{-2}$  (Fig. 8.S2), effective mass  $m_{\text{eff}} = 0.04 m_e$ [67] and  $L = 1.5$  are used. For the Zeeman effect we take a Landé  $g$ -factor of 4 [67, 184], which is measured in a quantum well similar to ours. The ratio  $E_Z/E_T$  is only 0.17 for  $B = 0.5$  T, which limits us to a small region of phase space in Fig. 8.1. Apart from that, we find  $\Delta_{SO} > E_Z$ , where  $\alpha$  is obtained via weak anti-localization measurements in a similar heterostack [69]. Additionally, the transparency plays a crucial role in the shape of the phase diagram. The dashed line in Fig. 8.1 has a larger onset value ( $E_Z/E_T$ ) for the topological phase at  $\phi = \pi$ . The combination of a small  $E_Z/E_T$  ratio and a lower transparency then expected could explain why the JJ did not reach the onset of the  $\pi$ -state up to a magnetic field of 0.5 T.

The considerations above give us an idea what to improve experimentally and investigate theoretically. Obviously, the experiment would benefit from using a material with a larger Landé  $g$ -factor (for example InSb), and a lower density, to increase the  $E_Z/E_T$  ratio. Also, the current bias measurement limits the magnetic field range, because the

switching current diminishes with magnetic field. To increase the switching current, one could work in the narrow junction regime.<sup>1</sup> Next to that, a tunneling measurement of the density of states in the junction could work up to larger magnetic fields than the current bias measurements. Recently, such tunneling measurements in the narrow junction limit were done in an InAs quantum well [174]. The authors observe a phase bias dependence of the superconducting gap at zero in-plane field, and a zero bias peak emergence around a phase difference of  $\pi$  at finite magnetic fields. However, the expected topological gap is not observed, even though they claim that the zero bias peak splits because that gap decreases. Also, it is not clear whether the zero bias peak stems from a Majorana bound state or a local Andreev bound state, that could form due to the smooth potential of their split gate tunnel probe [185, 186]. A simultaneous measurement at both sides of the junction could reveal which of the two bound states is observed. This, and other experimental ideas, are discussed in more detail in chapter 9.

## 8.5. SWITCHING CURRENT REVIVAL IN AN IN-PLANE MAGNETIC FIELD

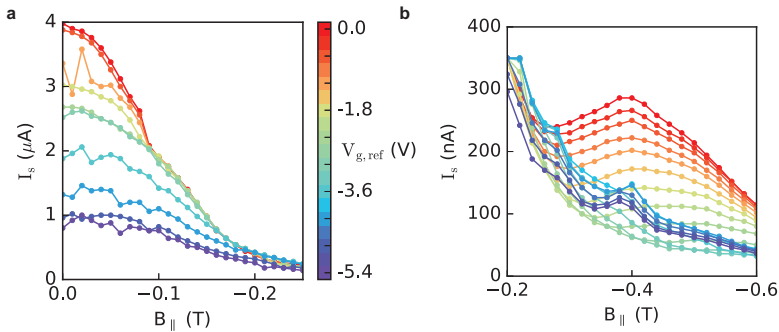


Figure 8.7: **Switching current of the reference junction in an in-plane magnetic field.** **a** Switching current from 0 T to  $-0.25$  T for  $V_{g,ref}$  0 (red) to  $-5.4$  V (purple), with a  $-0.6$  V step. **b** Switching current from  $-0.2$  T to  $-0.6$  T for  $V_{g,ref}$  0 V to  $-5.4$  V ( $-0.3$  V step).

The revival of the switching current observed in Fig. 8.5b is further investigated by measuring the reference junction only. The switching current as a function of the in-plane magnetic field, measured at zero perpendicular magnetic field (Fig. 8.S4), is presented in Fig. 8.7a-b. For zero gate voltage (red line) the same behavior as in Fig. 8.5 is observed, the switching current increases from  $B_{||} = -0.25$  T on and peaks around  $B_{||} = -0.4$  T. Interestingly, as the gate voltage  $V_{g,ref}$  is decreased, the revival disappears and from  $V_{g,ref} = -2.7$  V (dark green line) an overall decaying switching current remains. The supercurrent revival is reproduced in another device with a junction length of 250 nm (Fig. 8.S5). In a longer (500 nm) junction a monotonic decay is measured for all gate voltages (Fig. 8.S5), comparable to other experiments [70, 187].

We hypothesize that the oscillatory behavior of the switching current is caused by

<sup>1</sup>In the narrow junction regime, the phase diagram is different because  $E_T > \Delta$  [171].

an interference effect due to magnetic flux through the in-plane area of the JJ.<sup>2</sup> The estimated thickness  $d$  of the wavefunction is 20 nm (Fig. 8.S2)[69]. This together with  $L = 200$  nm corresponds to threading one flux quantum through the in-plane area at a magnetic field of 0.5 T. In a simple picture, a Fraunhofer interference pattern would occur, that depends on the geometry and the transport regime of the JJ. For a ballistic junction with  $d/L = 0.1$  a doubling of the regular Fraunhofer periodicity is expected [29, 31], where for the 1D diffusive limit a monotonic decay of the switching current remains [166, 188].<sup>3</sup> This is in qualitative agreement with the oscillations for different lengths of the junction, Fig. 8.7 and Fig. 8.S5 have ballistic and 1D diffusive patterns, respectively.

However, the oscillation in Fig. 8.7 is not a Fraunhofer pattern because the node spacing is different. We observe a node around  $-0.25$  T, and not at twice that spacing ( $-0.5$  T), where a node is expected in a Fraunhofer. Additionally, the gate dependence is different from what we expect. If reducing the gate voltage changes the pattern from ballistic (red line) to diffusive (green and blue lines), the periodicity is expected to grow before the oscillation disappears [31]. Also, a negative gate potential could squeeze the wavefunction and decrease  $d$ , what would lead to an increased periodicity. In contrast to both, we observe no change in the periodicity at all, only the magnitude of the oscillation decreases. Furthermore, the fact that the oscillation changes with gate voltage, rules out a recent suggestion that it depends on the area of the InAs covered by Al [174]. Therefore, we move on to more complex scenario.

The Hall bar measurements indicate that at zero gate voltage two subbands are occupied (Fig. 8.S2). Firstly, the supercurrent through the two modes can acquire a different phase shift and then interfere [44]. Secondly, if the wavefunctions of the two bands are spatially separated (i.e. one has more weight in the Al and the other in the InAs), the flux could induce a SQUID like interference. Such interference in the area enclosed by the Al and InAs layer is in agreement with the observed pattern, since nodes are expected at  $-0.25$  T and  $-0.75$  T. Because we observe only two nodes, we can not distinguish between the orbital or spatial interference of the modes. The gate dependence support this hypothesis, since the oscillation amplitude, like the occupation of the second sub band, decreases and then disappears. Therefore we conclude that the supercurrent revival originates from multi-band superconducting quantum interference.

## 8.6. CONCLUSIONS

In conclusion, we did not observe a Zeeman induced  $0 - \pi$ -transition in a InAs JJ up to a magnetic field of 0.5 T. This is due to a combination of a high electron density, a low Landé  $g$ -factor, and low transparency. Furthermore, we learned that the geometry of a short semiconducting JJ could lead to unwanted switching current oscillations in a large in-plane magnetic field, probably originating from interference of multiple bands in the semiconductor. This effect should be taken into account in future experiments on Zeeman induced  $0 - \pi$ -transitions.

<sup>2</sup> $E_T$  in this junction is much much larger than  $E_Z$ , so we are not looking at a  $0 - \pi$ -transition.

<sup>3</sup>For a detailed description of the interference patterns for different  $d/L$  in ballistic and diffusive regimes see chapter 7.

## 8.7. SUPPLEMENTARY MATERIAL

### 8.7.1. CPR MEASURED WITH A DC SQUID

The current phase relation in a Josephson junction can be measured by sweeping the superconducting phase difference in a superconducting quantum interference device (SQUID). In such a device the junction of interest is shorted by either a superconducting lead (RF SQUID) or another Josephson junction (DC SQUID), see Fig. 8.S1a. For a static DC SQUID (neglecting R and C effects), the normalized current is the sum of the current through junction 1 ( $i_1$ ) and junction 2 ( $i_2$ ) [175]:

$$i = i_1 + i_2 = (1 - \alpha_1) \sin(\phi_1) + (1 + \alpha_1) \sin(\phi_2) \quad (8.S1)$$

where  $\alpha_1$  is the asymmetry of the critical currents  $(I_{c,2} - I_{c,1}) / (I_{c,2} + I_{c,1})$ . In the asymmetric limit ( $\alpha_1 \ll 1$ ), then all phase difference drops over the device junction, and its CPR can be measured. Sweeping the phase difference is done by threading a magnetic flux through the loop. Additionally, the current in the loop adds to the flux via the inductance such that the total flux becomes:

$$\Phi_T = \Phi_a + L_1 I_{c,1} - L_2 I_{c,2}, \quad (8.S2)$$

where  $\Phi_a$  is the applied flux,  $L$  is inductance and  $I_c$  is the critical current. In the case of zero inductance asymmetry, the phase difference is:

$$\phi_2 = \phi_1 + 2\pi\Phi_a/\Phi_0 + \pi\beta_L \left( \frac{i_1 - i_2}{2} \right) \quad (8.S3)$$

where  $\beta_L = LI_c/\Phi_0$  and  $(i_1 - i_2)/2$  is the circulating current. For  $\beta_L \ll 1$ ,  $\phi_2 = \phi_1 + 2\pi\Phi_a/\Phi_0$ , and eq. 8.S1 needs to be solved such that  $i$  is maximized. In the asymmetric case, where  $I_1 \ll I_2$ , this leads to a phase difference  $\phi_1$  close to the maximum obtainable supercurrent at  $\phi_1 = \pi/2$ . As  $\phi_1$  can be considered a constant now,  $\phi_2$  only depends on  $\Phi_a$ . Then the CPR of junction 2 can thus be measured by sweeping the applied magnetic field. In the experiment however, we usually do not operate in the limit where  $\beta_L \ll 1$ .

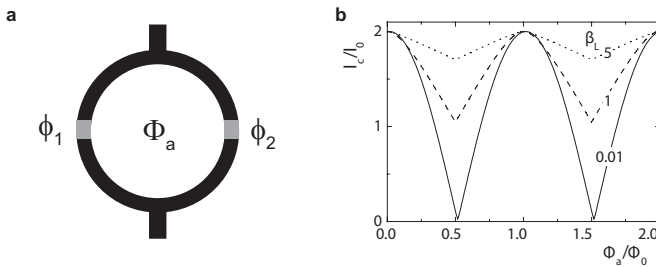


Figure 8.S1: **DC SQUID and node lifting due to inductance, a** Schematic DC SQUID. Two junctions, 1 & 2, are enclosed in a loop where a flux can be applied  $\Phi_a$  that influences the superconducting phase differences  $\phi_1$  and  $\phi_2$ . **b** The effect of inductance screening on the interference pattern of a symmetric DC SQUID. Figure taken from [175].

The inductance could then have typically two effects in the measured signal, either the

nodes are lifted (Fig. 8.S1b) or the shape could be distorted due to reentrant behavior. [183]. These underlines the importance of being in the right regime to be able to measure the CPR in a DC SQUID.

### 8.7.2. SUPPLEMENTARY FIGURES

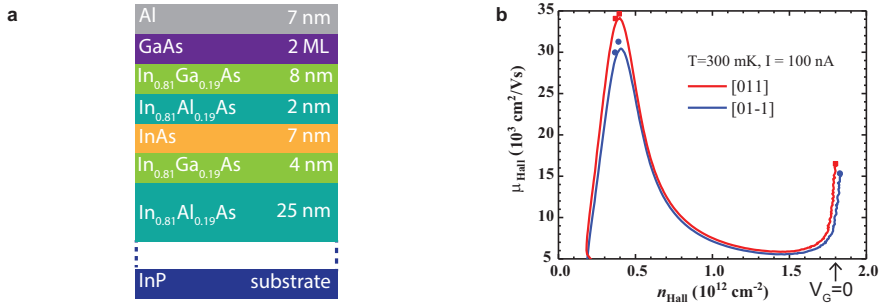


Figure 8.S2: **Quantum well heterostack and density versus mobility measurement.** **a** The InAs quantum well is grown on a InP substrate with InGaAs and InAlAs barriers. The Al grown epitaxially on top serves as the superconducting contact. All layer thicknesses are indicated. **b** Measurement of the electron density versus the electron mobility in two different crystal directions. A Hall bar geometry is used with a top gate separated from the device by 15 nm  $\text{AlO}_x$  dielectric. The mobility peaks and then decreases around a density of  $4 \cdot 10^{11} \text{ cm}^{-2}$ . At zero gate voltage the density is  $1.8 \cdot 10^{12} \text{ cm}^{-2}$ . Since the mobility peaks at a density far below the nominal density, we expect to have two bands in the perpendicular direction contributing to the transport at zero gate voltage. These measurements are done by our collaborators from Purdue University.

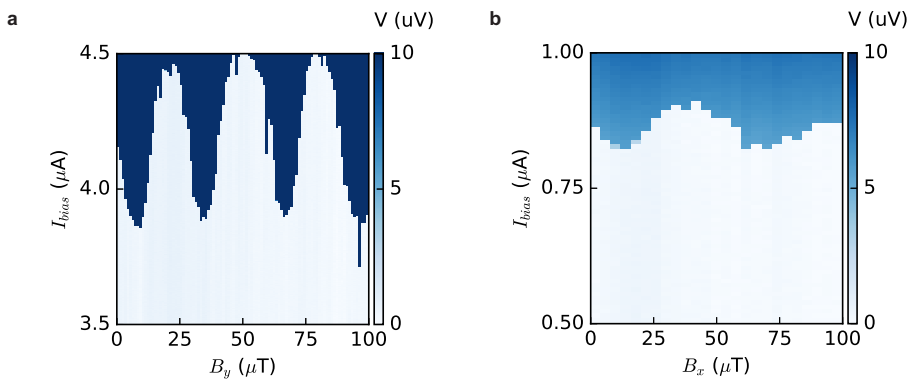


Figure 8.S3: **SQUID oscillations as a function of  $B_x$  and  $B_y$ .** **a** Current bias versus magnetic field in the  $y$ -direction. The switching current oscillates about 3.5 times in  $100 \mu\text{T}$ . **b** Same as **a** with magnetic field in the  $x$ -direction. The switching current undergoes 1.5 oscillations. Thus the alignment of the  $y$ - and  $x$ - axis is estimated to be  $60^\circ$  and  $30^\circ$  of the perpendicular direction, respectively.



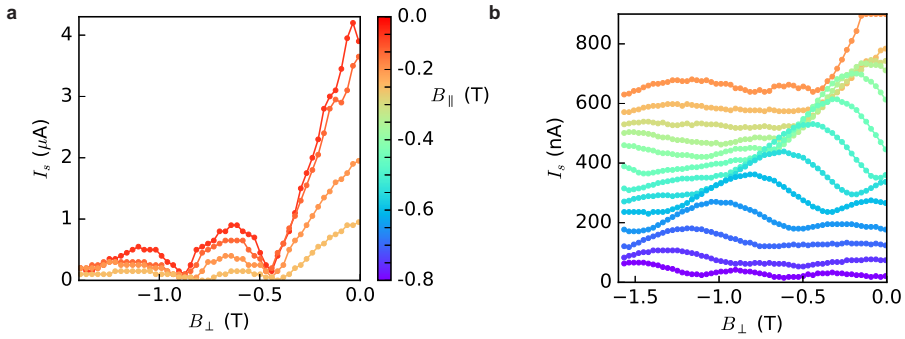


Figure 8.S4: **Fraunhofer pattern as a function of parallel magnetic field.** **a** and **b** shows the switching current versus  $B_{\perp}$  measurements as  $B_{\parallel}$  is stepped from 0 T to  $-0.8$  T (0.05 T step). In **b** the switching current for every subsequent trace is offset by 50 nA. We see the top of the central lobe decreases first and then peaks at  $-0.4$  T. An asymmetry in the first lobes occurs, due to the in-plane magnetic field parallel to the current [187].

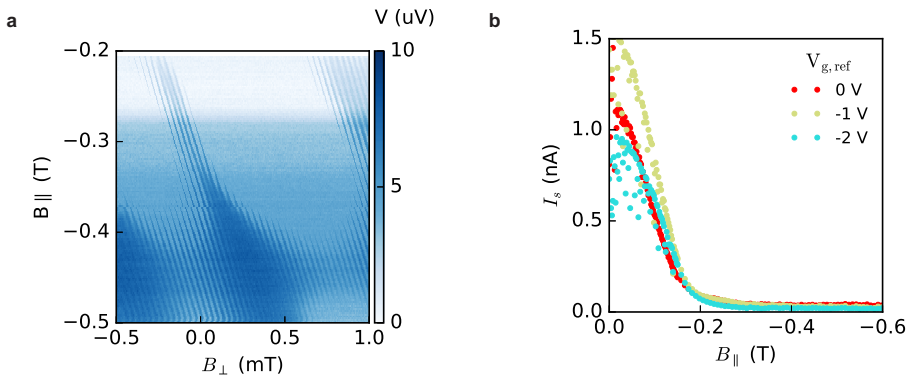


Figure 8.S5: **Switching current versus parallel magnetic field in other devices.** **a** Constant current bias as a function of  $B_{\perp}$  and  $B_{\parallel}$  for a device with  $L = 250$  nm. The voltage peaks around  $-0.45$  T and revives after that. **b** Switching current versus  $B_{\parallel}$  for a junction with  $L = 500$  nm for the indicated gate voltages  $V_g$ . The switching current monotonically decays, there is no oscillation visible.

# 9

## OUTLOOK

*We present and discuss ideas for future research in the material systems used in this thesis. First, the prospects of engineering a topological superconductor in Ge-Si nanowires are described. Then, applications of InSb flakes are considered, exploiting the flexibility of this platform. Finally, a thorough discussion on optimizing the topological gap in planar Josephson junctions is presented. We consider a new device geometry that enhances this gap and discuss how to measure it. Furthermore, several potential material systems are described and compared.*

## 9.1. GE-SI NANOWIRES

The Ge-Si nanowires studied are a potential platform to engineer a topological superconductor [77, 157, 158]. Here we discuss what is needed to reach this regime, in terms of spin-orbit interaction, Zeeman energy and induced superconductivity.

The spin-orbit interaction that stems from the direct coupling of the hole bands, needs to be considered quantitatively to confirm that its strength is sufficient. Being in the strong SOI regime, where  $E_{SO} > E_Z$ , is beneficial for the localization of the Majorana bound states (MBS) [77]. The strength of the direct Rashba SOI can be tuned via the coupling of the hole bands (occurring in 1D geometries [16]), and with applied electric field [17]. This coupling is dependent on the confinement and on strain induced by the Si shell. Finding the right combination of diameters for the Ge core and Si shell is thus crucial to obtain strong coupling. Theoretically  $E_{SO}$  of several meV can be reached in a Ge core of 6 nm diameter and a shell of 1.2 nm thick, under influence of an applied electric field [16]. In recent experiments encouraging results were obtained, as  $E_{SO} = 2.1$  meV was estimated from a quantum point contact [189], and weak anti-localization measurements result in similar values [190].

The Zeeman energy needed to reach the topological regime is  $E_Z > \sqrt{\Delta^2 + \mu^2}$ , where  $\Delta$  is the superconducting gap and  $\mu$  the chemical potential. Using for example aluminium, Al, with  $\Delta \sim 200\mu\text{V}$  and at a sufficiently low  $\mu$ ,  $E_Z$  is smaller than the  $E_{SO}$  mentioned before. However, a new challenge arises, since  $E_Z$  should become at least  $\Delta$  to enter the topological regime. For this, a magnetic field of around 1 T is needed, considering the Landé  $g$ -factor of 3.5 measured in chapter 4. However, in the Josephson junction of chapter 4, the induced superconductivity is already suppressed at such a magnetic field. To overcome this issue, the  $g$ -factor might be increase by tuning the electric field applied [87]. Another solution would be to increase the critical magnetic field of the induced superconductivity either by geometry or material engineering. Reducing the thickness of the Al increases its resilience against magnetic fields, which can be done by in situ growth of the Al [191]. Annealing the nanowires after the growth would form a transparent contact. In addition, it has been reported that the annealing could lead to the formation of a superconducting alloy (consisting of Ge, Si, Al) with a larger critical magnetic field than Al [59]. The improvements described make it possible to bring the Ge-Si nanowires in the topological regime.

## 9.2. INSb FLAKES

The InSb flake Josephson junctions are a unique hybrid superconductor semiconductor system, combining advantages of a 2D system, and the flexibility of transferable nanostructures. The flakes offer the possibility of making multi terminal devices, in contrast to the two terminal measurements in nanowires, while maintaining the freedom of choice in terms of the substrate used.

In a multi terminal device with superconducting contacts, the Andreev spectrum depends on the superconducting phase differences between the contacts. Treating the phase differences as quasi momenta, topological effects such as Weyl singularities can arise [192]. Using existing shadow evaporation techniques [55], such devices could be realized in InSb flakes. Furthermore, combining superconducting and normal metal

contacts allows for study of the spatial extent of the Andreev bound states. Additionally, in a topological superconductor, the nonlocal properties of the MBS could be investigated [193].

The flexibility in choice of substrate allows for the integration of flake Josephson junctions in microwave quantum circuits, as done before with nanowires [194, 195]. The flakes offer a good alternative to the nanowires because of their larger Josephson coupling. Additionally, fabricating a superconducting quantum point contact in a flake, would lead to a tunable and quantized Josephson energy, which is interesting for qubit applications.

### 9.3. ROBUST MAJORANA'S IN PLANAR JOSEPHSON JUNCTIONS

Planar Josephson junctions in semiconductors with strong SOI offer a new platform to create a topological superconductor [171, 172]. The addition of the superconducting phase difference as an experimental knob, leads to a reduction of the magnetic field needed to enter the topological phase, which is favorable for maintaining the induced superconductivity and minimizes magnetic orbital effects. In addition, the topological phase that occurs at  $\pi$  phase difference is stable as a function of chemical potential [171]. In this outlook, we first focus on maximizing the gap of the topological superconductor to obtain robust MBSs. We describe a new geometry that enhances the trivial and topological superconducting gap. Then, we describe an experimental device that allows for probing of the nonlocality of the MBS. Finally, we discuss possible material systems conclude which is preferable to reach the topological regime at a minimal magnetic field.

#### 9.3.1. TOPOLOGICAL GAP

The gap in the topological regime of a planar Josephson junctions generally depends on the various energy scales in the system: the SOI energy at the Fermi level,  $\Delta_{\text{SO}}$ , the Zeeman energy,  $E_Z$ , the Thouless energy,  $E_T$ , and the superconducting gap,  $\Delta$ . The phase diagram for the short junction limit and taking  $\Delta_{\text{SO}} \gg E_Z$ , as obtained in Ref. 171, is presented in Fig. 9.1a. Additionally, the phase diagram for a long junction is shown and discussed in chapter 8. The magnitude of the topological gap in both phase diagrams at  $k_x = 0$  is bounded by  $E_T$  and  $\Delta$  for the long and short junction limit, respectively [171].

In Ref. 171 the energy gap is calculated throughout the phase diagram of a junction with an intermediate length (Fig. 9.1b). The gap in the topological regime is largest at  $\phi = \pi$  and  $E_{Z,J}/\Delta \approx 7$ . In terms of the Thouless energy<sup>1</sup>, the largest gap occurs once  $E_{Z,J} \lesssim E_T$ . Furthermore, the topological phase and gap for  $\phi = \pi$  are stable as a function of chemical potential (Fig. 9.1c) [171]. Note that both the suppression of  $\Delta$  in the superconductor as a function of magnetic field, and the magnetic orbital effect are not taken into account. These effect can significantly reduce the magnitude of the gap as a function of magnetic field [90], and therefore should be further investigated theoretically. Concerning the experiments, this makes it even more crucial to have the transition at low magnetic fields.

In Fig. 9.1d,f we observe that the overall gap is limited by the states at  $k_F$  for both in

<sup>1</sup>Analogous to the phase diagram in the long junction (Fig. 8.1),  $E_T$  equals the energy of the phase boundary at  $\phi = 0$ .

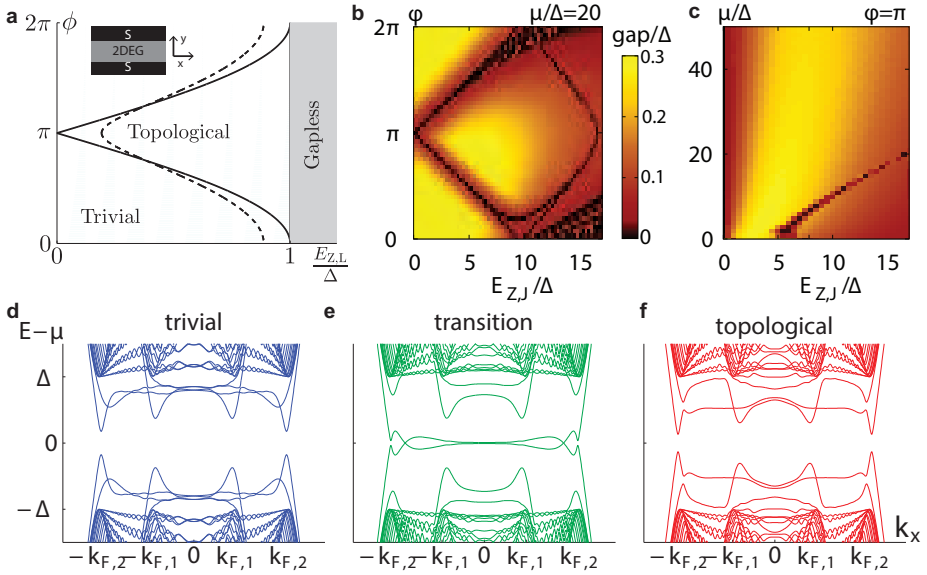


Figure 9.1: **Topological gap in a planar Josephson junction.** **a** Phase diagram for the short junction limit. Depending on the superconducting phase difference  $\phi$  and the ratio of the Zeeman energy in the leads and superconducting gap,  $E_{Z,L}/\Delta$ , the junction is in a trivial, topological or gapless state. The boundaries between the trivial and topological phases are given for unity (solid line) and 0.75 transparency (dashed line). The inset shows a schematic image of the planar junction, including the coordinate system. **b** The magnitude of the gap as a function of  $\phi$  and Zeeman field in the junction,  $E_{Z,J}$ , for a junction with an intermediate length. The chemical potential,  $\mu$ , used is  $20\Delta$ . **c** The magnitude of the gap in the same geometry as **b**, for a varying  $\mu$  at  $\phi = \pi$ . **d-f** Bandstructures for a similar device as used for **b,c** in the trivial regime, at the transition (closing gap), and in the topological regime. The Fermi wavenumbers,  $k_F$ , for the two Fermi surfaces, split by the Rashba SOI, are highlighted. All figures are taken from Ref. 171, where details of the calculations can be found as well.

the trivial and topological regime. In a quasi-classical picture, the states with a large momentum  $k_x$  follow long trajectories in the semiconductor, before reflecting at the superconductor. In terms of the Thouless energy, a long trajectory leads to a small  $E_T$ , and subsequently a smaller induced superconducting gap. Limiting the long trajectories through the junctions could thus increase the overall magnitude of the gap. A quasi-classical model in a trivial Josephson junction showed that introducing disorder in the junction does indeed enhance the induced superconducting gap [196]. The scattering events not only limit the length of the trajectory, but also couple states with different  $k_x$  (and therefore different gaps), which leads to an increase of the overall gap. Recently it has been shown that this mechanism works analogous for the topological gap [197]. However, introducing disorder in the junction is unfavorable for the transport properties, and hard to control. Therefore, we take a different route and only limit the length of the trajectories, by changing the geometry of the Josephson junction.

When a zigzag shape is introduced in the superconducting contacts [198] (Fig. 9.2a), the quasi-classical (straight) trajectories can maximally be the length of a single segment. Laeven *et al.* performed tight binding calculations to obtain the bandstructures for a straight and zigzag geometry, as presented in Fig. 9.2b and c, respectively. For

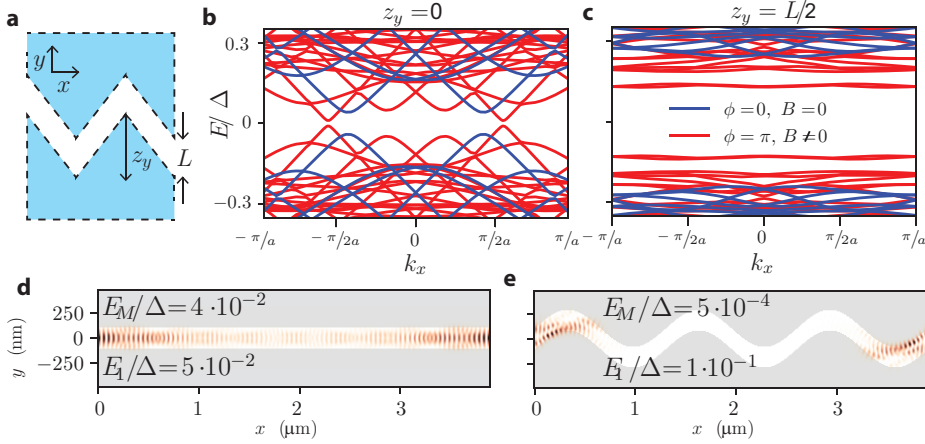


Figure 9.2: **Enhanced gap in zigzag geometry.** **a** Schematic representation of a zigzag Josephson junction. The length,  $L$ , and zigzag amplitude,  $z_y$ , are indicated. **b,c** Result of bandstructure calculations performed by Laeven *et al.*, for a straight and zigzag junction, respectively [198]. All momenta are folded to the first Brillouin zone and a junction length,  $L$ , of 200 nm is used. The blue lines represents the bands in the trivial regime ( $\phi = 0$ ,  $B = 0$  T) and the red lines in the topological regime ( $\phi = \pi$ ,  $B = 1$  T). The following parameters are used:  $\Delta = 1$  meV,  $E_Z = 1.5$  meV ( $g = 26$ ),  $\Delta_{SO} = 4$  meV Å,  $E_T = 2$  meV ( $n = 1.6 \cdot 10^{15}$ ). **d,e** Wavefunctions of Majorana bound states in the topological regime of the straight and zigzag junction, respectively. The topological gap,  $E_1$ , and splitting of the Majorana bound states,  $E_M$ , are presented, both in eV. Figures **b-e** are taken from Ref. 198.

both the trivial (blue lines) and topological (red lines) regimes the gap is larger for the zigzag shaped junction. The enhancement of the topological gap is also reflected in a shorter localization length of the MBS wavefunctions [198], as shown in Fig. 9.2d,e. The energy scales given are the topological gap,  $E_1$ , and the splitting of the MBS due to their overlap,  $E_M$ . The zigzag geometry thus increases the topological gap and reduces the MBS overlap, which are beneficial for future applications in topological quantum computation [199].

### 9.3.2. CORRELATION AND NONLOCAL MEASUREMENT

Here we implement the zigzag geometry in a device and describe an experimental setup that allows for probing of the nonlocality of the MBS. A local density of states (LDOS) measurement at the boundary of a topological superconductor, can reveal the MBS as a zero bias peak in the tunneling conductance. The first observation [78] and the subsequent results in nanowires [79] and phase biased 2DEG Josephson junctions [173, 174], all have in common that a single MBS (one side of the topological superconductor) is probed. Next to that, a multi probe device revealed the appearance of a zero bias peak at the end, and a simultaneous gap re-opening in the bulk of the topological superconductor [200]. In the device presented here, the goal is to be able to probe the entire topological superconductor segment, including both ends.

The proposed device consists of a zigzag Josephson junction in an RF SQUID geometry, with local density of states probes at its edges (Fig. 9.3). The probes are represent

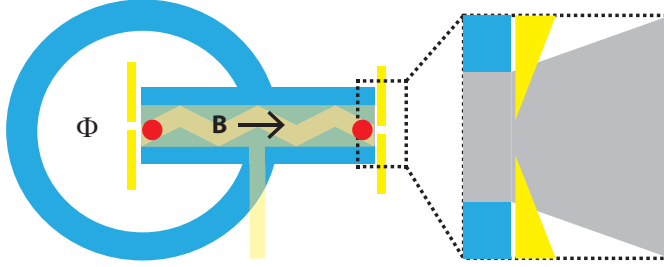


Figure 9.3: **Phase biased zigzag Josephson junction, with tunnel probes at both edges.** The superconductor is colored blue, the semiconductor is grey and the metal top gates are yellow. The zoom in reveals a split gate geometry to allow for tunneling spectroscopy at the edge of the junction. The superconducting phase can be adjusted with the flux,  $\Phi$ , through the ring. The in-plane magnetic field,  $B$ , and predicted location of the Majorana bound states (red dots) are indicated. Depending on the experiment, a voltage or current bias measurement setup can be used for this three terminal device.

by a split gate here, but an semi insulating barrier or a quantum dot could also be used. The overlap of the MBS wavefunctions, can be tuned via the chemical potential with the global bottom gate, and should result in correlated oscillations in the measured LDOS at both edges [201]. Comparing the two LDOS spectra as a function of magnetic field and gate voltage, therefore could reveal whether the MBS at the two ends form a pair [202]. Furthermore, using the two contacts from the sides as normal leads allows for nonlocal conductance measurements. With such a measurement the size of the topological gap, and the phase transitions between the trivial and topological regimes can be obtained [193]. Both measurements could give substantial evidence for the occurrence of a single topological superconducting segment extended through the entire Josephson junction. This will pave the way for future experiments that probe the predicted non-Abelian exchange statistics of the MBSs [199, 203].

### 9.3.3. MATERIAL SYSTEM

Material	$n$ ( $10^{15}\text{m}^{-2}$ )	$m_{\text{eff}}$ ( $m_e$ )	$g$	$E_T$	$E_Z$	$\Delta_{\text{SO}}$
InAs/InGaAs	18	0.04[67]	4 [67]	0.67	0.12	10 [69]
InAs/AlSb	18 [204]	0.041 [204]	12 [66]	0.67	0.35	2.5 [204]
InSb/InAlSb	2 [170]	0.019 [170]	26 [170]	0.45	0.75	1.1 [205]
HgTe/CdTe	20 [206]	0.049 [206]	20 [207]	0.55	0.58	30 [206]

Table 9.1: **2DEG parameters and energy scales.** Four different semiconductor quantum wells, denoted by the active and barrier layer, are presented. The energy scales are calculated with values from the literature. For  $E_T$  a length of the junction of  $1\mu\text{m}$  is used, and  $E_Z$  is taken at 0.5 T. All energy scales are given in meV.

In chapter 8 we studied a phase biased InAs Josephson junction, but did not find evidence for a topological phase. This was most likely due to the a misfit of the relevant energy scales and a suboptimal contact transparency. In order to reach the topological regime the right combination of  $E_T$ ,  $E_Z$  and contact transparency should be found, while

maintaining the induced superconductivity in the semiconductor with strong SOI. Apart from InAs [174]; HgTe [173] and InSb are semiconductors that could potentially be used for this. The relevant material parameters and estimated energy scales for these materials are listed in table 9.1.

The effective mass,  $m_{\text{eff}}$ , and Landé  $g$ -factor,  $g$ , are strongly dependent on the choice of material. In contrast, the electron density,  $n$ , depends on the doping in the quantum well, and can be altered with an electrostatic gate. However, lowering the density usually leads to an unwanted reduction of the supercurrent in a Josephson junction. The difference in  $n$  and  $m_{\text{eff}}$  reflect in  $E_T \propto \sqrt{n}/m_{\text{eff}}$ , which turn out to be relatively close to each other for the different materials. In contrast, the  $g$ -factors and corresponding  $E_Z$  differ much more. InAs/InGaAs quantum wells, as used in chapter 8, have the lowest  $g$ -factor, whereas the  $g$  of InSb stands out. Comparing  $E_T$  and  $E_Z$ , the InSb quantum well is the best candidate to reach the optimal topological gap at a minimal magnetic field.

The spin-orbit energy,  $\Delta_{\text{SO}}$  is the largest energy scale for all materials, in accordance with the model proposed by Pientka *et al.*. Nevertheless, for the InSb quantum well  $\Delta_{\text{SO}} \propto E_Z$ , a case that is considered only in the absence of a phase bias in Ref. 172. Whether the phase diagram is altered at  $\phi = \pi$  is unknown and needs further theoretical investigation. Apart from its magnitude, the type of SOI also matters. Both Refs. 171 and 172 consider Rashba SOI only, even though in the materials considered above Dresselhaus SOI could also occur [9, 204, 205]. A Dresselhaus component in combination with the magnetic field (perpendicular to the direction of current), leads to a tilt in the bandstructure of Fig. 9.1c-e. This tilting can potentially close the gap with an increasing magnetic field. The magnitude of the the Dresselhaus SOI and its effect on the topological gap should thus be studied both experimentally and theoretically.

The induced gap depends on the gap of the superconductor, and its coupling to the semiconductor. We consider two candidate superconductors, Al and niobium titanium

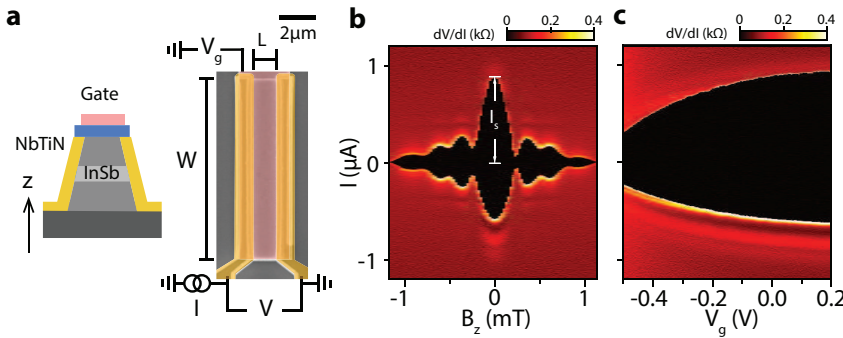


Figure 9.4: **Josephson junctions in InSb quantum wells.** **a** Schematic representation and optical image of the device made of an InSb quantum well with NbTiN contacts. An electrostatic gate is added on top of the quantum well to alter the electron density. The quasi 4 terminal measurement setup is indicated as well as the junction length  $L$  and width  $W$ . **b** Differential resistance,  $dV/dI$ , measurement as a function of current bias,  $I$ , perpendicular magnetic field,  $B_z$ . A typical Fraunhofer superconducting quantum interference pattern is observed, and the switching current,  $I_s$ , at  $B = 0$  T is indicated. **c**  $dV/dI$  as a function of  $I$  and gate voltage,  $V_g$ , revealing that  $I_s$  is tunable with the top gate.



nitride, NbTiN. An InAs quantum well with epitaxially grown Al contacts have shown to exhibit highly transparent contacts, with a superconducting gap of around  $200 \mu\text{eV}$  [84]. In comparison, NbTiN has a larger  $\Delta$  of around  $1.5 \text{ meV}$ , and is more challenging to produce high transparency contacts with [61].

To conclude, a combination of an InSb 2DEG with highly transparent NbTiN contacts would be the best combination of materials. We recently fabricated and measured Josephson junctions with NbTiN contacts in high quality InSb 2DEGs [208]. The first results are presented in Fig. 9.4, where the supercurrent is tunable with a magnetic field and with a gate, as expected for a semiconducting Josephson junction. These measurements highlight the promise of this material combination for engineering a topological superconductor.

# BIBLIOGRAPHY

- [1] Griffiths, D. J. *Introduction to Quantum Mechanics* (Pearson Prentice Hall, 2005)
- [2] Skolasinski, R. J. *Topology, Magnetism, and Spin-Orbit*. Ph.D. thesis, Delft University of Technology, Netherlands (2018)
- [3] Bardeen, J. Surface states and rectification at a metal semi-conductor contact. *Phys. Rev.* **71**, 717–727 (1947)
- [4] Hanson, R., Kouwenhoven, L. P., Petta, J. R., Tarucha, S. & Vandersypen, L. M. K. Spins in few-electron quantum dots. *Rev. Mod. Phys.* **79**, 1217–1265 (2007)
- [5] Cronenwett, S. M., Oosterkamp, T. H. & Kouwenhoven, L. P. A tunable kondo effect in quantum dots. *Science* **281**, 540–544 (1998)
- [6] Goldhaber-Gordon, D. *et al.* Kondo effect in a single-electron transistor. *Nature* **391**, 156 (1998)
- [7] Ihn, T. *Semiconductor Nanostructures: Quantum states and electronic transport* (Oxford University Press, 2010)
- [8] von Klitzing, K. The quantized hall effect. *Rev. Mod. Phys.* **58**, 519–531 (1986)
- [9] Winkler, R. *Spin-orbit Coupling Effects in Two-dimensional Electron and Hole Systems* (Springer-Verlag GmbH, 2003)
- [10] Kane, E. O. Band structure of indium antimonide. *J. Phys. Chem. Solids* **1**, 249 – 261 (1957)
- [11] van den Berg, J. W. G. *Single spins in nanowire quantum dots with strong spin-orbit interaction*. Ph.D. thesis, Delft University of Technology, Netherlands (2014)
- [12] Dresselhaus, G. Spin-orbit coupling effects in zinc blende structures. *Phys. Rev.* **100**, 580–586 (1955)
- [13] Bychkov, Y. A. & Rashba, E. I. Properties of a 2d electron gas with lifted spectral degeneracy. *JETP Lett.* **39**, 78 (1984)
- [14] Beukman, A. J. A. *Topology in two-dimensional systems*. Ph.D. thesis, Delft University of Technology, Netherlands (2016)
- [15] Ganichev, S. D. & Golub, L. E. Interplay of rashba/dresselhaus spin splittings probed by photogalvanic spectroscopy –a review. *Phys. Status Solidi B* **251**, 1801–1823

- 
- [16] Kloeffel, C., Rancic, M. J. & Loss, D. Direct rashba spin-orbit interaction in si and ge nanowires with different growth directions. *Phys. Rev. B* **97**, 235422 (2018)
- [17] Kloeffel, C., Trif, M. & Loss, D. Strong spin-orbit interaction and helical hole states in ge/si nanowires. *Phys. Rev. B* **84**, 195314 (2011)
- [18] Winkler, G. W. *et al.* Orbital contributions to the electron g factor in semiconductor nanowires. *Phys. Rev. Lett.* **119**, 037701 (2017)
- [19] Bir, G. L. & Pikus, G. *Symmetry and strain-induced effects in semiconductors* (New York, Wiley, 1974)
- [20] De Gennes, P.-G. *Superconductivity of metals and alloys* (W.A. Benjamin, 1966)
- [21] Tinkham, M. *Introduction to Superconductivity*. Dover Books on Physics Series (Dover Publications, 1996)
- [22] Josephson, B. D. Possible new effects in superconductive tunnelling. *Phys. Lett.* **1**, 251 – 253 (1962)
- [23] Andreev, A. The thermal conductivity of the intermediate state in superconductors. *JETP Lett.* **19**, 1228 (1964)
- [24] Harmans, C. *Mesoscopic Physics: An Introduction* (TU Delft, 1997)
- [25] Altshuler, B. & Spivak, B. Mesoscopic fluctuations in a superconductor–normal metal–superconductor junction. *Zh. Eksp. Teor. Fiz.* **92**, 607–615 (1987)
- [26] Beenakker, C. W. J. Universal limit of critical-current fluctuations in mesoscopic josephson junctions. *Phys. Rev. Lett.* **67**, 3836–3839 (1991)
- [27] Dynes, R. C. & Fulton, T. A. Supercurrent density distribution in josephson junctions. *Phys. Rev. B* **3**, 3015–3023 (1971)
- [28] Hui, H.-Y., Lobos, A. M., Sau, J. D. & Das Sarma, S. Proximity-induced superconductivity and josephson critical current in quantum spin hall systems. *Phys. Rev. B* **90**, 224517 (2014)
- [29] Heida, J. P., van Wees, B. J., Klapwijk, T. M. & Borghs, G. Nonlocal supercurrent in mesoscopic josephson junctions. *Phys. Rev. B* **57**, R5618–R5621 (1998)
- [30] Ledermann, U., Fauchere, A. L. & Blatter, G. Nonlocality in mesoscopic josephson junctions with strip geometry. *Phys. Rev. B* **59**, R9027–R9030 (1999)
- [31] Barzykin, V. & Zagoskin, A. M. Coherent transport and nonlocality in mesoscopic sns junctions: anomalous magnetic interference patterns. *Superlattice. Microst.* **25**, 797 – 807 (1999)
- [32] Rasmussen, A. *et al.* Effects of spin-orbit coupling and spatial symmetries on the josephson current in sns junctions. *Phys. Rev. B* **93**, 155406 (2016)

- 
- [33] Suominen, H. J. *et al.* Anomalous fraunhofer interference in epitaxial superconductor-semiconductor josephson junctions. *Phys. Rev. B* **95**, 035307 (2017)
- [34] Assouline, A. *et al.* Spin-orbit induced phase-shift in bi 2 se 3 josephson junctions. *Nature Commun.* **10**, 126 (2019)
- [35] Bezuglyi, E. V., Rozhavsky, A. S., Vagner, I. D. & Wyder, P. Combined effect of zeeman splitting and spin-orbit interaction on the josephson current in a superconductor–two-dimensional electron gas–superconductor structure. *Phys. Rev. B* **66**, 052508 (2002)
- [36] Fulde, P. & Ferrell, R. A. Superconductivity in a strong spin-exchange field. *Phys. Rev.* **135**, A550–A563 (1964)
- [37] Larkin, A. I. & Ovchinnikov, I. U. N. Inhomogeneous state of superconductors(production of superconducting state in ferromagnet with fermi surfaces, examining green function). *JETP Lett.* **20**, 762–769 (1965)
- [38] Bulaevskii, L. N., Kuzii, V. V. & Sobyenin, A. A. Superconducting system with weak coupling to the current in the ground state. *JETP Lett.* **25**, 290–294 (1977)
- [39] Buzdin, A. I., Bulaevskii, L. N. & Panyukov, S. V. Critical-current oscillations as a function of the exchange field and thickness of the ferromagnetic metal (f) in an sfs josephson junction. *JETP Lett.* **35**, 147 (1982)
- [40] Demler, E. A., Arnold, G. B. & Beasley, M. R. Superconducting proximity effects in magnetic metals. *Phys. Rev. B* **55**, 15174–15182 (1997)
- [41] Yokoyama, T., Eto, M. & Nazarov, Y. V. Anomalous josephson effect induced by spin-orbit interaction and zeeman effect in semiconductor nanowires. *Phys. Rev. B* **89**, 195407 (2014)
- [42] Szombati, D. B. *et al.* Josephson  $\phi_0$ -junction in nanowire quantum dots. *Nature Phys.* **12**, 568–573 (2016)
- [43] Hart, S. *et al.* Controlled finite momentum pairing and spatially varying order parameter in proximitized hgte quantum wells. *Nature Phys.* **13**, 87 (2017)
- [44] Zuo, K. *et al.* Supercurrent interference in few-mode nanowire josephson junctions. *Phys. Rev. Lett.* **119**, 187704 (2017)
- [45] Zuo, K. & Mourik, V. *Signatures of Majorana Fermions in Hybrid Superconductor-Semiconductor Nanowire Devices*. Ph.D. thesis, Delft University of Technology, Netherlands (2016)
- [46] Kammhuber, J. *Spin-orbit interaction in ballistic nanowire devices*. Ph.D. thesis, Delft University of Technology, Netherlands (2017)

- [47] Kjaergaard, M. *Proximity Induced Superconducting Properties in One and Two Dimensional Semiconductors*. Ph.D. thesis, Copenhagen University, Denmark (2015)
- [48] Schäffler, F. High-mobility si and ge structures. *Semicond. Sci. Technol.* **12**, 1515 (1997)
- [49] Xiang, J. *et al.* Ge/si nanowire heterostructures as high-performance field-effect transistors. *Nature* **441**, 489 EP – (2006)
- [50] Conesa-Boj, S. *et al.* Boosting hole mobility in coherently strained [110]-oriented ge-si core-shell nanowires. *Nano Lett.* **17**, 2259–2264 (2017)
- [51] Xiang, J., Vidan, A., Tinkham, M., Westervelt, R. M. & Lieber, C. M. Ge/si nanowire mesoscopic josephson junctions. *Nature Nanotech.* **1**, 208–13 (2006)
- [52] Pan, D. *et al.* Free-standing two-dimensional single-crystalline insb nanosheets. *Nano Lett.* **16**, 834–841 (2016)
- [53] Plissard, S. R. *et al.* From insb nanowires to nanocubes: Looking for the sweet spot. *Nano Lett.* **12**, 1794–1798 (2012)
- [54] de la Mata, M. *et al.* Twin-induced insb nanosails: A convenient high mobility quantum system. *Nano Lett.* **16**, 825–833 (2016)
- [55] Gazibegovic, S. *et al.* Epitaxy of advanced nanowire quantum devices. *Nature* **548**, 434 (2017)
- [56] Flohr, K. *et al.* Manipulating inas nanowires with submicrometer precision. *Rev. Sci. Instrum.* **82**, 113705 (2011)
- [57] Su, Z. *et al.* High critical magnetic field superconducting contacts to ge/si core/shell nanowires. *arXiv preprint 1610.03010* (2016)
- [58] Ridderbos, J. *et al.* Josephson effect in a few-hole quantum dot. *Advan. Mater.* **0**, 1802257 (2018)
- [59] Ridderbos, J. *Quantum dots and superconductivity in Ge-Si nanowires*. Ph.D. thesis, University of Twente, Netherlands (2018)
- [60] Suyatin, D. B., Thelander, C., Björk, M. T., Maximov, I. & Samuelson, L. Sulfur passivation for ohmic contact formation to inas nanowires. *Nanotechnology* **18**, 105307 (2007)
- [61] Gül, Ö. *et al.* Hard superconducting gap in insb nanowires. *Nano Lett.* **17**, 2690–2696 (2017)
- [62] King, P. D. C., Veal, T. D., Lowe, M. J. & McConville, C. F. Surface electronic properties of clean and s-terminated insb(001) and (111)b. *J. Appl. Phys.* **104**, 083709 (2008)

- 
- [63] Bett, A., Dimroth, F., Stollwerck, G. & Sulima, O. Iii-v compounds for solar cell applications. *Appl. Phys. A* **69**, 119–129 (1999)
- [64] Kroemer, H. The 6.1 Å family (InAs, GaSb, AlSb) and its heterostructures: a selective review. *Physica E* **20**, 196–203 (2004)
- [65] Lee, J. S. *et al.* Contribution of top barrier materials to high mobility in near-surface inas quantum wells grown on gasb (001). *arXiv preprint 1809.06971* (2018)
- [66] Mu, X., Sullivan, G. & Du, R.-R. Effective g-factors of carriers in inverted inas/gasb bilayers. *Appl. Phys. Lett.* **108**, 012101 (2016)
- [67] Nitta, J., Lin, Y., Akazaki, T. & Koga, T. Gate-controlled electron g factor in an inas-inserted-channel in0.53ga0.47as/in0.52al0.48as heterostructure. *Appl. Phys. Lett.* **83**, 4565–4567 (2003)
- [68] Nguyen, B.-M., Yi, W., Noah, R., Thorp, J. & Sokolich, M. High mobility back-gated InAs/GaSb double quantum well grown on GaSb substrate. *Appl. Phys. Lett.* **106**, 032107 (2015)
- [69] Shabani, J. *et al.* Two-dimensional epitaxial superconductor-semiconductor heterostructures: A platform for topological superconducting networks. *Phys. Rev. B* **93**, 155402 (2016)
- [70] Lee, J. S. *et al.* Transport studies of epi-al/inas 2deg systems for required building-blocks in topological superconductor networks. *arXiv preprint 1705.05049* (2017)
- [71] Chaghi, R. *et al.* Wet etching and chemical polishing of inas/gasb superlattice photodiodes. *Semicond. Sci. Technol.* **24**, 065010 (2009)
- [72] Pobell, F. *Matter and methods at low temperatures*, vol. 2 (Springer, 1996)
- [73] Schouten, R. N. Qt designed instrumentation-ivvi rack page (2018). <http://qtnetwork.tudelft.nl/schouten/ivvi/index-ivvi.htm>
- [74] Nadj-Perge, S., Frolov, S. M., Bakkers, E. P. A. M. & Kouwenhoven, L. P. Spin-orbit qubit in a semiconductor nanowire. *Nature* **468**, 1084–7 (2010)
- [75] Kloeffel, C., Trif, M., Stano, P. & Loss, D. Circuit qed with hole-spin qubits in ge/si nanowire quantum dots. *Phys. Rev. B* **88**, 241405 (2013)
- [76] Alicea, J. New directions in the pursuit of majorana fermions in solid state systems. *Rep. Prog. Phys.* **75**, 076501 (2012)
- [77] Maier, F., Klinovaja, J. & Loss, D. Majorana fermions in ge/si hole nanowires. *Phys. Rev. B* **90**, 195421 (2014)
- [78] Mourik, V. *et al.* Signatures of majorana fermions in hybrid superconductor-semiconductor nanowire devices. *Science* **336**, 1003–1007 (2012)

- [79] Deng, M. T. *et al.* Majorana bound state in a coupled quantum-dot hybrid-nanowire system. *Science* **354**, 1557–1562 (2016)
- [80] Chang, W. *et al.* Hard gap in epitaxial semiconductor-superconductor nanowires. *Nature Nanotech.* **10**, 232–6 (2015)
- [81] Deacon, R. S. *et al.* Tunneling spectroscopy of andreev energy levels in a quantum dot coupled to a superconductor. *Phys. Rev. Lett.* **104**, 076805 (2010)
- [82] Lee, E. *et al.* Spin-resolved andreev levels and parity crossings in hybrid superconductor-semiconductor nanostructures. *Nature Nanotech.* **9**, 79–84 (2014)
- [83] Averin, D. & Bardas, A. ac josephson effect in a single quantum channel. *Phys. Rev. Lett.* **75**, 1831–1834 (1995)
- [84] Kjaergaard, M. *et al.* Transparent semiconductor-superconductor interface and induced gap in an epitaxial heterostructure josephson junction. *Phys. Rev. Appl.* **7**, 034029 (2017)
- [85] Scheer, E., Joyez, P., Esteve, D., Urbina, C. & Devoret, M. H. Conduction channel transmissions of atomic-size aluminum contacts. *Phys. Rev. Lett.* **78**, 3535–3538 (1997)
- [86] Goffman, M. F. *et al.* Conduction channels of an inas-al nanowire josephson weak link. *New J. Phys.* **19**, 092002 (2017)
- [87] Maier, F., Kloeffer, C. & Loss, D. Tunable gfactor and phonon-mediated hole spin relaxation in ge/si nanowire quantum dots. *Phys. Rev. B* **87**, 161305(R) (2013)
- [88] Brauns, M., Ridderbos, J., Li, A., Bakkers, E. P. A. M. & Zwanenburg, F. A. Electric-field dependent g-factor anisotropy in ge-si core-shell nanowire quantum dots. *Phys. Rev. B* **93**, 121408(R) (2016)
- [89] Brauns, M. *et al.* Anisotropic pauli spin blockade in hole quantum dots. *Phys. Rev. B* **94**, 041411 (2016)
- [90] Nijholt, B. & Akhmerov, A. R. Orbital effect of magnetic field on the majorana phase diagram. *Phys. Rev. B* **93**, 235434 (2016)
- [91] Blonder, G. E., Tinkham, M. & Klapwijk, T. M. Transition from metallic to tunneling regimes in superconducting microconstrictions: Excess current, charge imbalance, and supercurrent conversion. *Phys. Rev. B* **25**, 4515–4532 (1982)
- [92] Buitelaar, M. R., Nussbaumer, T. & Schonenberger, C. Quantum dot in the kondo regime coupled to superconductors. *Phys. Rev. Lett.* **89**, 256801 (2002)
- [93] Lee, E. J. H. *et al.* Zero-bias anomaly in a nanowire quantum dot coupled to superconductors. *Phys. Rev. Lett.* **109**, 186802 (2012)

- 
- [94] Bardas, A. & Averin, D. V. Electron transport in mesoscopic disordered superconductor normal-metal superconductor junctions. *Phys. Rev. B* **56**, R8518–R8521 (1997)
- [95] Luttinger, J. M. & Kohn, W. Motion of electrons and holes in perturbed periodic fields. *Phys. Rev.* **97**, 869–883 (1955)
- [96] Luttinger, J. M. Quantum theory of cyclotron resonance in semiconductors: General theory. *Phys. Rev.* **102**, 1030–1041 (1956)
- [97] Lawaetz, P. Valence-band parameters in cubic semiconductors. *Phys. Rev. B* **4**, 3460–3467 (1971)
- [98] Kloeffel, C., Trif, M. & Loss, D. Acoustic phonons and strain in core/shell nanowires. *Phys. Rev. B* **90** (2014)
- [99] Groth, C. W., Wimmer, M., Akhmerov, A. R. & Waintal, X. Kwant: a software package for quantum transport. *New J. Phys.* **16**, 063065 (2014)
- [100] de Vries, F. K. *et al.* Simulation codes and data for spin-orbit interaction and induced superconductivity in an one-dimensional hole gas (2018). DOI: [10.5281/zenodo.1310873](https://doi.org/10.5281/zenodo.1310873)
- [101] Csontos, D. & Zülicke, U. Large variations in the hole spin splitting of quantum-wire subband edges. *Phys. Rev. B* **76**, 073313 (2007)
- [102] Fabian, J., Matos-Abiague, A., Ertler, C., Stano, P. & Žutić, I. Semiconductor spintronics. *Acta Phys. Slov.* **57** (2007)
- [103] Nitta, J., Akazaki, T., Takayanagi, H. & Enoki, T. Gate control of spin-orbit interaction in an inverted In<sub>0.53</sub>Ga<sub>0.47</sub>As/In<sub>0.52</sub>Al<sub>0.48</sub>As heterostructure. *Phys. Rev. Lett.* **78**, 1335–1338 (1997)
- [104] Grundler, D. Large Rashba splitting in InAs quantum wells due to electron wave function penetration into the barrier layers. *Phys. Rev. Lett.* **84**, 6074–6077 (2000)
- [105] Shojaei, B. *et al.* Demonstration of gate control of spin splitting in a high-mobility InAs/AlSb two-dimensional electron gas. *Phys. Rev. B* **93** (2016)
- [106] Žutić, I., Fabian, J. & Sarma, S. D. Spintronics: Fundamentals and applications. *Rev. Mod. Phys.* **76**, 323–410 (2004)
- [107] Datta, S. & Das, B. Electronic analog of the electro-optic modulator. *Appl. Phys. Lett.* **56**, 665 (1990)
- [108] Liu, C., Hughes, T. L., Qi, X.-L., Wang, K. & Zhang, S.-C. Quantum spin Hall effect in inverted type-II semiconductors. *Phys. Rev. Lett.* **100**, 236601 (2008)
- [109] Qu, F. *et al.* Electric and magnetic tuning between the trivial and topological phases in InAs/GaSb double quantum wells. *Phys. Rev. Lett.* **115**, 036803 (2015)



- [110] de Andrada e Silva, E. A., Rocca, G. C. L. & Bassani, F. Spin-split subbands and magneto-oscillations in iii-v asymmetric heterostructures. *Phys. Rev. B* **50**, 8523–8533 (1994)
- [111] Cooper, L. J. *et al.* Resistance resonance induced by electron-hole hybridization in a strongly coupled InAs/GaSb/AlSb heterostructure. *Phys. Rev. B* **57**, 11915–11918 (1998)
- [112] Zakharova, A., Yen, S. & Chao, K. Hybridization of electron, light-hole, and heavy-hole states in InAs/GaSb quantum wells. *Phys. Rev. B* **64** (2001)
- [113] Halvorsen, E., Galperin, Y. & Chao, K. A. Optical transitions in broken gap heterostructures. *Phys. Rev. B* **61**, 16743–16749 (2000)
- [114] Xu, W., Li, L. L., Dong, H. M., Gumbs, G. & Folkes, P. A. Band hybridization and spin-splitting in InAs/AlSb/GaSb type II and broken-gap quantum wells. *J. Appl. Phys.* **108**, 053709 (2010)
- [115] Nichele, F. *et al.* Giant spin-orbit splitting in inverted InAs/GaSb double quantum wells. *Phys. Rev. Lett.* **118**, 016801 (2017)
- [116] Li, J., Chang, K., Hai, G. Q. & Chan, K. S. Anomalous rashba spin-orbit interaction in InAs/GaSb quantum wells. *Appl. Phys. Lett.* **92**, 152107 (2008)
- [117] Onsager, L. Interpretation of the de haas-van alphen effect. *Philos. Mag.* **43**, 1006–1008 (1952)
- [118] Sander, T. H., Holmes, S. N., Harris, J. J., Maude, D. K. & Portal, J. C. Determination of the phase of magneto-intersubband scattering oscillations in heterojunctions and quantum wells. *Phys. Rev. B* **58**, 13856–13862 (1998)
- [119] Rowe, A. C. H., Nehls, J., Stradling, R. A. & Ferguson, R. S. Origin of beat patterns in the quantum magnetoresistance of gated InAs/GaSb and InAs/AlSb quantum wells. *Phys. Rev. B* **63** (2001)
- [120] Tsui, D. C., Englert, T., Cho, A. Y. & Gossard, A. C. Observation of magnetophonon resonances in a two-dimensional electronic system. *Phys. Rev. Lett.* **44**, 341–344 (1980)
- [121] Gurevich, V. L. & Firsov, Y. A. On the theory of the electrical conductivity of semiconductors in a magnetic field, 1. *JETP Lett.* **13**, 137–146 (1961)
- [122] Averkiev, N. S., Glazov, M. M. & Tarasenko, S. A. Suppression of spin beats in magneto-oscillation phenomena in two-dimensional electron gas. *Solid State Comm.* **133**, 543–547 (2005)
- [123] Symons, D. M. *et al.* Magnetic breakdown in the semimetallic InAs/GaSb system. *Phys. Rev. B* **58**, 7292–7299 (1998)
- [124] Shoenberg, D. *Magnetic oscillations in metals* (Cambridge University Press (CUP), 1984)

- 
- [125] Ganichev, S. D. *et al.* Experimental separation of rashba and dresselhaus spin splittings in semiconductor quantum wells. *Phys. Rev. Lett.* **92** (2004)
- [126] Herzog, F., Hardtdegen, H., Schäpers, T., Grundler, D. & Wilde, M. A. Experimental determination of rashba and dresselhaus parameters and  $g^*$ -factor anisotropy via shubnikov-de haas oscillations. *New J. Phys.* **19**, 103012 (2017)
- [127] Bychkov, Y. A. & Rashba, E. I. Oscillatory effects and the magnetic susceptibility of carriers in inversion layers. *J. Phys. Condens. Matter* **17**, 6039 (1984)
- [128] Bychkov, Y. A. & Rashba, E. I. Properties of a 2d electron gas with lifted spectral degeneracy. *JETP Lett.* **39**, 78 (1984)
- [129] Studer, M., Salis, G., Ensslin, K., Driscoll, D. C. & Gossard, A. C. Gate-controlled spin-orbit interaction in a parabolic GaAs/AlGaAs quantum well. *Phys. Rev. Lett.* **103**, 027201 (2009)
- [130] Luo, J., Munekata, H., Fang, F. F. & Stiles, P. J. Effects of inversion asymmetry on electron energy band structures in GaSb/InAs/GaSb quantum wells. *Phys. Rev. B* **41**, 7685–7693 (1990)
- [131] Hasan, M. Z. & Kane, C. L. *Colloquium* : Topological insulators. *Rev. Mod. Phys.* **82**, 3045–3067 (2010)
- [132] Kane, C. L. & Mele, E. J. Quantum spin hall effect in graphene. *Phys. Rev. Lett.* **95**, 226801 (2005)
- [133] König, M. *et al.* Quantum spin hall insulator state in hgte quantum wells. *Science* **318**, 766–770 (2007)
- [134] Hart, S. *et al.* Induced superconductivity in the quantum spin hall edge. *Nature Phys.* **10**, 638–643 (2014)
- [135] Pribiag, V. S. *et al.* Edge-mode superconductivity in a two-dimensional topological insulator. *Nature Nanotech.* **10**, 593–597 (2015)
- [136] van Wees, B. *et al.* Breakdown of the quantum hall effect in inas/alsb quantum wells due to counterflowing edge channels. *Phys. Rev. B* **51**, 7973–7976 (1995)
- [137] Nguyen, B.-M. *et al.* Decoupling edge versus bulk conductance in the trivial regime of an InAs/GaSb double quantum well using corbino ring geometry. *Phys. Rev. Lett.* **117**, 077701 (2016)
- [138] Nichele, F. *et al.* Edge transport in the trivial phase of inas/gasb. *New J. Phys.* **18**, 083005 (2016)
- [139] Tamm, I. On the possible bound states of electrons on a crystal surface. *Phys. Z. Soviet Union* **1** (1932)
- [140] Shockley, W. On the surface states associated with a periodic potential. *Phys. Rev.* **56**, 317–323 (1939)

- [141] Furukawa, A. Dependence of electron accumulation in alsb/inas quantum well on thin surface materials of inas and gasb. *Appl. Phys. Lett.* **62**, 3150–3152 (1993)
- [142] Olsson, L. O. *et al.* Charge accumulation at inas surfaces. *Phys. Rev. Lett.* **76**, 3626–3629 (1996)
- [143] Abanin, D. A. *et al.* Giant nonlocality near the dirac point in graphene. *Science* **332**, 328–330 (2011)
- [144] Efros, A. L. & Shklovskii, B. I. Coulomb gap and low temperature conductivity of disordered systems. *J. Phys. Condens. Matter* **8**, L49 (1975)
- [145] Flensberg, K., Hansen, J. B. & Octavio, M. Subharmonic energy-gap structure in superconducting weak links. *Phys. Rev. B* **38**, 8707–8711 (1988)
- [146] Allen, M. T. *et al.* Spatially resolved edge currents and guided-wave electronic states in graphene. *Nature Phys.* **12**, 128–133 (2016)
- [147] Haberkorn, W., Knauer, H. & Richter, J. A theoretical study of the current-phase relation in josephson contacts. *Phys. Status Solidi A* **47**, K161–K164 (1978)
- [148] Ben Shalom, M. *et al.* Quantum oscillations of the critical current and high-field superconducting proximity in ballistic graphene. *Nature Phys.* **12**, 318–322 (2016)
- [149] Meier, H., Fal’ko, V. I. & Glazman, L. I. Edge effects in the magnetic interference pattern of a ballistic sns junction. *Phys. Rev. B* **93**, 184506 (2016)
- [150] Russo, S., Kroug, M., Klapwijk, T. M. & Morpurgo, A. F. Experimental observation of bias-dependent nonlocal andreev reflection. *Phys. Rev. Lett.* **95**, 027002 (2005)
- [151] Baxevanis, B., Ostroukh, V. P. & Beenakker, C. W. J. Even-odd flux quanta effect in the fraunhofer oscillations of an edge-channel josephson junction. *Phys. Rev. B* **91**, 041409 (2015)
- [152] van Ostaay, J. A. M., Akhmerov, A. R. & Beenakker, C. W. J. Spin-triplet supercurrent carried by quantum hall edge states through a josephson junction. *Phys. Rev. B* **83**, 195441 (2011)
- [153] Liu, J., Liu, H., Song, J., Sun, Q.-F. & Xie, X. C. Superconductor-graphene-superconductor josephson junction in the quantum hall regime. *Phys. Rev. B* **96**, 045401 (2017)
- [154] Recher, P., Sukhorukov, E. V. & Loss, D. Andreev tunneling, coulomb blockade, and resonant transport of nonlocal spin-entangled electrons. *Phys. Rev. B* **63**, 165314 (2001)
- [155] Stan, G., Field, S. B. & Martinis, J. M. Critical field for complete vortex expulsion from narrow superconducting strips. *Phys. Rev. Lett.* **92**, 097003 (2004)
- [156] Furusaki, A. DC Josephson effect in dirty SNS junctions: Numerical study. *Phys. B Condens. Matter* **203**, 214–218 (1994)

- 
- [157] Oreg, Y., Refael, G. & von Oppen, F. Helical liquids and majorana bound states in quantum wires. *Phys. Rev. Lett.* **105**, 177002 (2010)
- [158] Lutchyn, R. M., Sau, J. D. & Das Sarma, S. Majorana fermions and a topological phase transition in semiconductor-superconductor heterostructures. *Phys. Rev. Lett.* **105**, 077001 (2010)
- [159] Amet, F. *et al.* Supercurrent in the quantum hall regime. *Science* **352**, 966–969 (2016)
- [160] de Vries, F. K. *et al.*  $h/e$  superconducting quantum interference through trivial edge states in inas. *Phys. Rev. Lett.* **120**, 047702 (2018)
- [161] Nilsson, H. A. *et al.* Giant, level-dependent  $g$  factors in insb nanowire quantum dots. *Nano Lett.* **9**, 3151–3156 (2009)
- [162] Kreuzt, E., Rickus, E. & Sotnik, N. Barrier height and surface states at cleaned insb(110) surfaces. *Thin Solid Films* **101**, 153 – 165 (1983)
- [163] Ritz, A. & Lüth, H. Determination of space charge layer parameters on insb(110) by electron energy loss spectroscopy. *J. Vac. Sci. Technol.* **3**, 1153–1156 (1985)
- [164] Whitman, L. J., Stroscio, J. A., Dragoset, R. A. & Celotta, R. J. Scanning-tunneling-microscopy study of insb(110). *Phys. Rev. B* **42**, 7288–7291 (1990)
- [165] Jacquet, R., Rech, J., Jonckheere, T., Zazunov, A. & Martin, T. Cooper pair splitting and recombination in a nanosquid geometry at high transparency. *Phys. Rev. B* **92**, 235429 (2015)
- [166] Chiodi, F. *et al.* Geometry-related magnetic interference patterns in long  $sns$  josephson junctions. *Phys. Rev. B* **86**, 064510 (2012)
- [167] Rohlfing, F. *et al.* Doppler shift in andreev reflection from a moving superconducting condensate in nb/inas josephson junctions. *Phys. Rev. B* **80**, 220507 (2009)
- [168] Amado, M. *et al.* Electrostatic tailoring of magnetic interference in quantum point contact ballistic josephson junctions. *Phys. Rev. B* **87**, 134506 (2013)
- [169] Kraft, R. *et al.* Tailoring supercurrent confinement in graphene bilayer weak links. *Nature Commun.* **9** (2018)
- [170] Qu, F. *et al.* Quantized conductance and large  $g$ -factor anisotropy in insb quantum point contacts. *Nano Lett.* **16**, 7509–7513 (2016)
- [171] Pientka, F. *et al.* Topological superconductivity in a planar josephson junction. *Phys. Rev. X* **7**, 021032 (2017)
- [172] Hell, M., Leijnse, M. & Flensberg, K. Two-dimensional platform for networks of majorana bound states. *Phys. Rev. Lett.* **118**, 107701 (2017)

- [173] Ren, H. *et al.* Topological superconductivity in a phase-controlled josephson junction. *arXiv preprint 1809.03076* (2018)
- [174] Fornieri, A. *et al.* Evidence of topological superconductivity in planar josephson junctions. *arXiv preprint 1809.03037* (2018)
- [175] Clarke, J. & Braginski, A. I. *The SQUID handbook, vol. 1* (Wiley-VCH Verlag GmbH & Co. KGaA, 2004)
- [176] Grajcar, M. *et al.* Supercurrent–phase relation of a nb/inas(2deg)/nb josephson junction. *Phys. C Supercond.* **372-376**, 27 – 30 (2002)
- [177] Ebel, M. *et al.* Supercurrent-phase relationship of a nb/inas 2des/nb josephson junction in overlapping geometry. *Phys. Rev. B* **71**, 052506 (2005)
- [178] Delagrangé, R. *et al.*  $0-\pi$  quantum transition in a carbon nanotube josephson junction: Universal phase dependence and orbital degeneracy. *Phys. Rev. B* **93**, 195437 (2016)
- [179] Delagrangé, R. *et al.*  $0-\pi$  quantum transition in a carbon nanotube josephson junction: universal phase dependence and orbital degeneracy. *Physica B* (2018)
- [180] Luo, J., Munekata, H., Fang, F. F. & Stiles, P. J. Observation of the zero-field spin splitting of the ground electron subband in gasb-inas-gasb quantum wells. *Phys. Rev. B* **38**, 10142–10145 (1988)
- [181] Das, B. *et al.* Evidence for spin splitting in  $\text{In}_x\text{Ga}_{1-x}\text{As}/\text{In}_{0.52}\text{Al}_{0.48}\text{As}$  heterostructures as  $b \rightarrow 0$ . *Phys. Rev. B* **39**, 1411–1414 (1989)
- [182] Nanda, G. *et al.* Current-phase relation of ballistic graphene josephson junctions. *Nano Lett.* **17**, 3396–3401 (2017)
- [183] Fulton, T. A., Dunkleberger, L. N. & Dynes, R. C. Quantum interference properties of double josephson junctions. *Phys. Rev. B* **6**, 855–875 (1972)
- [184] Suominen, H. J. *et al.* Zero-energy modes from coalescing andreev states in a two-dimensional semiconductor-superconductor hybrid platform. *Phys. Rev. Lett.* **119**, 176805 (2017)
- [185] Kells, G., Meidan, D. & Brouwer, P. W. Near-zero-energy end states in topologically trivial spin-orbit coupled superconducting nanowires with a smooth confinement. *Phys. Rev. B* **86**, 100503 (2012)
- [186] Prada, E., San-Jose, P. & Aguado, R. Transport spectroscopy of  $ns$  nanowire junctions with majorana fermions. *Phys. Rev. B* **86**, 180503 (2012)
- [187] Suominen, H. J. *et al.* Anomalous fraunhofer interference in epitaxial semiconductor-semiconductor josephson junctions. *Phys. Rev. B* **95**, 035307 (2017)

- 
- [188] Cuevas, J. C. & Bergeret, F. S. Magnetic interference patterns and vortices in diffusive s/n junctions. *Phys. Rev. Lett.* **99**, 217002 (2007)
- [189] Sun, J. *et al.* Helical hole state in multiple conduction modes in ge/si core/shell nanowire. *Nano Lett.* **18**, 6144–6149 (2018)
- [190] Wang, R., Deacon, R. S., Yao, J., Lieber, C. M. & Ishibashi, K. Electrical modulation of weak-antilocalization and spin-orbit interaction in dual gated ge/si core/shell nanowires. *Semicond. Sci. Technol.* **32**, 094002 (2017)
- [191] Krogstrup, P. *et al.* Epitaxy of semiconductor–superconductor nanowires. *Nature materials* **14**, 400 (2015)
- [192] Riwar, R.-P., Houzet, M., Meyer, J. S. & Nazarov, Y. V. Multi-terminal josephson junctions as topological matter. *Nature Commun.* **7**, 11167 (2016)
- [193] Rosdahl, T. O., Vuik, A., Kjaergaard, M. & Akhmerov, A. R. Andreev rectifier: A nonlocal conductance signature of topological phase transitions. *Phys. Rev. B* **97**, 045421 (2018)
- [194] de Lange, G. *et al.* Realization of microwave quantum circuits using hybrid superconducting–semiconducting nanowire josephson elements. *Phys. Rev. Lett.* **115**, 127002 (2015)
- [195] Larsen, T. W. *et al.* Semiconductor-nanowire-based superconducting qubit. *Phys. Rev. Lett.* **115**, 127001 (2015)
- [196] Mi, S. *Signatures of Majorana zero-modes in nanowires, quantum spin Hall edges, and quantum dots.* Ph.D. thesis, Leiden University (2015)
- [197] Haim, A. & Stern, A. The double-edge sword of disorder in multichannel topological superconductors. *arXiv preprint 1808.07886* (2018)
- [198] Laeven, T. M., Nijholt, B., Wimmer, M. & Akhmerov, A. R. Improved isolation of majorana bound states in zigzag-shaped junctions. *In preparation.*
- [199] Hell, M., Flensberg, K. & Leijnse, M. Coupling and braiding majorana bound states in networks defined in two-dimensional electron gases with proximity-induced superconductivity. *Phys. Rev. B* **96**, 035444 (2017)
- [200] Grivnin, A., Bor, E., Heiblum, M., Oreg, Y. & Shtrikman, H. Concomitant opening of a topological bulk-gap with an emerging majorana edge-state. *arXiv preprint 1807.06632* (2018)
- [201] Das Sarma, S., Sau, J. D. & Stanescu, T. D. Splitting of the zero-bias conductance peak as smoking gun evidence for the existence of the majorana mode in a superconductor-semiconductor nanowire. *Phys. Rev. B* **86**, 220506 (2012)
- [202] Lai, Y.-H., Sau, J. D. & Sarma, S. D. Presence versus absence of end-to-end nonlocal conductance correlations in majorana nanowires: Majorana bound states versus andreev bound states. *arXiv preprint 1901.02655* (2019)

- [203] Aasen, D. *et al.* Milestones toward majorana-based quantum computing. *Phys. Rev. X* **6**, 031016 (2016)
- [204] Beukman, A. J. A. *et al.* Spin-orbit interaction in a dual gated inas/gasb quantum well. *Phys. Rev. B* **96**, 241401 (2017)
- [205] Kallaher, R. L., Heremans, J. J., Goel, N., Chung, S. J. & Santos, M. B. Spin-orbit interaction determined by antilocalization in an insb quantum well. *Phys. Rev. B* **81**, 075303 (2010)
- [206] Gui, Y. S. *et al.* Giant spin-orbit splitting in a HgTe quantum well. *Phys. Rev. B* **70**, 115328 (2004)
- [207] Landwehr, G., Zhang, X., Ortner, K., Pfeuffer-Jeschke, A. & Becker, C. Determination of the g-factor of n-type hgte hg1-xcdxte single quantum wells. *Superlattice. Microst.* **34**, 519 – 524 (2003)
- [208] Ke, C. T. *et al.* Induced superconductivity and tunable  $\pi$ -junctions in insb quantum wells. *In preparation.*

# ACKNOWLEDGEMENTS

First of all, Leo, thank you for supervising me during the four years and giving me the opportunity to work in the great environment you created. You managed to keep me motivated during moments of doubt, and kept on challenging me. I very much enjoyed being part of your group and wish you lots of success with the Microsoft lab.

Srijit, thank you for being my copromotor, it was great to team up with you after my first year. Even though the IV-VI semiconductor devices never materialized, I am happy to see that you built up your own lab, and the InSb is working so well now. It was great to work in the 'new' 2D topo team with Christian, Ting, Qing, Prasanna, Michael, Ivan and Saurabh. I enjoyed the meetings, journal clubs and of course playing darts in 't Proeflokaal.

Arjan, Fanming and Stevan, I still have very good memories of the 'old' 2D topo team. I learned a lot from all of you about what being a researcher entails, from the fabrication of the 2D samples to the process of writing a manuscript and unfortunately also terminating a project. Jasper, it is great to see you found an interesting new research direction, and also did a very good job on that. Good luck finishing your thesis.

Thank you Jie, for working together on some hard projects. I admire your perseverance in both making devices and making them work. I think we are quite complementary, which made us a good team. I am convinced you will find a good faculty position soon.

To come up with new ideas for experiments, and to find explanations for the experimental data, I benefited greatly from many discussions with theory collaborators. Slava, thank you for tackling the even-odd effect, and taking the time for our discussions on the modeling. Rafal, Daniel and Michal thank you for your work on the GeSi nanowires, I am glad we were able to combine all the work in a nice publication. Michael and Anton, thank you very much for all discussions we had on several topics and experimental ideas.

Along the way I had the opportunity to supervise several students during their thesis projects. David, even though a bachelor thesis is short, you managed to get some nice results out. Tom and Eric, both of you did a great job, became independent very quickly and took charge of your own projects. I learned a lot from supervising you, both when things were working and when they didn't. Thanks for all the hard work, and I hope the experience will be of help in your careers outside academia.

All of this work could not have been possible without the help of the support staff and technicians. Marja, Yuki, Simone, Jenny and Chantal, thank you for the help with the administration and finance, and thank you for organizing the Christmas parties and summer BBQ's. Heera, thank you for coordinating the PR activities of the promo team. I enjoyed our tea breaks and chats about Qutech, personal development and a lot of other things. Good luck with your new job. Mark, Remco, Jelle and Siebe thank you for your work on all the lines/pumps/cables in the labs and the Qutech cleanroom equipment. Raymond, Raymond and Marijn, thanks for your help with the electrical measurement



setup. Olaf and Jason, I always enjoyed solving the fridge problems together. Thanks to all cleanroom staff for maintaining such a great cleanroom to work in. Ewan, in particular, thank you for the fun conversations we had, making being in the cleanroom (even more) fun, and, for organizing our winning team for the TNO football tournament.

Apart from the people I worked with directly, I enjoyed the company of many others within the topo team and QuTech. Vincent, Kun, Önder and David, thanks for teaching me all kinds of cleanroom and labskills in my first years. Michiel, thank you for the many interesting discussions on physics, sports and other things in life. Being teaching assistant of the quantum hardware course, together with Niels, was hard work but also a lot of fun. I learned a lot from you and am very happy to have you as one of my paranymphs. Alex, thanks for the many enjoyable coffee breaks and (early) lunches. I will never forget cycling through the Schilderswijk with you. James, you are always up for a nice chat or interesting conversation. I hope the Netherlands will treat you well in the future and am looking forward to our first conversation in Dutch. Florian, thanks for your efforts in organizing the meetings with the Aachen guys. Good luck with your new job in Portland. Damaz, Willemijn and Jouri, it was fun being around you, either at the topological island or during coffee/tea breaks, good luck with the final year of your PhDs. Filip, Anne-Marije, Norbert and Florian, thank you for the organization of the best QuTech uitje ever. Toivo, Uditendu, Suzanne, Jelmer and Adriaan, thanks for keeping up the QT family feeling by organising and participating in the QuTech wide activities. Thanks to all QuTech'ers for joining (and winning) the VvTP sportsday.

Naast het werk hebben de activiteiten buiten het werk mij altijd heel erg geholpen om te ontspannen en weer op te laden voor een nieuwe dag of week. DOPC'ers, leuk dat jullie vaak vroegen of het bakken of the chips nog in goed orde verliep. Jaarclubgenoten, ik vind het fantastisch dat we weer samen op lustrumreis zijn geweest (en gaan). Bestuursgenoten, leuk om te zien dat het lukt om regelmatig af te spreken, het is altijd als vanouds gezellig. Marc, Marco en de boys, gezellig om soms aan een hardloopwedstrijd mee te doen of gewoon een biertje te drinken. Twan, bedankt voor het geïnteresseerd doorvragen naar mijn onderzoek, en pas stoppen als je het zelf ook echt begrijpt.

Pa en Ma, bedankt voor jullie onvoorwaardelijke steun tijdens mijn pieken en dalen in de afgelopen jaren. Jullie hebben ons altijd gemotiveerd om alles uit onszelf te halen en volgens mij zijn we aardig op weg. Marieke, fantastisch om te zien dat je samen met David een mooi gezin hebt gesticht. Lianne, gezellig dat je een leuke baan in Rotterdam hebt gevonden en bedankt dat je mijn paranimf wil zijn. Beide heel veel succes met jullie onderzoeksprojecten, ik ben benieuwd wat de toekomst jullie brengt. Tenslotte, Tamara, het leven samen is heerlijk, bedankt voor je steun en voor het helpen met relativeren. De beklimming van de Elbroes was een hoogtepunt en ik hoop er nog veel met jou te beleven.

# CURRICULUM VITÆ

## **Folkert Kornelis DE VRIES**

- 28-06-1990 Born in Amsterdam, the Netherlands.
- 2002-2008 Secondary school, Hermann Wesselink College, Amstelveen.
- 2008-2012 BSc Applied Physics, Delft University of Technology.  
*Thesis supervisor:* Prof. dr. ir. H. S. J. van der Zant.
- 2012-2014 MSc Applied Physics, Delft University of Technology.  
*Thesis supervisor:* Prof. dr. ir. L. P. Kouwenhoven.
- 2014 Research intership, Harvard University.  
*Supervisor:* Prof. A. Yacoby.
- 2015-2018 PhD Research, Delft University of Technology.  
*Promotor:* Prof. dr. ir. L. P. Kouwenhoven.



# LIST OF PUBLICATIONS

9. *Spin-orbit interaction and induced superconductivity in an one-dimensional hole gas*  
**Folkert K. de Vries**, Jie Shen, Rafal J. Skolasinski, Michal P. Nowak, Daniel Varjas, Lin Wang, Michael Wimmer, Joost Ridderbos, Floris A. Zwanenburg, Ang Li, Sebastian Koelling, Marcel A. Verheijen, Erik P. A. M. Bakkers, Leo P. Kouwenhoven  
[Nano Lett. 18 \(10\), 6483-6488, 2018](#)
8. *Josephson effect in a few-hole quantum dot*  
Joost Ridderbos, Matthias Brauns, Jie Shen, **Folkert K. de Vries**, Ang Li, Erik P. A. M. Bakkers, Alexander Brinkman, Floris A. Zwanenburg  
[Advanced Materials 1802257, 2018](#)
7.  *$h/e$  superconducting quantum interference through trivial edge states in InAs*  
**Folkert K. de Vries**, Tom Timmerman, Viacheslav P. Ostroukh, Jasper van Veen, Arjan J. A. Beukman, Fanming Qu, Michael Wimmer, Binh-Minh Nguyen, Andrey A. Kiselev, Wei Yi, Marko Sokolich, Michael J. Manfra, Charles M. Marcus, Leo P. Kouwenhoven  
[Phys. Rev. Lett. 120, 047702, 2018](#)
6. *Spin-orbit interaction in a dual gated InAs/GaSb quantum well*  
Arjan J. A. Beukman, **Folkert K. de Vries**, Jasper van Veen, Rafal Skolasinski, Michael Wimmer, Fanming Qu, David T. de Vries, Binh-Minh Nguyen, Wei Yi, Andrey A. Kiselev, Marko Sokolich, Michael J. Manfra, Fabrizio Nichele, Charles M. Marcus, Leo P. Kouwenhoven  
[Phys. Rev. B 96, 241401\(R\), 2017](#)
5. *Ballistic superconductivity in semiconductor nanowires*  
Hao Zhang, Önder Gül, Sonia Conesa-Boj, Michal P. Nowak, Michael Wimmer, Kun Zuo, Vincent Mourik, **Folkert K. de Vries**, Jasper van Veen, Michiel W. A. de Moor, Jouri D.S. Bommer, David J. van Woerkom, Diana Car, Sebastian R. Plissard, Erik P. A. M. Bakkers, Marina Quintero-Pérez, Maja C. Cassidy, Sebastian Koelling, Srijit Goswami, Kenji Watanabe, Takashi Taniguchi, Leo P. Kouwenhoven  
[Nature Commun. 8, 16025, 2017](#)
4. *Hard superconducting gap in InSb nanowires*  
Önder Gül, Hao Zhang, **Folkert K. de Vries**, Jasper van Veen, Kun Zuo, Vincent Mourik, Sonia Conesa-Boj, Michal P. Nowak, David J. Van Woerkom, Marina Quintero-Pérez, Maja C. Cassidy, Attila Geresdi, Sebastian Koelling, Diana Car, Sebastian R. Plissard, Erik P. A. M. Bakkers, Leo P. Kouwenhoven  
[Nano Letters 17 \(4\), 2690-2696, 2017](#)
3. *Quantized conductance and large  $g$ -factor anisotropy in InSb quantum point contacts*  
Fanming Qu, Jasper van Veen, **Folkert K. de Vries**, Arjan J. A. Beukman, Michael Wimmer, Wei Yi, Andrey A. Kiselev, Binh-Minh Nguyen, Marko Sokolich, Michael J. Manfra, Fabrizio Nichele, Charles M. Marcus, Leo P. Kouwenhoven  
[Nano Lett. 16 \(12\), 7509-7513, 2016](#)

2. *Decoupling edge versus bulk conductance in the trivial regime of an InAs/GaSb double quantum well using Corbino ring geometry*  
Binh-Minh Nguyen, Andrey A. Kiselev, Ramsey Noah, Wei Yi, Fanming Qu, Arjan J. A. Beukman, **Folkert K. de Vries**, Jasper van Veen, Stevan Nadj-Perge, Leo P. Kouwenhoven, Morten Kjaergaard, Henri J. Suominen, Fabrizio Nichele, Charles M. Marcus, Michael J. Manfra, Marko Sokolich  
[Phys. Rev. Lett. 117 \(7\), 077701, 2016](#)
1. *Edge Transport in the Trivial Phase of InAs/GaSb*  
Fabrizio Nichele, Henri J. Suominen, Morten Kjaergaard, Charles M. Marcus, Ebrahim Sajadi, Joshua A. Folk, Fanming Qu, Arjan J. A. Beukman, **Folkert K. de Vries**, Jasper van Veen, Stevan Nadj-Perge, Leo P. Kouwenhoven, Binh-Minh Nguyen, Andrey A. Kiselev, Wei Yi, Marko Sokolich, Michael J. Manfra, Eric M. Spanton, Kathryn A. Moler  
[New J. Phys. 18 \(8\), 083005, 2016](#)